



TECHNISCHE UNIVERSITÄT WIEN

DISSERTATION

Upgrading and new applications of a neutron imaging facility

ausgeführt zum Zwecke der Erlangung des akademischen Grades eines
Doktors der Technischen Wissenschaften unter der Leitung von

O. Univ. Prof. Dipl.-Ing Dr Helmut Rauch
E 141 – Atominstitut der “Österreichischen Universitäten”

Eingereicht an der Technischen Universität Wien,
Fakultät für Technische Physik von

FAREEHA HAMEED
MATRIKELNUMMER: 0427436
GYMNASIUMSTRASSE 85/561
1190 WIEN

Wien, am November 2008

Abstract

This thesis describes the upgrading and new applications of the neutron imaging facility at a low power TRIGA Mark II research reactor at The Atomic Institute (ATI) in Vienna. This upgrading has improved the spatial resolution and made possible longer neutron tomography measurements to exploit the full dynamic range. The instrumental setup has been used successfully in various applications. The techniques of neutron imaging that have been employed include neutron radiography, neutron tomography and dynamic imaging. Interesting applications in the fields of engineering and geology based on hydrogen transport within samples have been made. The methods of neutron imaging have been applied to conservation and restoration projects in engineering geology where the distribution and penetration of stone consolidants inside building materials have been investigated. This method has been applied to assess conservation and restoration processes and for the selection of stone strengtheners based on their penetration and distribution for historical buildings and monuments. An application having value for the textile industry is the study of moisture transport in different fibers. The distribution of moisture in different textile fibers is important for comfort. Non-destructive imaging of radioactive samples relevant to the nuclear industry has also been presented. Neutron radiography and tomography techniques were applied to isotopic neutron sources to get information about their construction and density. Beam hardening correction was performed for the neutron tomography of a neutron source. These applications show that high resolution neutron imaging can be performed at a low power research reactor and is thus encouraging for mobile neutron sources as well. Neutron imaging is therefore a suitable technique for non-destructive studies in various fields.

Abstrakt

Die Arbeit beschreibt die Erneuerung und neue Anwendungen an der Neutronenradiographie- und Tomographiestation des Atominstutes mit seinem TRIGA Mark II Forschungsreaktor. In diesem Rahmen wurde die räumliche Auflösung deutlich verbessert, und der dynamische Bereich der digitalen Detektoren kann jetzt auch bei tomographischen Messungen voll ausgeschöpft werden. Mit dem neuen Setup wurden Projekte auf den Gebieten Materialforschung, Geologie und Ingenieurgeologie durchgeführt. In einem Konservierungs- und Restaurierungsprojekt wurde die Strahlschwächung durch Wasserstoff verwendet, um die Verteilung und das Eindringen von Steinfestigern und Konservierungsmitteln in Baumaterialien, historischen Gebäuden und Denkmäler zu untersuchen.

Eine weitere Anwendung ist die Analyse des Feuchtetransportes in Textilfasern, die für den Tragekomfort maßgeblich ist. Mit unserem hochauflösenden Imaging Plate Detektor und dem neuen 100 μ m Szintillationsdetektor konnten temperaturabhängige, materialspezifische Feuchtigkeitsverteilungen systematisch untersucht werden.

Anschließend wurden drei kompakte Neutronenquellen, zwei Plutonium-Beryllium und eine Americium-Beryllium Quelle, analysiert. Die Neutronentomographie ist die einzige Messmethode mit der die Mantel- und Quellgeometrie sowie die makroskopischen Wirkungsquerschnitte im Quellkern zerstörungsfrei rekonstruiert werden können. Mit Hilfe der von uns entwickelten Beam-Hardening-Korrektur konnte eine homogene Isotopenverteilung im Pu-Be Kern nachgewiesen werden, während in der Am-Be Quelle ein Bruch im Kern sichtbar wurde. Es ist bemerkenswert, dass tomographische Abbildungen von stark absorbierenden Proben auch bei nur 250 kW Reaktorleistung möglich sind.

Anhand dieser Anwendungen wurden die Vorteile der zerstörungsfreien Neutronenabbildungsverfahren, sowie die Aktualität des Forschungsgebietes demonstriert.

Dedicated to

My father Abdul Hameed Chaudhry

I couldn't have started and completed without his love, support and encouragement

Acknowledgements

I express my gratitude to God Almighty, the beneficent, and the merciful.

I would like to warmly thank all who have contributed to the successful completion of this work. First of all I would like to thank Prof. Helmut Rauch for giving me the opportunity to be a member of his excellent scientific group. His profound approach to physical phenomena, demonstrated in the regular seminars of the group, had a strong pedagogical influence on me. Prof. Helmut Böck for his interest in my work and for providing the neutron sources. I appreciate Dr. Michael Zawisky's cooperation as the instrument responsible for the neutron imaging facility at the Atomic Institute.

I am thankful to Dr. Eberhard Lehmann and Lidija Jose from the Paul Scherrer Institute, Switzerland, for their help with the quantitative analysis. I would like to acknowledge Dr. Burkhard Schillinger, the ANTARES team and Hongyun Lee for their cooperation during the experiments performed at ANTARES, Technische Universität München, FRM II and Physics Department E21, Garching, Germany, which were supported by the European research project (NMI3).

Dr. K. Christian Schuster and Ksenija Varga from the Lenzing Textile Company for the interesting application of neutron imaging in textile fibers. Prof. Andreas Rohatsch from the Institute of Engineering Geology, for providing the conservation samples and his excellent interpretations and discussions. W. Zehetner (Dombaumeister), P. Stastny, G. Hahn, and K. Deuthauser, for many interesting discussions, and for providing samples from the Dombauhütte St. Stephan. Prof. Bernhard Graseman, department of geological sciences and Dr. Ulrike Exner, Department of Geodynamics and Sedimentology, Structural Processes Group, University of Vienna for providing samples and interesting discussions. Johann Nimmrichter from the Austrian Federal Office for the Care and Protection of Monuments, Department for Conservation for providing original restored samples from historical buildings and monuments.

Warm thanks to my former and present colleagues, Dr. Menekse Bastürk, Paulo Capka, Dr. Katharina Durstberger, Dr. Stefan Filip, Sulyok Georg, Dr. Yuji Hasegawa, Dr. Erwin Jericha, Sam Karimzadeh, Rustam Khan, Jürgen Klepp, Dr. Hartmut Lemmel, Dr. Simon Mayer, Stephan Sponar, Joseph Springer, Thomas Stummer, Halit Tatlisu, Dr. Martin Trinker, and Babak Zamani. I express my gratitude for the fruitful discussions and pleasant atmosphere. Dr. Mario Villa, Ernst Klapfer and Hans Schachnar who are responsible for the reactor operation. Prof. Sauerzopf, Hartmann, and Barbara Fertl for their help with liquid nitrogen and technical matters. Eva Cech-Haberl and Tamara Jurschitsch for secretarial support. Herbert Diem and Helmut Richter for their help with the solution of computer problems.

Björn Chyba from Vienna University of Technology and Salamar Dietberger from H.G. Wells for their help with the X-ray measurements. J. Weber from the Institute of Art and Technology, University of Applied Arts Vienna for the SEM analysis. We would like to thank BÖHLER Bleche GmbH, Müzzuschlag in Austria for providing the boron alloyed steel sheets and plates.

Prof. Sarwar Buksh Leghari who encouraged me to proceed for my PhD studies. Arjumand Durrani for her sincere suggestions and my friends Saadia, Aneesa, Navida and Shahroz for their company and support. I think these are not the only names, the list is endless. I am thankful to all my friends and well wishers.

My family, particularly my mother for whom I lack words to express my gratitude, she always wanted what she thought was the best for me, and especially my daughter, Aimen who has always been a source of strength in my life.

This PhD study was supported by The Higher Education Commission, Pakistan, Austrian Exchange Service (ÖAD) and Academic Cooperation and Mobility Unit (ACM), Austria.

Contents

ABSTRACT	2
ABSTRAKT	3
1 INTRODUCTION.....	11
2 NEUTRON IMAGING.....	14
2.1 NEUTRON RADIOGRAPHY	14
2.1.1 <i>Interactions of Neutrons with Matter.....</i>	<i>14</i>
2.1.2 <i>Neutron Interactions and Macroscopic Cross Sections.....</i>	<i>14</i>
2.1.3 <i>Mathematical and physical foundations of Neutron Radiography.....</i>	<i>15</i>
2.2 NEUTRON TOMOGRAPHY	17
2.2.1 <i>Tomography Reconstruction.....</i>	<i>17</i>
2.2.2 <i>The Method of Filtered Backprojection.....</i>	<i>18</i>
3 EXPERIMENTAL FACILITIES	23
3.1 NEUTRON IMAGING FACILITIES AT ATI.....	23
3.1.1 <i>Neutron spectrum.....</i>	<i>25</i>
3.1.2 <i>The measured spectrum of the NR II beam line.....</i>	<i>26</i>
3.1.3 <i>Collimator.....</i>	<i>28</i>
3.2 ANTARES EXPERIMENTAL SETUP.....	31
4 UPGRADING OF THE NR-NT FACILITY AT ATI.....	36
4.1 DETECTOR SELECTION.....	36
4.2 CHARACTERIZATION OF THE DETECTORS	38
4.2.1 <i>Thin-plate scintillation detector.....</i>	<i>39</i>
4.2.2 <i>Imaging plate detector.....</i>	<i>43</i>
4.3 .SUMMARY	48
APPLICATIONS.....	51
5 ST. STEPHANS CATHEDRAL PROJECT.....	52
5.1 INTRODUCTION.....	52

5.2	RESTORATION PROCEDURE AND SAMPLE PREPARATION	52
5.3	NEUTRON STUDIES ON FRESHLY PREPARED LIME-SANDSTONES	53
5.4	NR AND NT INVESTIGATIONS OF SAMPLES FROM ST. STEPHAN'S FACADE.....	57
5.5	ALTERNATIVE INSPECTION METHODS.....	61
5.6	CONCLUSIONS.....	65
6	INVESTIGATIONS OF STONE CONSOLIDANTS BY NEUTRON IMAGING.	67
6.1	INTRODUCTION.....	67
6.2	THE CONSOLIDANTS	67
6.3	SAMPLE CHARACTERIZATION AND TREATMENT	68
6.4	EXPERIMENTAL PROCEDURE AND RESULTS	69
6.4.1	<i>Comparison of ethyl silicate and paraloid 5% measured at ATI.....</i>	<i>70</i>
6.4.2	<i>Comparison of ethyl silicate and paraloid 5% measured at ANTARES.....</i>	<i>71</i>
6.4.3	<i>Experiments with reduced concentration of Paraloid B72 on real weathered samples.....</i>	<i>72</i>
6.4.4	<i>Time series experiments with different strengtheners.</i>	<i>73</i>
6.5	SUMMARY AND OUTLOOK:.....	74
7	NEUTRON SOURCES.....	75
7.1	SAMPLES INVESTIGATED	76
7.1.1	<i>Plutonium-Beryllium (α, n) Sources.....</i>	<i>76</i>
7.1.2	<i>Americium-Beryllium (α, n) Sources.....</i>	<i>77</i>
7.2	MEASUREMENTS AND RESULTS.....	77
7.2.1	<i>Neutron Radiography measurements.....</i>	<i>77</i>
7.2.2	<i>Neutron tomography measurements</i>	<i>84</i>
7.3	CONCLUSIONS AND OUTLOOK	86
8	TEXTILE FIBERS.....	88
8.1	INTRODUCTION.....	88
8.2	EXPERIMENTS AND RESULTS.....	88
8.2.1	<i>Dynamic neutron radiography.....</i>	<i>88</i>

8.2.2	<i>Experiments of fibers enclosed in pillows</i>	89
8.2.3	<i>Imaging plate neutron radiography measurements</i>	91
8.2.4	<i>Imaging of fiber samples enclosed in plastic bags</i>	96
8.3	OUTLOOK.....	96
9	HYDROGEN TRANSPORT STUDIES.....	98
9.1	INTRODUCTION.....	98
9.2	HYDROGEN DETECTION SENSITIVITY IN THIN MATERIALS AT ATI.....	98
9.3	INVESTIGATION OF LIQUID TRANSPORT BY DYNAMIC NR.....	101
9.4	NR SERIES OF THE IMBIBITION OF H ₂ O WITH THERMAL NEUTRONS AT ATI.....	103
9.5	NR SERIES OF THE IMBIBITION OF H ₂ O WITH COLD NEUTRONS AT ANTARES.....	105
9.6	X-RAY INVESTIGATION.....	107
10	SOME MORE APPLICATIONS.....	110
10.1	MEASUREMENT OF POROSITY	110
10.2	BORON ALLOYED STEELS.....	114
11	CONCLUSION AND OUTLOOK.....	118
12	APPENDIX I.....	120
12.1	NR INVESTIGATIONS OF WEAK, FAIR AND STRONG ABSORBERS.....	120
12.2	LABVIEW PROGRAM FOR THE SHUTTER	122
12.3	GOLD CHAIN	123
13	APPENDIX II – NT OF RESTORED ORIGINAL SAMPLES.....	125
13.1	SAMPLE 1	125
13.2	SAMPLE 2	126
13.3	SAMPLE 3	127
13.4	SAMPLE 4	128
13.5	SAMPLE 5	129
	LIST OF ABBREVIATIONS	131
	LIST OF FIGURES.....	133

LIST OF PUBLICATIONS 140

14 REFERENCES..... 143

1 INTRODUCTION

At the Atomic Institute (ATI), Vienna we have a low power TRIGA Mark II research reactor. This reactor at ATI has a long tradition of neutron imaging. Two beam lines have been devoted to neutron imaging, NR I and NR II. Initially neutron radiography was performed with the film method at NR I. Later the system was digitized at NR II.

In the framework of this thesis, the experimental setup at NR II has been upgraded with the acquisition of a new scintillation detector and an imaging plate detector. An automatic nitrogen filling system has been installed. The detection system and the instrument infrastructure were continuously improved in order to optimize the experiment results and to make the experimental work more flexible. This has led to an improved spatial resolution, better sensitivity and the possibility of longer measurements for the utilization of the full dynamic range. The key detector features have been analyzed for their use in neutron radiography and neutron tomography. Our experiences indicate the feasibility of the deployment of mobile neutron sources for imaging with improved spatial resolution and sensitivity.

The neutron interaction with matter and the upgraded instrumental setup has been utilized for promising applications in the fields of engineering and geology. X-rays do not possess high penetration ability into the materials having high atomic number. Elements having small atomic number like H-1, D-2, Li-6, B-10 etc. cannot give contrast with X-ray radiography contrary to neutron radiography. Even the purely qualitative inspection has provided valuable results, particularly because it is possible to penetrate materials (e.g. metals), that are opaque for X-rays. On the other hand, the sensitivity for certain light elements (e.g. hydrogen) is very high, while they are almost invisible for X-rays. Neutrons are able to distinguish between different isotopes and neutron radiography is an important tool for studies of radioactive materials. X-ray measurements have also been performed to show a comparison. The complementarity of neutrons and X-rays can lead to a complete visualization of a sample and hence is of great importance. The samples studied were ideally suited for neutrons based on the properties of the interaction of neutrons with matter.

Introduction

Projects based on the hydrogen sensitivity of this method to study the transport of hydrogen in building materials and textile fibers have been carried out. Investigation of boron alloyed steels used in the nuclear industry. Sealed radioactive neutron sources have been imaged non-destructively to get information about their geometry and material.

Neutron imaging has been successfully applied for conservation and restoration of building materials. Evaluation of distribution and penetration of the stone consolidants is very important for historical buildings and monuments. This technique has been utilized to assess the restoration work at the St. Stephans cathedral which dates back to the 12th century. The selection of a suitable strengthener is very important to achieve a successful restoration. Different strengtheners were studied using this method. Studies have been performed for the restoration and conservation work of historical buildings and monuments. Neutron imaging was also performed for the structural studies of rocks, to perform porosity analysis to be used for the investigation of deformation bands.

Isotopic neutron sources have been available for more than six decades. At the Atomic Institute, different neutron sources are in use for instrument calibration and fast neutron applications but we have only little information about their construction and densities. The knowledge of source design is essential for a complete MCNP5 ((Monte Carlo Neutron Particle Transport) code modeling of the experiments. Neutron radiography (NR) and neutron tomography (NT) are the best choices for the non-destructive inspection of the source geometry and homogeneity. From the transmission analysis we gain information about the shielding components and the densities of the radio-isotopes in the cores. Three neutron sources, based on (alpha, n) reaction, have been investigated, two $^{239}\text{PuBe}$ sources and one $^{241}\text{AmBe}$ source. In the NR images the internal structure was clearly revealed using high-resolving scintillation and imaging plate detectors. In one source tablet a crack was detected which causes asymmetric neutron emission. The tomography inspection of strong absorbing materials is more challenging due to the low beam intensity of $1.3 \times 10^5 \text{ n/cm}^2\text{s}$ at our NT instrument, and due to the beam hardening effect which requires an extension of reconstruction software. The tomographic inspections of a PuBe neutron source and appropriate measures for background and beam hardening correction have been presented.

Introduction

Tencel Lyocell fibers are used in duvets. The basic requirement of a quilt is thermal insulation. During sleep the human body perspires, therefore moisture management of the duvet is essential for a comfortable sleep. The release of humidity has to be accommodated by the quilt. Hence moisture absorption and humidity transport are very important when designing a coverlet. Neutron imaging is suitable for studying moisture transport processes due to the sensitivity of neutrons for hydrogen. Neutron radiography was used to investigate the moisture distribution in textile fibers under praxis conditions. Real time neutron radiography made it possible to follow the dynamics of the moisture transport without disturbing the ensemble during measurement.

Dynamic neutron radiography has been performed to study the diffusion of liquids that is water and different stone strengtheners in stones. Due to the sensitivity of neutrons to hydrogen, hydrogen transport studies are an interesting and useful application of this method. Previously such studies have been demonstrated at the ATI at the older setup with the film method. In this research work these studies were done using the digital setup employing a higher dynamic range. The diffusion of water and stone consolidants in building materials has been studied according to the interest of geologists and conservators.

2 NEUTRON IMAGING

2.1 Neutron radiography

2.1.1 Interactions of Neutrons with Matter

Neutrons interact with nuclei in a variety of ways [Lamarsh, 1965]. For instance, if the nucleus is unchanged in either isotopic composition or internal energy after interacting with a neutron, the process is called *elastic scattering*. On the other hand, if the nucleus, still unchanged in composition, is left in an excited state, the process is called *inelastic scattering*. In referring to these interactions it is common to say that the incident neutron has been “scattered”, elastically or inelastically, as the case may be, because a neutron reappears after the interaction. However, this term is somewhat misleading, since the emerging neutron may not be the same neutron that originally struck the nucleus. Neutrons disappear as the result of *absorption* reactions.

2.1.2 Neutron Interactions and Macroscopic Cross Sections

The radiography process must use a radiation which has a high probability of reacting with the material of the sample, and it is usual to describe this probability of interaction as an effective target size called *cross-section* [Domanus, 1992]. There are several types of cross-section but the two that are of principal interest to neutron radiographers are the *absorption cross-section* and the *scattering cross-section*. The total cross-section is the sum of these two. This microscopic cross-section is represented by σ .

The neutron transmission through a sample, ideally for a thin, homogeneous, monochromatic and collimated beam, may be expressed by considering the rate at which the neutron intensity reduces as it passes through the sample material. This is given by:

$$\frac{-dI(x)}{dx} = I(x)\sigma N \quad 2.1$$

Where

I – neutron intensity, i.e. number of particles across unit area in unit time, $\text{n.cm}^{-2}\text{s}^{-1}$

x – specimen thickness, cm;

Neutron Imaging

σ - microscopic cross-section, cm^{-2}

N – number of target nuclei per unit volume, cm^{-3}

Rearranging and integrating give:

$$I = I_0 e^{-N\sigma x}$$

2.2

Where

I – neutrons transmitted through the sample, $\text{n.cm}^{-2}\text{s}^{-1}$

I_0 - neutrons incident upon the sample, $\text{n.cm}^{-2}\text{s}^{-1}$

The equation above is also referred to as ‘The law of exponential attenuation’ or Beer Lambert’s law.

2.1.3 Mathematical and physical foundations of Neutron Radiography

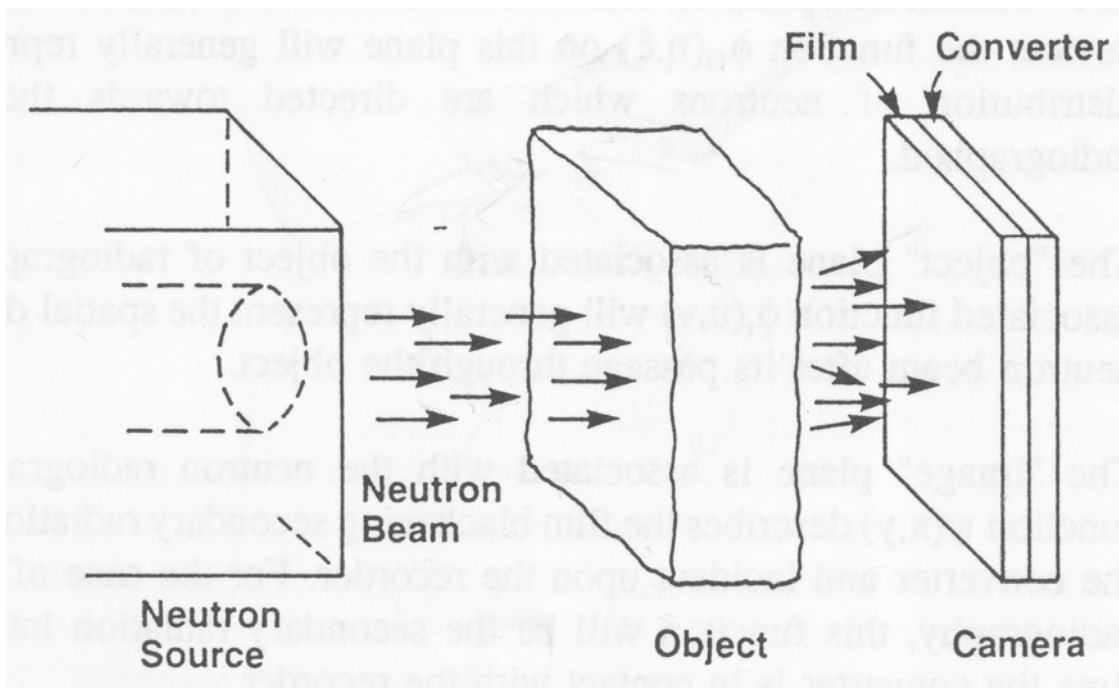


Figure 2-1: Principal components of a neutron radiography system [Domanus, 1992].

Neutron Imaging

Neutron radiography involves three main components:

- a) a suitable neutron beam,
- b) an object of radiographic interest,
- c) a device to record-promptly or latently – the radiation intensity information associated with the neutron beam transmitted through the object.

Figure 2-1 provides a graphical depiction of these three system components for the case of a non-radioactive object specimen. In order to provide mathematical and physical basis of the various processes which take place in neutron radiography we need to define the following terms which are depicted in Figure 2-2

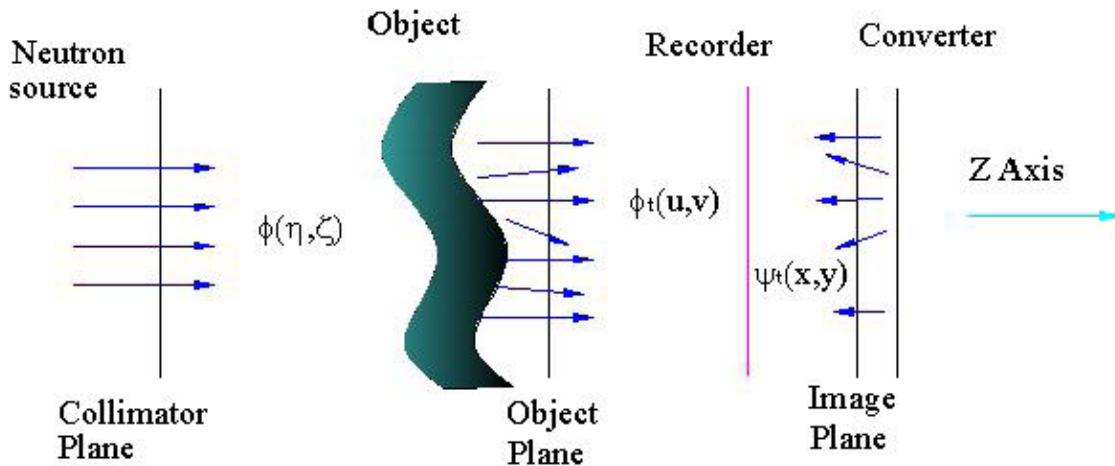


Figure 2-2: Illustration showing the association of various radiation flux quantities with functional planes and system components [Domanus, 1992; Mishra, 2005].

(η, ζ) = The “collimator” plane associated with the neutron beam from a collimator device; the function $\phi(\eta, \zeta)$ on this plane will generally represent the spatial distribution of neutrons which are directed towards the object to be radiographed.

(u, v) = The “object” plane is associated with the object of radiographic interest; the associated function $\phi_t(u, v)$ will generally represent the spatial distribution of the neutron beam after its passage through the object.

(x,y) = The “image” plane is associated with the neutron radiographic image; the function $\psi(x,y)$ describes the film blackening secondary radiation emerging from the converter or the photo stimulated luminescence in case of image plates and incident upon the recorder.

The flux $\phi(\eta,\zeta)$ is fully determined by the characteristics of the neutron source and the collimator device. The flux $\phi_t(u,v)$ depends upon the flux $\phi(\eta,\zeta)$ and the object. The function $\psi(x,y)$ represents a flux of a certain type of radiation induced by the neutrons from the $\phi_t(u,v)$ beam captured in the converter. Hence $\psi(x,y)$ is a function of $\phi_t(u,v)$. However the end result is the optical density or gray level $D(x,y)$ on the film or the image plate. The radiographic process can be illustrated by the following sequence of functions:

$$\phi(\eta, \zeta) \rightarrow \phi(u, v) \rightarrow \psi(x, y) \rightarrow D(x, y) \quad 2.3$$

For the object, both neutron scattering and absorption will generally be possible, so the total cross-section at a coordinate z is given by

$$\Sigma_t(z) = \Sigma_a(z) + \Sigma_s(z) \quad 2.4$$

Further details about the consequent mathematics and physics of neutron radiography with applications can be found in [Harms, 1986].

2.2 Neutron Tomography

2.2.1 Tomography Reconstruction

Computed neutron tomography is an interesting application of digital image processing. It is a method in which a series of two dimensional projections (radiography images) can be reconstructed to get a three dimensional view of the internal structure of the sample. The term ‘Neutron computed tomography’ is usually used for the reconstruction of a 3D voxel array representing the inner structure of the sample on the basis of 2D neutron transmission images of an object taken from different view angles.

2.2.2 The Method of Filtered Backprojection

The theory of tomographic reconstruction using parallel beams has been extensively described in [Kak, 1988]. The reconstruction of the macroscopic cross section $\Sigma(x, y, z) = N(x, y, z)\sigma$ from the transmission data T is represented by Figure 2-3:

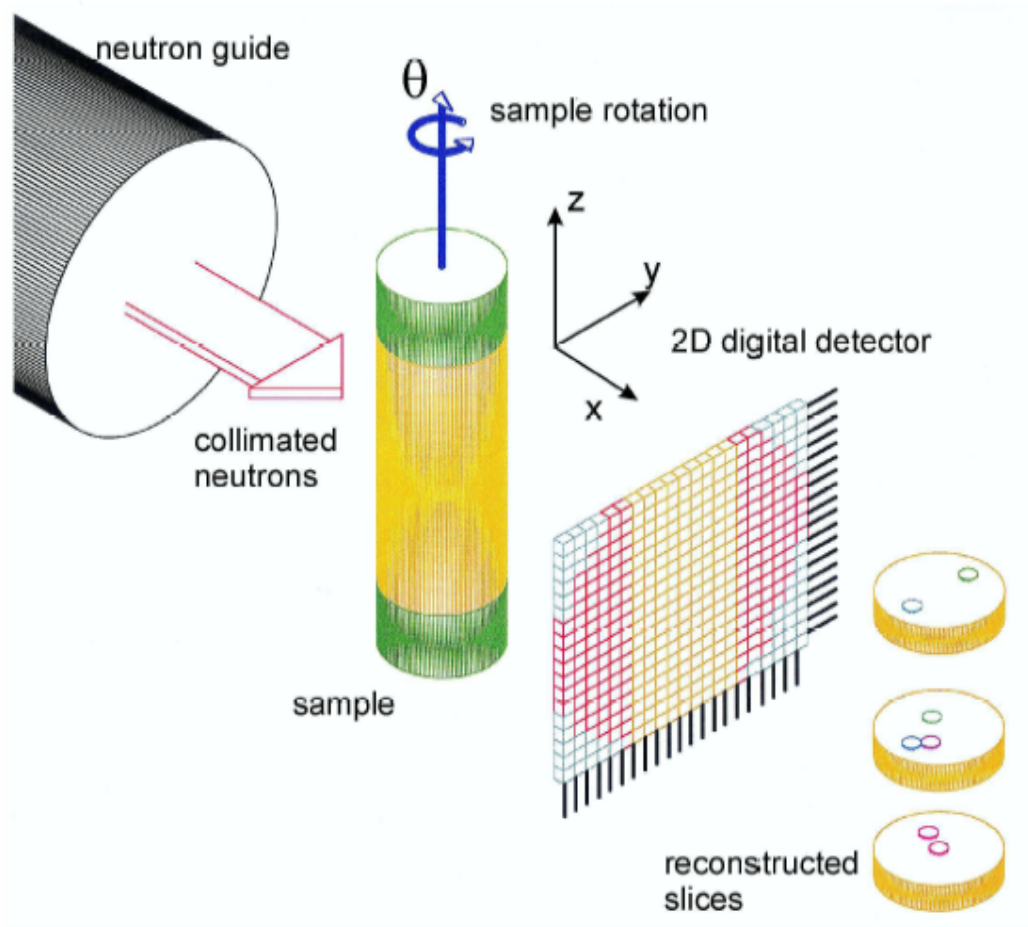


Figure 2-3: Utilization of the transmission signal for the tomographic reconstruction of the cross-section $\Sigma(x, y, z)$ [Zawisky].

$$T(\theta, t, z) \cong \exp - \int_{ray} \sum_i N_i(x, y, z) \sigma_i ds \quad 2.5$$

$$\text{Objectfield for a mixture of isotopes} = \sum_i N_i(x, y, z) \sigma_i \quad 2.6$$

The individual (x, y) slices are reconstructed independent from each other, a 3D-rendering of all the slices then follows. A monochromatic beam would be described with the help of the polar coordinates (θ, t) whereas the sample coordinates will be represented by the Cartesian coordinates (x, y). The first step is to reconstruct a linear relationship between transmission and the object field. This procedure is represented as a projection in Figure 2-4.

$$P(\theta, t) \equiv -\ln T(\theta, t) \cong \int_{ray} \sum_i \Sigma_i(x, y) ds$$

2.7

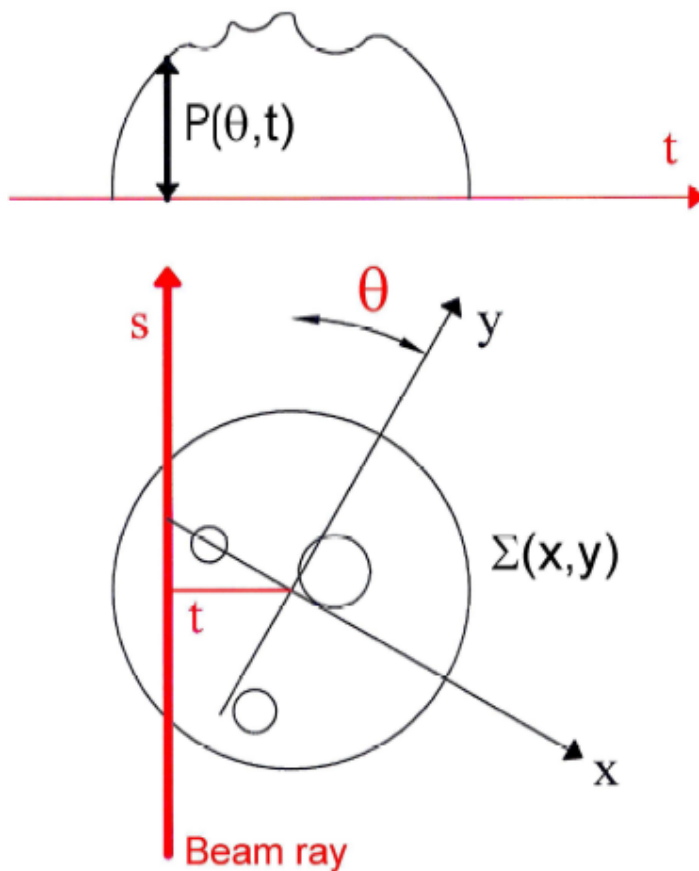


Figure 2-4: Principle of tomographic projection

The transformation *Objectfield* → *Projection* is called Radon-Transformation [Kak, 1988]:

$$P(\theta, t) \cong \int_{-\infty-\infty}^{\infty} \int_{-\infty-\infty}^{\infty} \sum_i \Sigma_i(x, y) \delta(x \cos \theta + y \sin \theta - t) dx dy$$

2.8

Neutron Imaging

The inverse problem, the calculation of the objectfield from the projections, is called Inverse Radon transformation, a special realization is the filtered backprojection (FB). The main features of the FB have been sketched in Figure 2-5 below. According to the Fourier slice theorem, the Fourier transformation of projection $P(\theta, t)$ defines a line in the Fourier space $F(\theta, u, v)$. We substitute the coordinates (u, v) for the Fourier space with $u = \omega \cos\theta$ and $v = \omega \sin\theta$:

$$F(\theta, u, v) = \int_{-\infty}^{\infty} P(\theta, t) e^{-i2\pi\omega t} dt = \int_{-\infty}^{\infty} \int_{-\infty}^{\infty} \Sigma_i \Sigma_i(x, y) e^{-i2\pi\omega(x\cos\theta + y\sin\theta)} dx dy \quad 2.9$$

$$F(\theta, u, v) = \int_{-\infty}^{\infty} \int_{-\infty}^{\infty} \Sigma_i \Sigma_i(x, y) e^{-i2\pi(ux+vy)} dx dy \quad 2.10$$

Each projection defines a line in Fourier space. For a sufficient number of projections, the Fourier space can be sufficiently filled. Afterwards the object field can be reconstructed by the inverse Fourier transform of F .

$$\Sigma_i \Sigma_i(x, y) = \int_{-\infty}^{\infty} \int_{-\infty}^{\infty} F(\theta, u, v) e^{i2\pi(ux+vy)} du dv \quad 2.11$$

However during this direct back projection, the higher frequencies are underrepresented therefore an additional filter is implemented to strengthen the high frequency portion (filtered back projection).

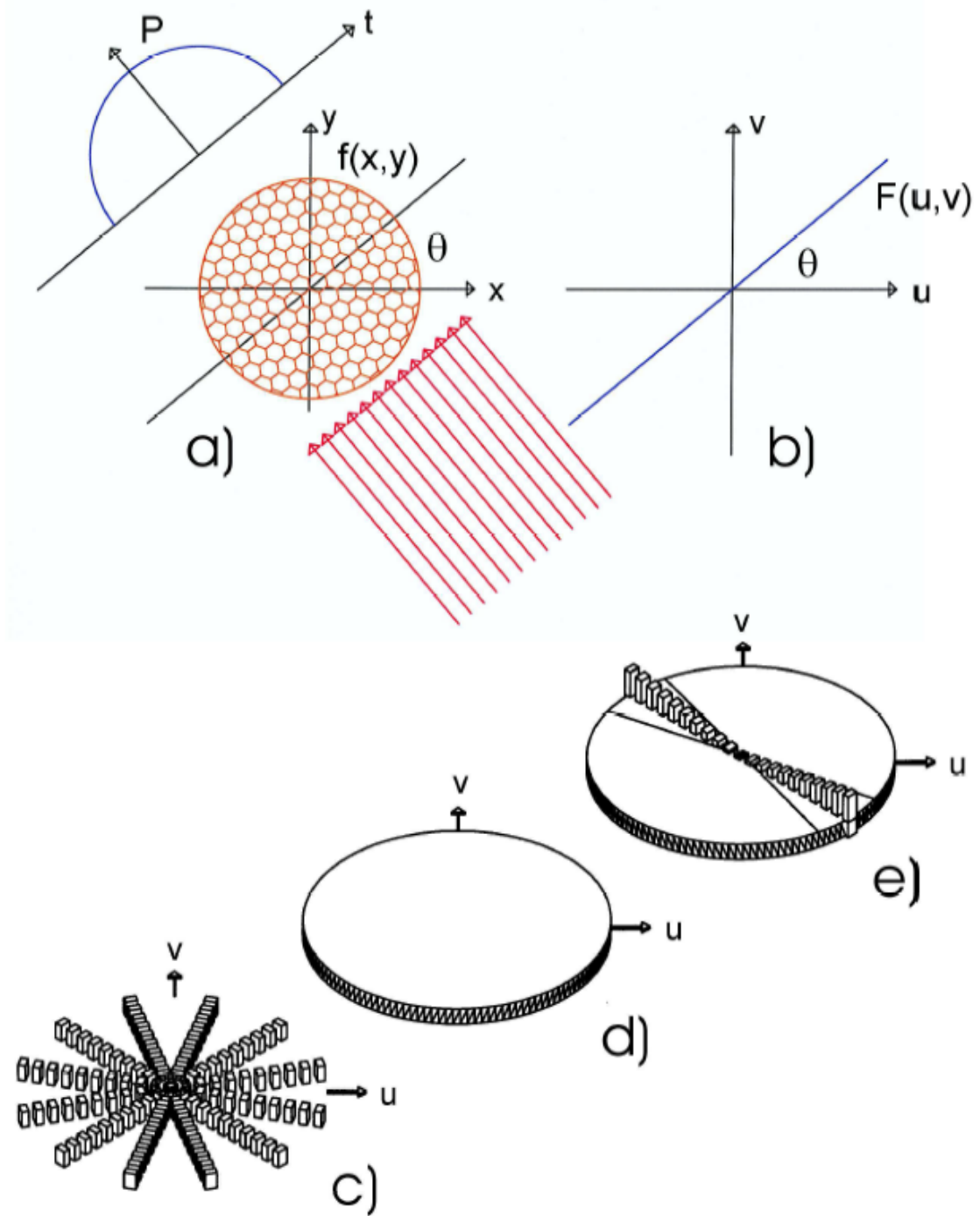


Figure 2-5: Tomographic Reconstruction with filtered backprojection: a) Calculation of the projection data. b) +c) each projection defines a line in Fourier space. d) Ideal occupation of the Fourier space in the limit of a large number of projections. e) The high-frequency part from the backprojection is amplified.

Neutron Imaging

The simplest filter is the ramp filter that strengthens the frequency regions linearly with frequency ($F_{\text{filtered}} = F \times |\omega|$). We have chosen a Shepp-Logan filter for our applications. Subsequently, slices of the object are reconstructed independent of each other and then merged to a 3D object. This step is designated as 3D-rendering. By changing the opacity, different regions of the sample can be represented with different transparency. Through segmenting and coloring, regions with different transmission or absorption (density) can be emphasized. With the help of special softwares, quantitative information about the grain sizes and distributions can be obtained. With such an analysis, only the objectfield, which is our case, is the distribution of the macroscopic cross-section is reconstructed. A measurement with X-rays would give a different result which will be complementary to the neutron tomography. The tomography visualization is a complete illustration but only related to a special reciprocal effect.

3 EXPERIMENTAL FACILITIES

3.1 Neutron imaging facilities at ATI

At the ATI we have a TRIGA Mark II reactor. This is purely a research reactor of the swimming-pool type. The maximum continuous output is 250 kW (thermal). Figure 3-1 shows several experimental setups that have been developed at the neutron beam lines for material investigations and fundamental physics research based on neutron techniques. These are: NR-NT (neutron radiography and tomography), USANS (Ultra Small Angle Scattering), Neutron interferometry, NAA (Neutron Activation Analysis) and Depolarisation analysis

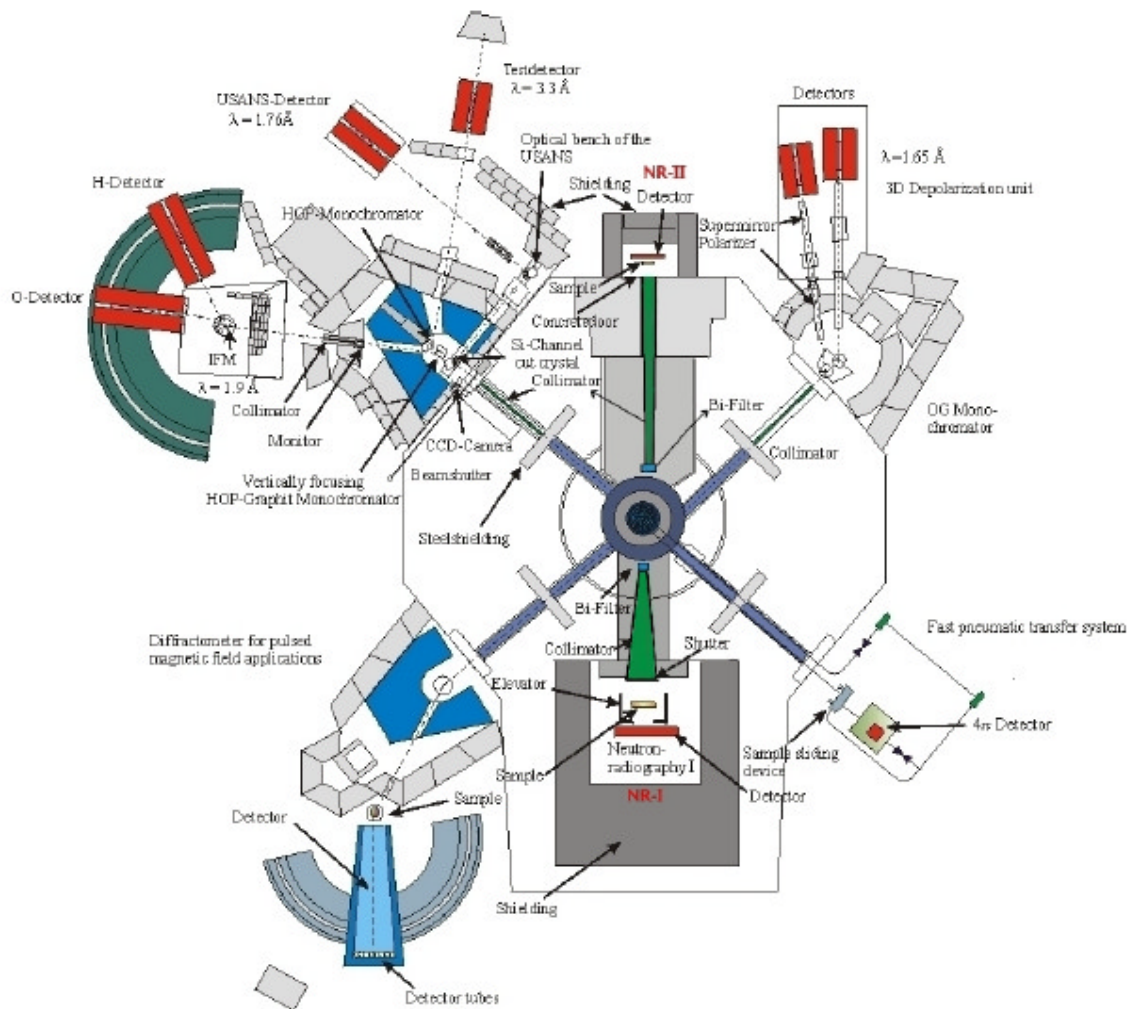


Figure 3-1: *The neutron beam lines at the TRIGA Mark II research reactor.*

Experimental facilities

NR I and NR II are two beam lines at ATI that are dedicated to neutron imaging. These facilities have been shown in Figure 3-1. NR I is based on the film/converter method. Station 1 is located at a radial thermal beam channel of the TRIGA reactor. Station 2 is located at the thermal column of the TRIGA reactor, as shown in Figure 3-1. The digitized neutron imaging setup was installed at NR II. It has a lower neutron flux and a smaller beam diameter, but a higher L/D ratio compared to NR I. This beam position was chosen due to the advantage of easy access to the sample position during reactor operation. At NR I the sample position is located in an irradiation room that cannot be accessed during reactor operation and also several hours after shutdown due to the high radiation level. A vertical elevator system is used to transport samples to the beam position. Another advantage is the collimation ratio which is an important parameter for spatial resolution. The L/D ratio at NR I is 50, which is not sufficient to generate sharp images. Figure 3-2 shows the components of the both NR facilities [Bastürk, 2003] .

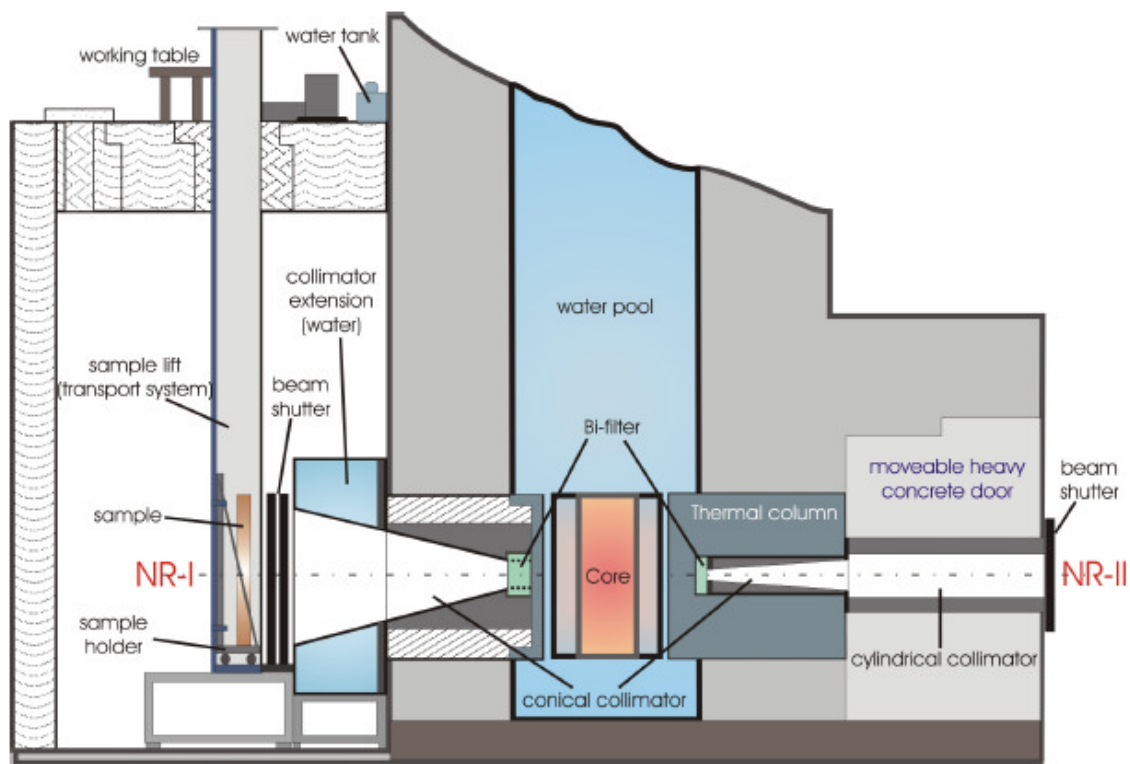


Figure 3-2: *NR facilities at TRIGA Mark II research reactor.*

3.1.1 Neutron spectrum

Bonner Sphere Spectroscopy (BSS) was used to measure the spectral distribution of neutron fluence rate at the thermal column by [Hajek, 2001] . A Bonner sphere spectrometer (BSS) consists of a detector for thermal neutrons located in the centre of polyethylene moderating spheres. Polyethylene (CH₂)_n is used as it is an ideal moderating material for neutrons due to its high concentration of elements like hydrogen and carbon which have a low atomic number. These spheres are available in different diameters and are used according to the requirements of the problem. Depending on the diameter of the sphere, a fraction of neutrons gets moderated until a thermal equilibrium is established with the atoms of the surrounding medium. The detector in the centre of the BSS can then detect these neutrons. The detector in the BSS used for this measurement was a ⁶LiI(EU)-scintillation counter optically coupled to a photo multiplier tube with connected pre-amplifier.

The spectrum of neutrons after moderation in the graphite block of the thermal column was confirmed to be a Maxwellian distribution. The fast neutron component (10 to 12 MeV) at this position is negligible. Equation (3.1) gives the number of neutrons dn per volume element with energies between E and E + dE as approximated by a Maxwellian distribution.

$$dn = n(E) = \frac{2\pi n}{(\pi kT)^{3/2}} \exp(-E/kT) \sqrt{E} dE \quad (3.1)$$

Monte Carlo Neutron Transport program was used to simulate the measurements with BSS to determine the response of the detector at different sphere diameters for the same detector material. The density of the thermalized neutrons inside the Bonner spheres is measured by the ⁶LiI scintillator. The deconvolution was performed with a computer program. Φ , the neutron fluence, is the quotient of dN by dA, where dN is the number of particles incident on a sphere of cross-sectional area dA. The neutron fluence rate ϕ is the quotient of d Φ by dt where d Φ is the increment of neutron fluence in the time interval dt as shown in equation (3.2).

$$\phi(t, r) = \frac{d\Phi(r)}{dt} = \frac{d^2N}{dt dA} (m^{-2}s^{-1}) \text{ and } \phi = \int_0^{\infty} n(v) v dv \quad (3.2)$$

3.1.2 The measured spectrum of the NR II beam line

The neutron spectrum behind the heavy concrete door at the thermal column was measured with BSS method [Hajek, 2002]. The Maxwellian distribution of neutron fluence and density of NR II beamline is shown in Figure 3-3.

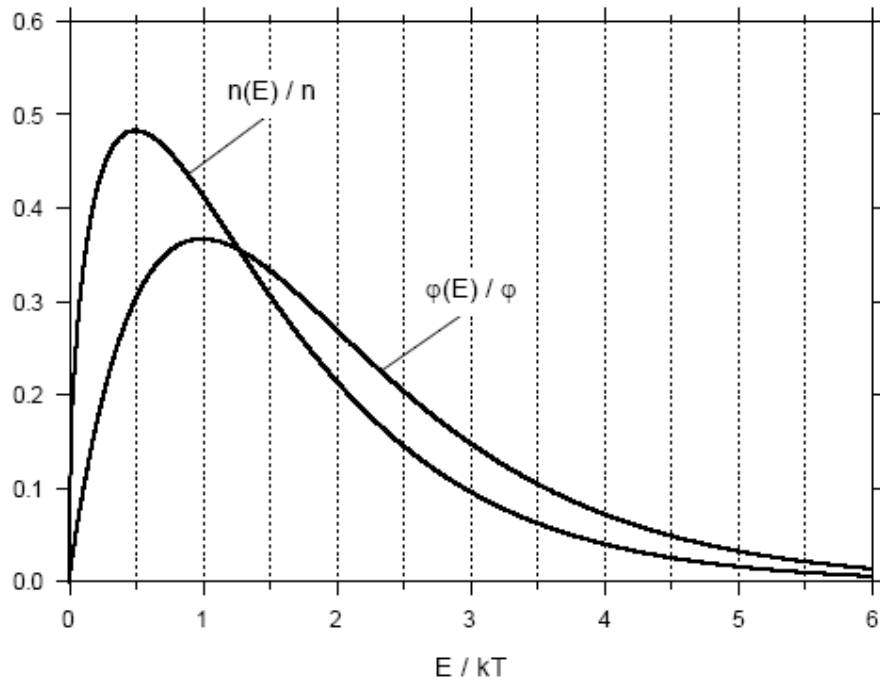


Figure 3-3: *The Maxwellian distributions of neutron fluence and density of NR II.*

The plot of the distributions of neutron density and neutron fluence versus E/E_T in Figure 3-3, clearly show that the distribution functions are peaked at $kT/2$ and kT , respectively. The unfolded and fitted neutron spectra at the thermal column of NR II facility are given in the graph in Figure 3-4

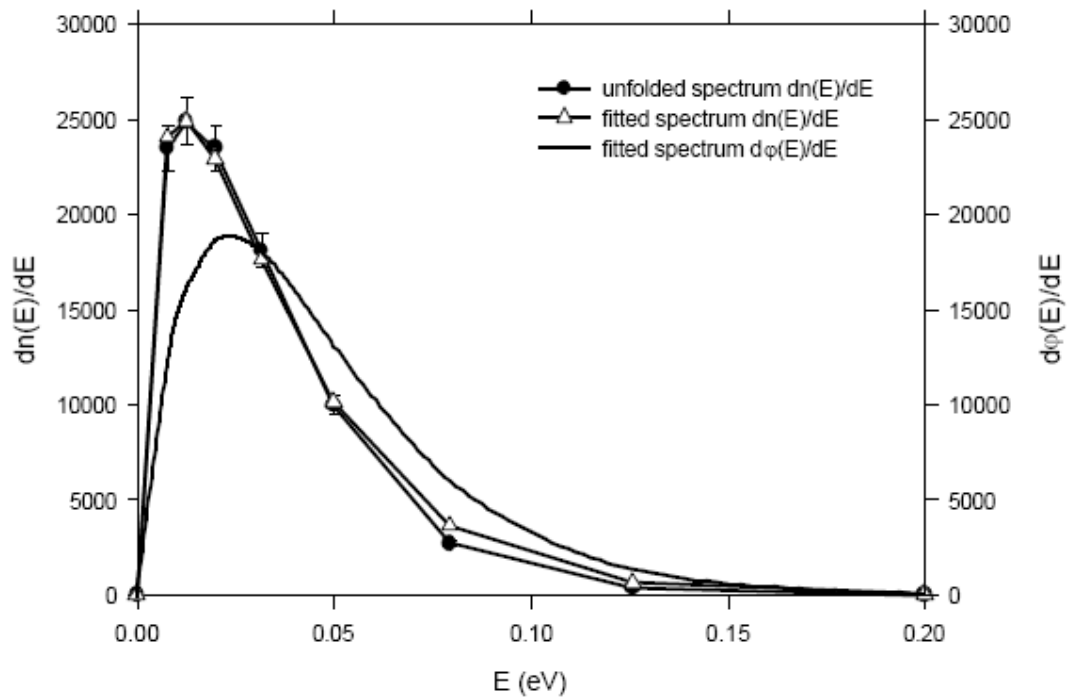


Figure 3-4: Unfolded and fitted neutron spectra at the thermal column of the TRIGA Mark II research reactor

Table 3-1 shows the calculated values for a thermal power of 250 kW_{th} with the assumption of a linear flux/power relationship. From these results it can be concluded that the contribution of the fast neutrons to the total flux is negligible. The BSS measurements have been carried out at a distance of 35cm from the graphite surface, behind the concrete door.

Table 3-1: Neutron flux at the thermal column of the TRIGA Mark II reactor measured with the Bonner spectrometer [Hajek, 2002].

	$\Phi (E < 0.4 \text{ eV}) (\text{cm}^{-2} \cdot \text{s}^{-1})$	$\Phi (E < 100 \text{ MeV}) (\text{cm}^{-2} \cdot \text{s}^{-1})$
$P_{\text{th}} = 5 \text{ W}_{\text{th}}$	1.07×10^3	1.08×10^3
$P_{\text{th}} = 250 \text{ kW}_{\text{th}}$	5.37×10^7	5.39×10^7

3.1.3 Collimator

The collimator at the NR-II facility has two parts. One part is conical and the second part is cylindrical. The first conical part is installed in the thermal column. It has a length of 130cm. The cylindrical part is installed in the movable heavy concrete door. The cylindrical part has a length of 127 cm. A schematic diagram has been shown in Figure 3-2.

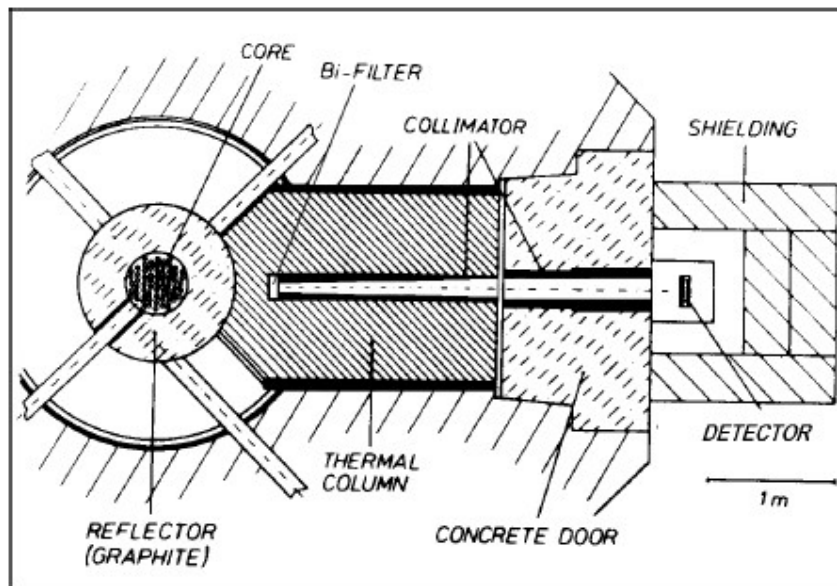


Figure 3-5: Floor plan of the NR II station at ATI.

The movable door facilitates the carrying out of measurements at a high neutron flux in the thermal column. The conical part of the collimator has an aperture of 2 cm and an outlet of 6cm. It has been placed in an outer shell of 10 cm x 10 cm. Figure 3-5 shows a 4 cm thick polycrystalline Bi for gamma filtering. The dimensions of the inner and outer diameter of the cylindrical part of the collimator are 8.2 cm and 20 cm respectively. Both collimators have been coated with CdB_4C on the inner side. Homogeneous neutron distribution can be provided for measurements at a high neutron flux behind the door by replacing the first part of the collimator with a graphite block of the same size.

Experimental facilities

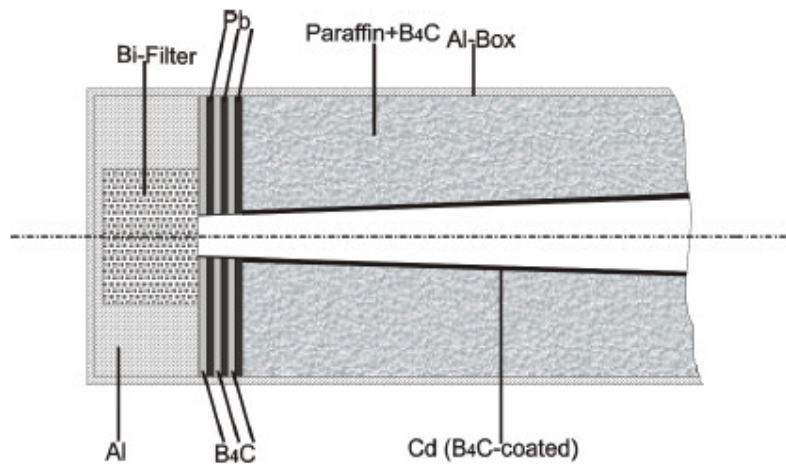


Figure 3-6: *The composition of the first part of collimator at NR II facility.*

The illuminator is a 30 cm thick graphite block between the aperture of the collimator and the aluminum reactor tank. The illuminator distributes the neutrons homogeneously before entrance into the collimator aperture. The required thickness of graphite illuminator for a NR facility is 10 – 15 cm. Excess thickness of illuminator leads to excess gamma content and reduction of neutron flux. At the NR II station, there is 20 cm excess graphite, which means that the neutron flux is reduced by a factor of 4. Figure 3-6 shows the 3 cm thick shielding material for neutrons and gammas surrounding the aperture. This shielding has 0.5 cm thick Pb and three 0.5 cm thick B₄C layers sandwiched together.

Table 3-2: *Table II: Basics characteristics of NR facilities at Atomic Institute – Vienna.*

	NR I Facility	NR II Facility
Neutron flux (cm ⁻² .s ⁻¹)	3 x 10 ⁵	1.3 x 10 ⁵
L/D (collimation) ratio	50	130
Cd-ratio	3	20
Beam diameter (cm)	40	9

Experimental facilities

Gamma background (Sv/h)	0.4	0.045
Source strength (n.s⁻¹)	3.8×10^8	7.0×10^6
Facilities	NR	NR and NT
Detection system	X – ray film/ Converter	CCD camera/ Scintillator/imaging plate

After the beam quality, the next important consideration is the detection system. A digital CCD camera system coupled to a scintillator was installed at NR II [Koerner, 2000]. The basic properties of the detection system are given in Table 3-3

Table 3-3: Table III. Properties and components of the nitrogen cooled digital CCD camera system at NR II.

Camera	Liquid nitrogen cooled Astrocama slow scan CCD camera
Camera chip	Sensitive area: 12.3 x 12.3 mm Sensitive pixel: 512 x 512 pixels Pixel size: 24 x 24 μm
Quantum Efficiency (QE)	Up to 90 % with standard AR coating
Digitization	16 bit digitization with 65535 gray levels
Lenses	Nikon NOKT 58 mm F 1.2 Nikon NOKT 180 mm F 2.8 Nikon NOKT 105 mm F 2.0
Mirror	2mm thick glass plate coated with Al and TiO ₂

A schematic representation of the digital system at NR II is given in Figure 3-7. The digital tomography system is based on the scintillator coupled to a CCD camera. The sample is placed on the rotary table between the shutter and the scintillator. The rotation of the sample is controlled with a stepper motor through a computer program.

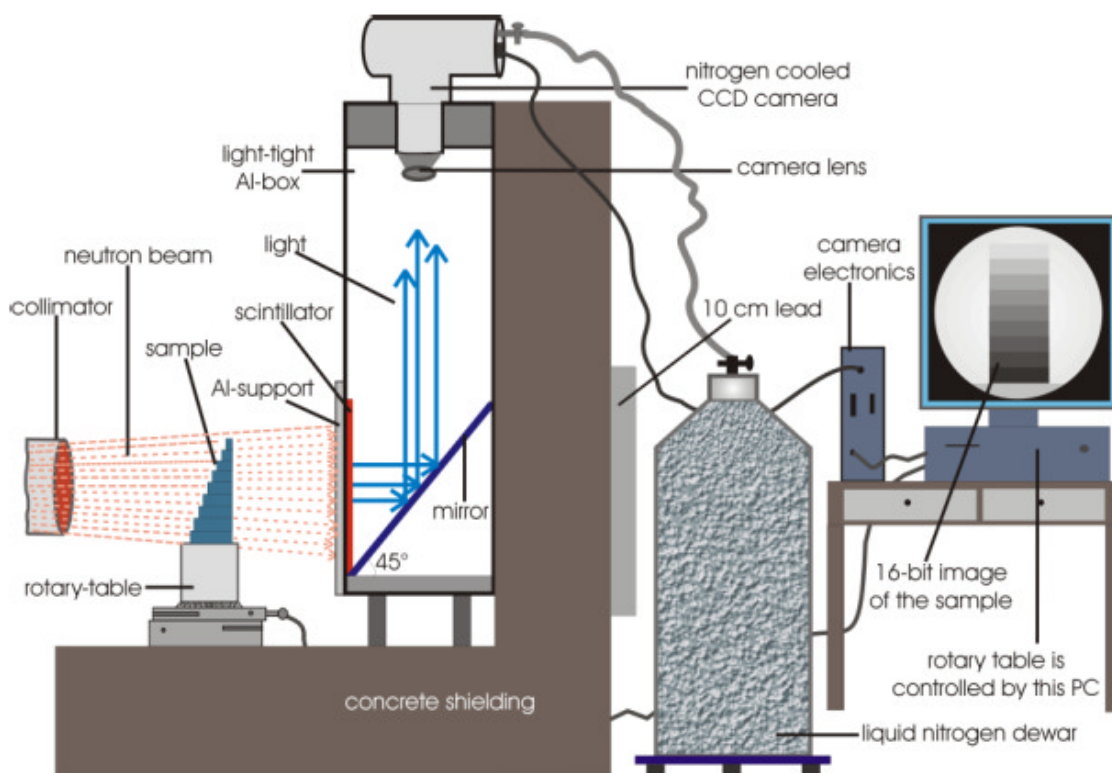


Figure 3-7: A schematic diagram of the digital detection system at NR II – ATI facility in Vienna

3.2 ANTARES Experimental Setup

Some experiments were performed at the cold neutron facility ANTARES (Advanced Neutron Tomography and Radiography Experimental Setup) at FRM II Munich (Forschungs Reaktor Muenchen) in Germany. This facility has a high neutron flux and hence a higher resolution and sensitivity. A description of the cold neutron instrumental setup is given below [Gruenauer, 2005].

Experimental facilities

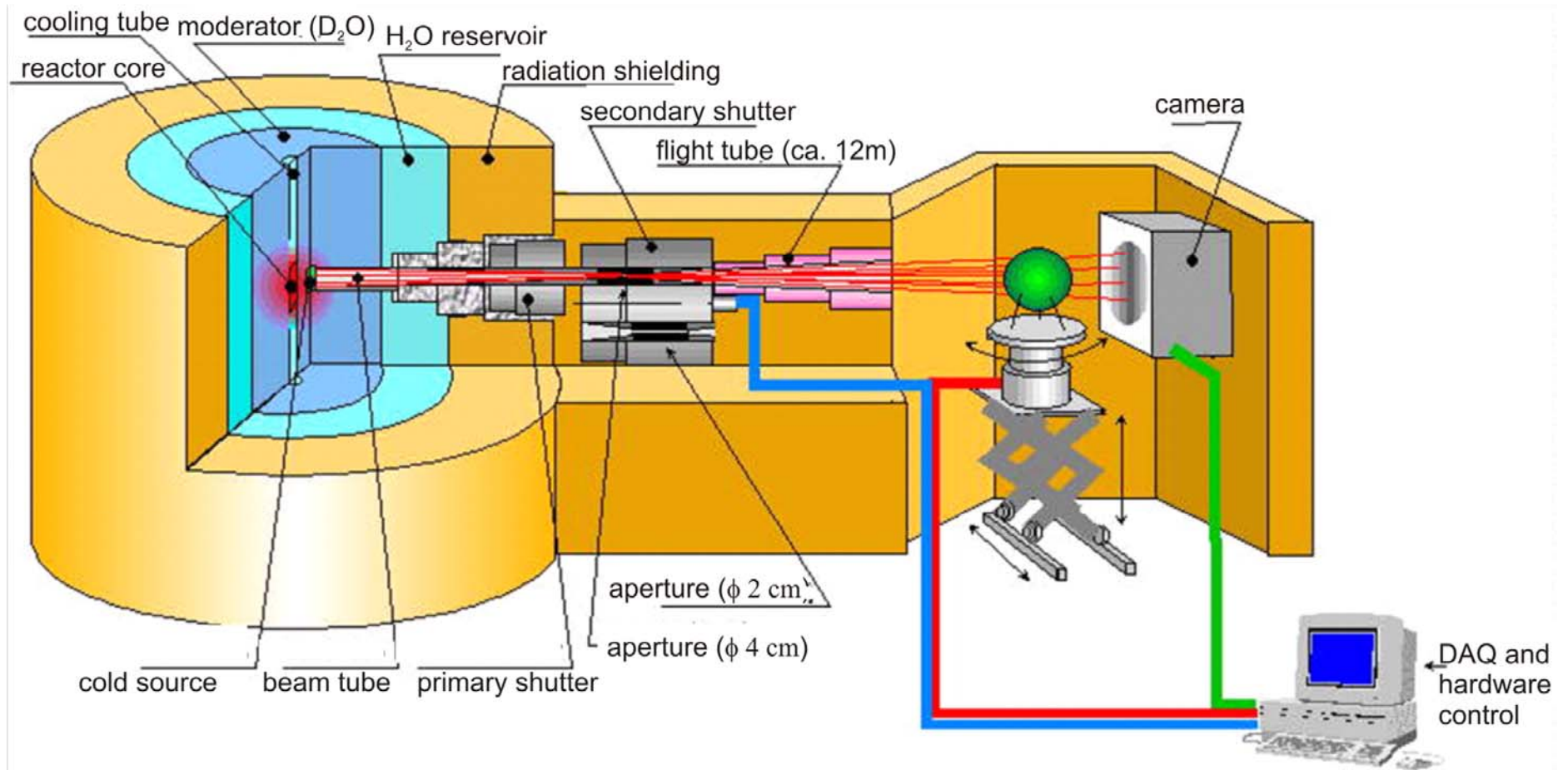


Figure 3-8: Schematic overview of ANTARES facility

Experimental facilities

Figure 3-9 shows the layout of the ANTARES facility. A secondary shutter has been installed adjacent to the biological shielding of the reactor. There is a possibility to change the L/D ratios to 400 and 800 by exchanging the collimator. An aperture wheel can move additional apertures into the beam. Different apertures required for different purposes like phase contrast radiography and coded masks can be moved in. A chamber for an energy selector is installed behind the aperture wheel (in the beam direction). Energy selective radiographies can be made with this energy selector to change contrasts of different elements depending on the neutron energy in the region of the Bragg cut-off. An X-ray tube which is mounted in the chamber for the energy selector can be moved to the beam axis when required.

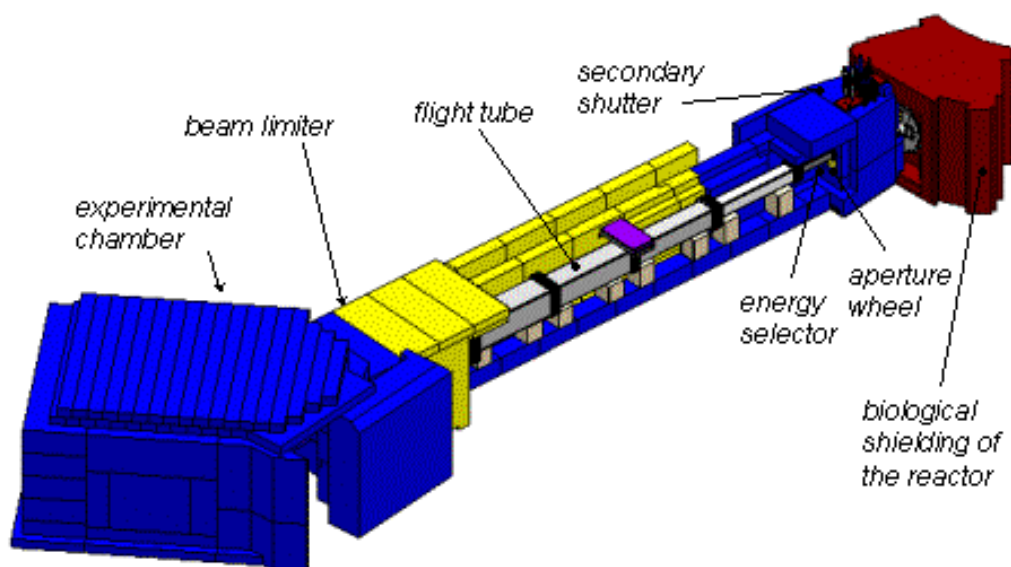


Figure 3-9: Setup of the ANTARES facility

Along the neutron flight path, a flight tube has been installed. Neutron scattering and absorption in air is reduced considerably by evacuating the flight tube down to a pressure of 0.1 mbar. With this arrangement, the flux at the specimen has been increased by 50%. A beam limiter is mounted at the end of the tube (at the entrance to the experimental chamber). The beam size can be adjusted to the size of the sample with the help of the beam limiter. Inside the experimental chamber, the sample is placed on a manipulator. The manipulator can move the specimen both in vertical and horizontal directions. For tomography measurements, the

Experimental facilities

sample can also be rotated. The detector has been placed behind the object. The direct beam is stopped with a beam catcher of lithium fluoride for minimization of background radiation.

Table 3-4: Some important beam parameters at location of the specimen

Parameter	L/D = 402.4	L/D = 792.5
Height of fully illuminated region	32 cm	36 cm
Width of fully illuminated region	32 cm	36 cm
Fully illuminated area	1.3E+3 cm ²	1.0E+3 cm ²
Neutron flux	9.4E+7 cm ⁻² s ⁻¹	2.5E+7 cm ⁻² s ⁻¹
Cd ratio	15	15
Gamma flux	4.2E+7 cm ⁻² s ⁻¹	1.0E+7 cm ⁻² s ⁻¹
Gamma dose rate	6.9E-1 Sv/h	1.7E-1 Sv/h
Neutron/gamma ratio	1.4E+8 cm ⁻² s ⁻¹ Sv ⁻¹ h	1.4E+8 cm ⁻² s ⁻¹ Sv ⁻¹ h

The spectral neutron flux density at location of the specimen in the ANTARES facility is shown in the graphs below.

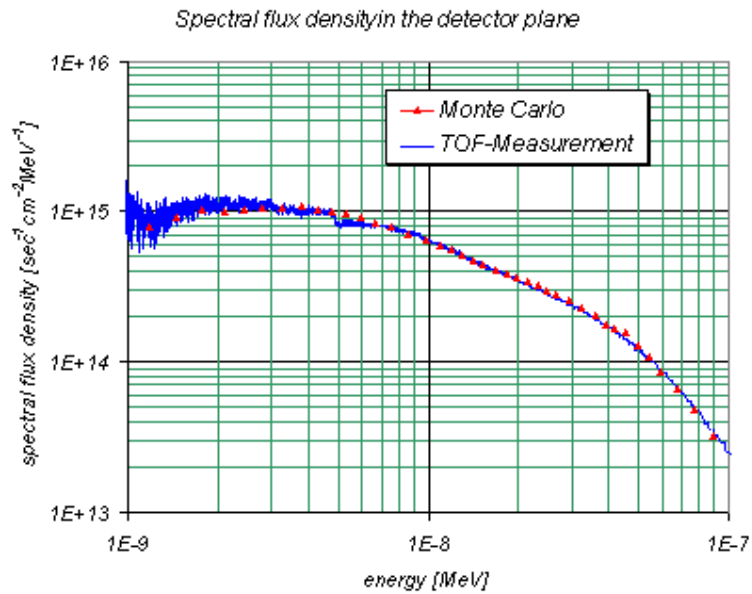


Figure 3-10: Spectral neutron flux density in the energy region between 1meV and 0.1eV

The spectral flux density in the energy region between 1 meV and 0.1 eV is depicted in Figure 3-10. While the spectral neutron flux density in the energy region between 0.1 meV and 1 MeV is illustrated in Figure 3-11.

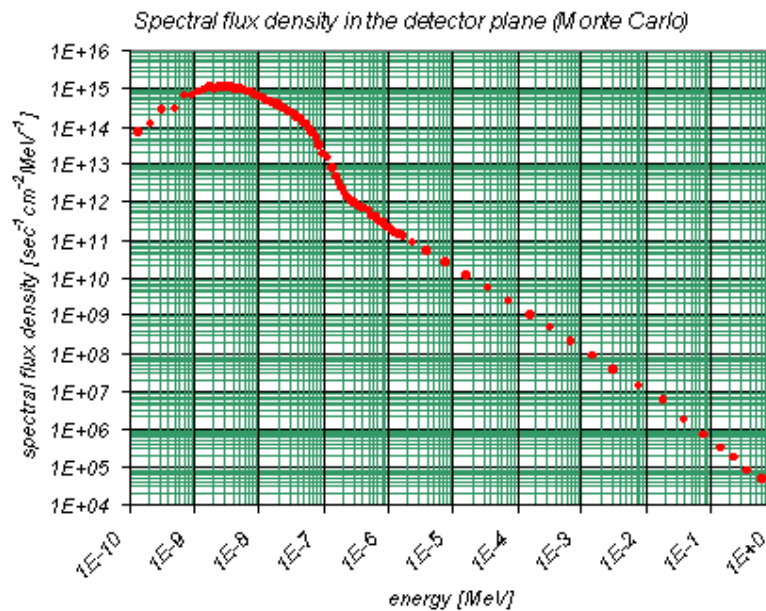


Figure 3-11: Spectral neutron flux density in the energy region between 0.1meV and 1MeV

4 UPGRADING OF THE NR-NT FACILITY AT ATI

At the Atomic Institute Vienna, with a 250kW TRIGA MARK II reactor, neutron imaging has a long tradition [Feigl, 1968; Harms, 1977; Rauch, 1977; Buchberger, 1989; Bayülken, 1990; Bruckner, 1999]. Gadolinium converter film detectors, despite their superior spatial resolution of up to 20 mm, have been widely replaced by digitized scintillator and imaging plate detectors. The advantages of digitized imaging detectors are linearity, reproducibility, and an increased image gradation due to 16 bit dynamic range compared to 7–8 bit on film. Higher detection efficiency is of particular importance in order to perform neutron tomography (NT) at a low intensity beamline with only 1.3×10^5 n/cm² s. Neutron imaging techniques present a challenging experimental task, especially at a low power research reactor.

Within the framework of a major instrument upgrade three digitized detectors have been installed, a 100 µm thin-plate scintillator, an imaging plate detector with 25 µm scanning resolution, and a ND&M micro-channel detector with 50 µm resolution. The advantages gained in this upgrade are being reported. Some key detector features are analyzed for their use in neutron radiography (NR) and tomography (NT). The strengths and limitations of each detector in the field of neutron radiography and tomography have been analyzed. It has been demonstrated that high resolution digitized imaging down to the 50 µm scale can be accomplished with weak beam intensities, if appropriate measures are taken for the inevitable extension of measurement times. Some selected applications of high resolution imaging have been presented in the next chapters. Our experiences indicate that the deployment of mobile neutron sources for imaging with improved spatial resolution is now feasible.

4.1 Detector selection

At a low-power reactor the signal-to-noise ratio becomes a major factor for neutron imaging. The distance between the radial tube of the neutron tomography station and the reactor core is only 3 m; therefore a 40 mm thick bismuth filter is placed at the collimator entrance for gamma reduction. The neutron beam has 9 cm diameter and is well thermalized by a graphite wall at the thermal column of the TRIGA reactor. The detector selection is

Upgrading

determined by beam intensity and the intended applications. The following items have to be taken into account:

- High detection efficiency, low background noise, as well as high signal-to-noise ratio;
- Good linearity and reproducibility for tomographic investigations;
- High dynamic range to achieve sufficient image gradation and sensitivity;
- High spatial resolution;
- The detectors should be commercially available at reasonable cost;

It is clear that; one detector alone cannot fulfill all these requirements. Previous studies by the ISNR (International Society for Neutron Radiology) community [Pleinert, 1997; Lehmann, 2004; Schillinger, 2006] have shown that scintillation detectors coupled to a slow-scan CCD system represent the best choice for tomography due to superior linearity, reproducibility, and weak gamma sensitivity. Integrating image intensifiers are preferably utilized for fast and periodic processes which are, however, not typical applications for a low intensity beamline. Our first 400 μm scintillator plate did not provide sufficient spatial resolution therefore we installed a 100 μm thin-plate scintillator which is now commercially available at a reasonable price [Tritec].

Our second detector, the ND&M camera, is also commercially available [Felber, GBR] . It is a scintillation detector coupled to a micro-channel plate with 50 μm resolution, high efficiency and extremely low intrinsic noise. The ND&M camera was originally used for beam alignment and tomography with monochromatic neutron beams at the ILL in Grenoble [Dubus, 2002; Dubus, 2005]. Its application in neutron imaging is restricted to weak beams with small cross section.

The third detector is intended to replace our Gd converter films. Neutron imaging plates (NIP) with a nominal scanning resolution of 25 μm have been chosen. With this ensemble of digitized detectors routine operation has recently been started with the upgraded instrument Figure 4-1.

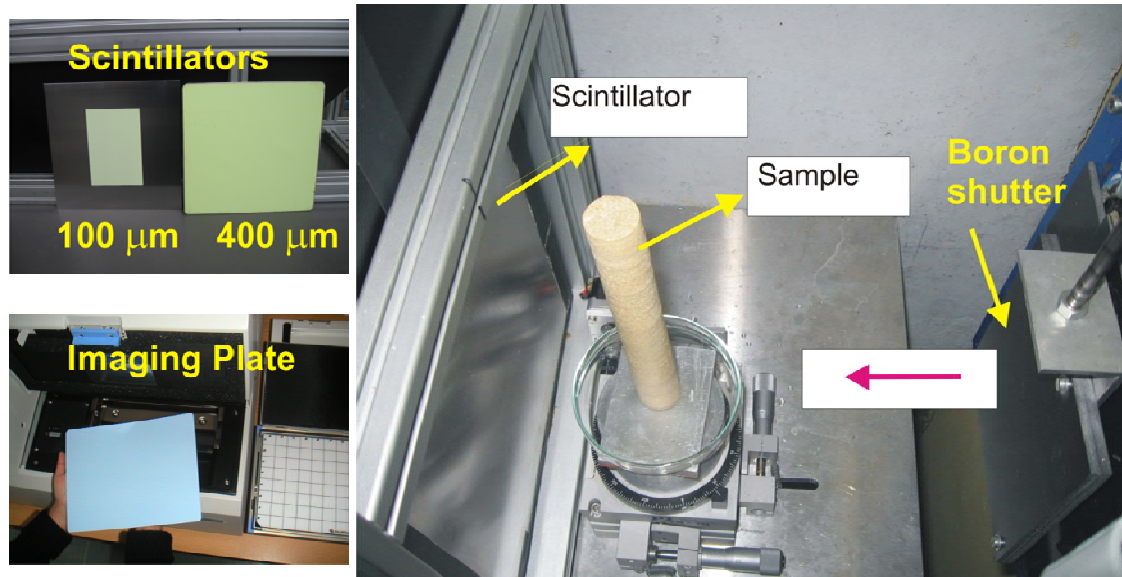


Figure 4-1:Left: The 100 μm thin-plate scintillator with 10 x 15 cm² detection area together with the old 400 μm scintillator; the 25 x 20 cm² imaging plate inserting in the BAS-5000 scanner. Right: Sample area of the upgraded instrument.

4.2 Characterization of the detectors

All three detectors are suitable for high resolution imaging beyond the resolution of 340 μm with the old scintillator [Koerner, 2001]. The spatial resolution is primarily limited by the collimation ratio $L/D = 130$, i.e., the ratio of the collimator length $L = 2600$ mm and the aperture $D = 20$ mm. To achieve best resolution it is necessary to minimize the sample-to-detector distance L_{S-D} and thereby the geometric unsharpness U_g :

$$U_g = L_{S-D} \left(\frac{D}{L} \right) \quad (4.1)$$

The second blurring effect is the intrinsic unsharpness in the sensitive layer. A thin layer narrows the spread of secondary radiation in the converter, thereby reducing the detector blurring at the cost of detection efficiency. To compare the spatial resolutions a sharp edge fabricated of a 25 μm thick gadolinium foil with 5.1 % neutron transmission was placed directly on the scintillator or the imaging plate. The measured edge spread function and its derivative, the line spread functions, can be approximated by a Lorentzian model if image blurring predominantly emerges in the converter. The ESF parameters $p_1 - p_3$ and λ are fitted to the measured edge profile with the resolution parameter λ as result:

Upgrading

$$\text{Edge spread function:} \quad ESF(x) = p_1 + p_2 \cdot \arctan(\lambda(x - p_3)) \quad (4.2a)$$

$$\text{Line spread function:} \quad LSF(x) = \frac{d}{dx} ESF(x) \quad (4.2b)$$

$$\text{Resolution:} \quad FWHM(x) \equiv \frac{2}{\lambda} \quad (4.2c)$$

In the following sections we compare the full-width-half-maximum (FWHM) resolutions, the absorption probabilities in the neutron sensitive layers, and the inhomogeneities in the beam profiles. Table 1 gives an overview of some key detector characteristics for NR / NT applications. The neutron-to-gamma ratio was determined by comparing the intensities with open and closed boron beam shutter. The intrinsic noise was measured several hours after reactor shut-down with beam and camera shutters closed.

Table 4-1: Detector characteristics

Detector	Sensitive area	Layer thickness	Spatial resolution	n / γ - ratio	Intrinsic noise / pixel
⁶ Li thin-plate	10 x 15 cm ²	100 μ m	150 μ m	500	300 + (0.4 /s)
Gd – NIP	20 x 25 cm ²	135 μ m	40 μ m	50	4 x 10 ⁻⁵ /s

4.2.1 Thin-plate scintillation detector

Scintillation plates in combination with a slow-scan CCD camera are commonly used in neutron tomography. They are integrating devices which accumulate the scintillation light without amplification over a period of several minutes. Their weak points are the limited spatial resolution, the density and the thickness variations in the layer which cause a nonuniform open beam image. ⁶Li is a good choice as neutron absorber because it offers the best gamma discrimination. In the ⁶LiF:ZnS scintillator screen the neutrons are converted to green light peaked at 520 nm:



The overall detection efficiency depends on the ${}^6\text{Li}$ -density, scintillator thickness, composition of the activators (ZnS, Ag), self-absorption of the generated photons in the scintillator, optical lens, and, finally, the photon detection efficiency in the CCD-camera [Eijk, 2001]. Experimentally, the neutron transmissions have been compared through the old 400 μm scintillator plate, $T = 68.7\%$ (absorption probability $\approx 31\%$), and the new 100 μm scintillator, $T = 86.8\%$ (absorption probability $\approx 13\%$). Thus, the detection efficiency of the 100 μm scintillator is lower by at least a factor of two, and the exposure time increases by that factor to achieve similar image gradation. The sensitive area of the 100 μm layer is $10 \times 15 \text{ cm}^2$, coated on a 1.5 mm thick plate of pure aluminum. From the data sheet provided by the company [Tritec] the relative light output is peaked at 100 μm . An alternatively available 50 μm scintillator would be inefficient for weak beam intensities.

The spatial resolution predicted by the manufacturer is 170 μm for the 100 μm scintillator, and 340 μm for the 400 μm scintillator. With our standard lens, $f = 105 \text{ mm}$ (Nikkor f/1.8, Nikon), we are limited by the optical resolution of $200 \times 200 \mu\text{m}^2$ (CCD pixel size $24 \times 24 \mu\text{m}^2$). Therefore repeated the ESF measurement has been repeated with larger focal length ($f = 180 \text{ mm}$, f/2.8) and $80 \times 80 \mu\text{m}^2$ optical resolution Figure 4-2 right, a best resolution 150 μm for the 100 μm plate has been obtained, well in agreement with the manufacturer's specification.

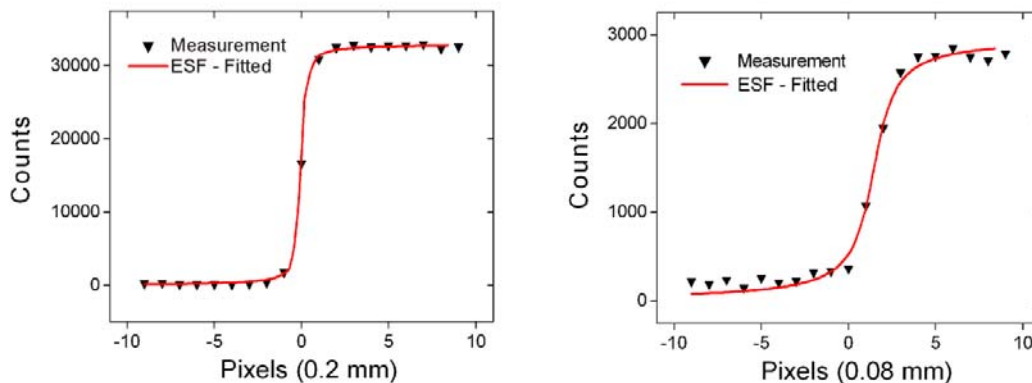


Figure 4-2: ESF measurements with different lenses. The pixel size denotes the optical resolution of the lenses, left $f = 105 \text{ mm}$, right $f = 180 \text{ mm}$. The fit yields $\lambda = 1.1(1)$ and $145 \pm 13 \mu\text{m}$ resolution in the right plot.

Figure 4-3 reveals different open beam inhomogeneities in the two ${}^6\text{Li}$ layers. As a measure for such intensity variations the standard deviation σ of the illuminated pixels are computed for the whole beam, and intensity profiles are plotted for the central region within the line markers. Given a uniform beam profile and ${}^6\text{Li}$ distribution, σ approaches the square root of the average pixel intensity ($\sigma \approx \sqrt{N_{average}}$). Obviously, this ideal limit is not reached, and therefore the resulting inhomogeneities have to be eliminated by pixel-wise open beam correction:

$$\text{Transmission} = (N_{\text{sample}} - N_{\text{background}}) / (N_{\text{open beam}} - N_{\text{background}}) \quad (4.4)$$

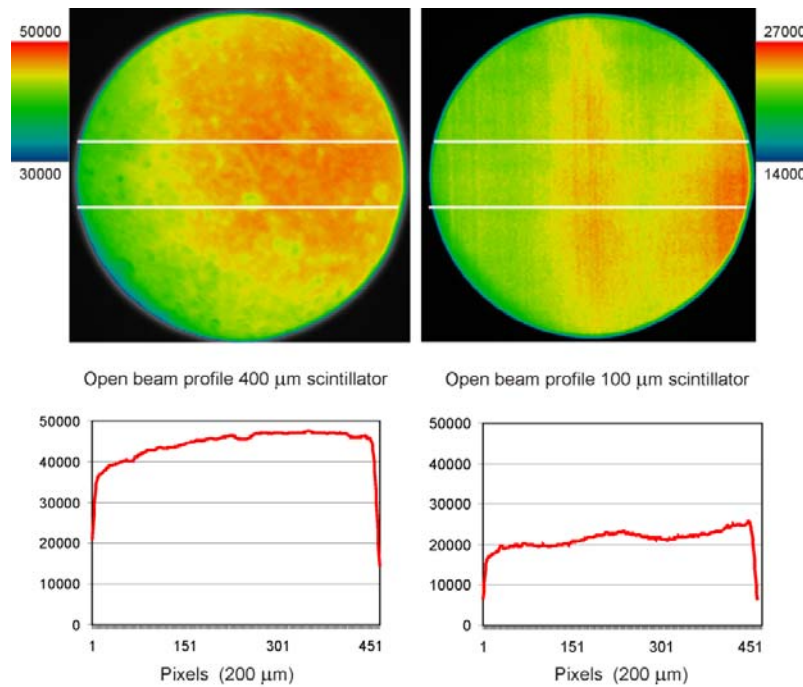


Figure 4-3: Inhomogeneities in the open beam profile.

Left: 400 μm scintillator, overall intensity variance $\sigma = 13 \times \sqrt{N_{average}}$, maximum intensity

difference in the area between the two marked lines $\frac{N_{\max} - N_{\min}}{N_{average}} = 17\%$.

Right: 100 μm scintillator, $\sigma = 11 \times \sqrt{N_{average}}$, maximum intensity difference 22 %.

Upgrading

The scintillator-CCD unit has several noise contributions: Gammas absorbed in the scintillator, white spots caused by bad (“hot”) pixels whose position remains unchanged, dark current and read-out noise. Surprisingly, a very little difference is seen in the dark images with the reactor on/off, only a few multipixel events occur due to gamma or neutron tracks. This shows that direct interactions of gammas and neutrons hitting the CCD chip are negligible at the detector site. The dark current is minimized by cooling the CCD chip down to -130°C with liquid nitrogen, it increases linearly with time if a constant readout offset is added Figure 4-4 left.

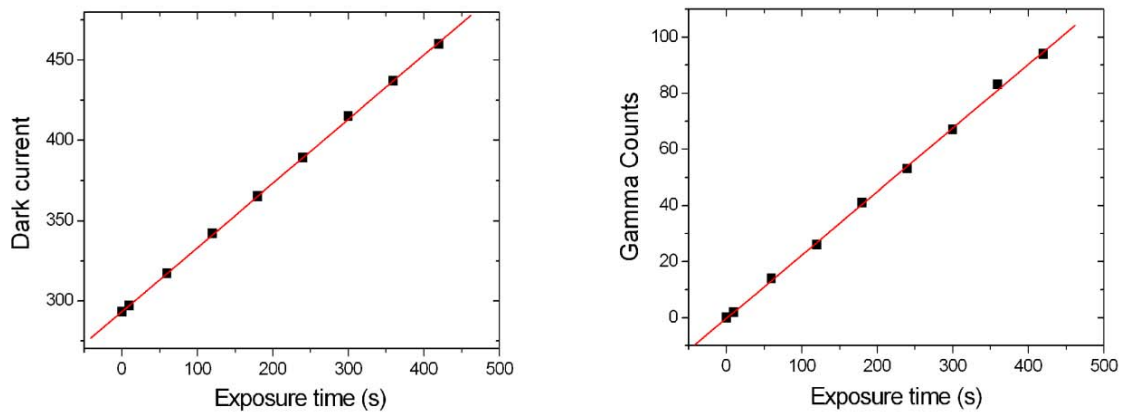


Figure 4-4: comparison of the dark noise (left, camera-shutter closed) and gamma noise (right, beam-shutter closed). The dominating dark noise increases with $N_{Dark} = 293 + 0.4 \times time(s)$ and the gamma background with $N_{Gamma} = 0.23 \times time(s)$.

The readout noise depends on the read out speed of the CCD chip, where the best signal-to-noise ratio is obtained at lowest speed. The gamma sensitivity was derived by comparing beam intensities with open and closed boron shutter which is transparent to gammas Figure 4-4 right. A neutron-to-gamma sensitivity of 500 and an overall signal-to-noise ratio of 100 have been obtained after the maximum exposure time of 7 min.

The reduction of remaining white spots is delicate because applying a simple median filter would reduce sharpness for the whole image. Selective removal of zingers is preferred by comparing every pixel value with the average count number of its neighbors and replacing it, if the ratio is greater than an adjustable threshold.

4.2.2 Imaging plate detector

Neutrons are absorbed in the Gd_2O_3 which is uniformly dispersed in the photostimulable phosphor (BaFBr:Eu) layer and an organic binder:



The BAS-5000 IP Reader [Fujifilm] enables the scan of BAS-ND 20 x 25 cm^2 neutron sensitive imaging plates and x-ray sensitive BAS-SR imaging plates with a nominal resolution of 25 x 25 μm^2 . The secondary particles excite the BaFBr:Eu to a metastable state, where electrons are trapped. The information is stored in locally trapped electron-hole pairs in the phosphor as latent image. This information is registered by optical stimulation with a focused HeNe laser. During the readout process in the scanner the trapped electrons are further excited by the red light from a He-Ne laser which causes a luminescence of blue light which is finally detected by a photomultiplier tube. Layer thickness (135 μm) and composition have been optimized in spatial resolution and photo stimulated luminescence (PSL) [Kobayashi, 1999]. After readout the NIP is erased with bright white light and can be reused many times as long as no mechanical damage occurs.

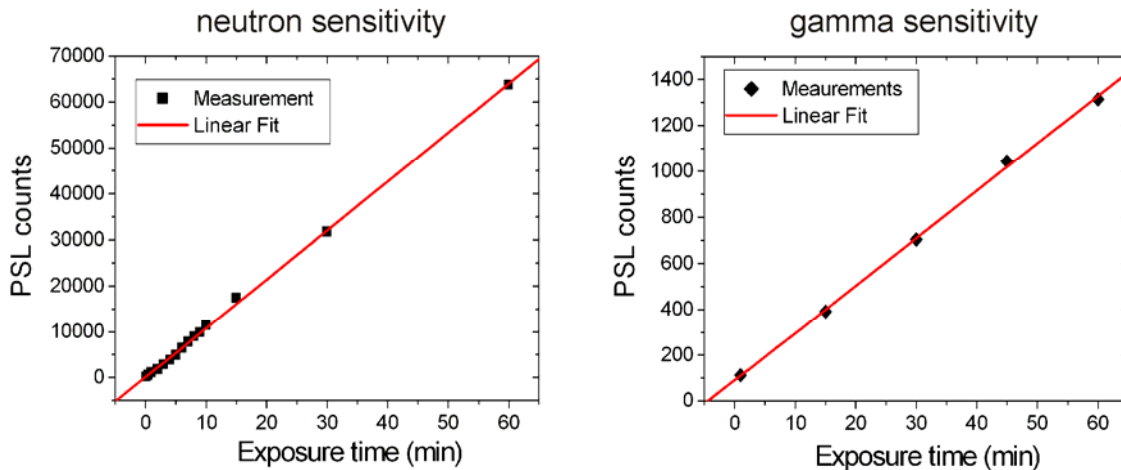


Figure 4-5 Linearity of the NIP count numbers at 25 μm pixel resolution.

Left: NIP in the open neutron beam, $PSL / pixel = 169 + 1064 \times time (min)$

Right: NIP with beam shutter closed, $PSL / pixel = 91 + 21 \times time (min)$

Advantages of the IP-detector are the wide linearity range, the absence of electronic noise, 16 bit dynamic range, and a high efficiency of 80 % in the layer [Kobayashi, 1999; Thoms, 1999]. However, the overall detection efficiency depends on the light collection optics of the scanner. A disadvantage of the NIP is its higher gamma sensitivity due to the heavy elements in the plate [Masalovich, 2002]. As scanning parameters with best signal-to-noise ratio at 25 μm resolution the highest gradation (16 bit) and sensitivity S4000 at level L5 have been chosen. The scanned images are stored as Fuji-img file format and then further processed with Image-Pro Plus 6 (MediaCybernetics); the logarithm of the detected PSL signals is converted to unsigned 16 bit data yielding a maximum image size of 160 Mb.

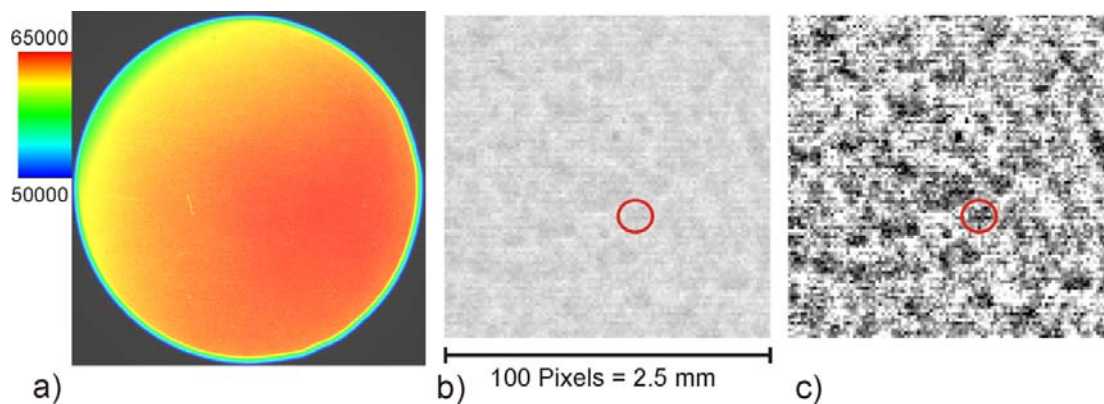


Figure 4-6 Open beam intensity variations and NIP artifacts.

- A) Intensity variance in the open beam $\sigma = 12 \times \sqrt{N_{average}}$, maximum intensity variation 17 %.
- B) Random pattern of dark spots (150-200 μm) with reduced PSL intensity (unprocessed).
- C) Same artifacts contrast enhanced.

After erasing the IP the intrinsic noise is only 0.3 counts per 25 x 25 μm^2 . The intrinsic noise increases from 0.3 to 11 per pixel after three days deposition in a light-tight box outside the reactor building. A neutron-to-gamma ratio of 50 was derived. The NIP linearity was confirmed for an interval between 1 and 60 min exposure time Figure 4-5.

The open beam image confirms, except for a few scratches in the layer, a uniform Gd-distribution Figure 4-6. Unfortunately, a microscopic pattern of dark spots, 150 – 200 μm in size, appears in the images yielding 25 % reduced PSL intensity. A similar pattern was found

when scanning the NIP with 50 μm and 100 μm resolution, and also in the x-ray sensitive SR imaging plate. Such micro-structural artifacts enhance the intensity variance in detector pixels and impede the investigation of inhomogeneities in materials. The usual open beam correction (Eq. (4.4)) is not applicable until the problem of 25 μm positioning accuracy is solved.

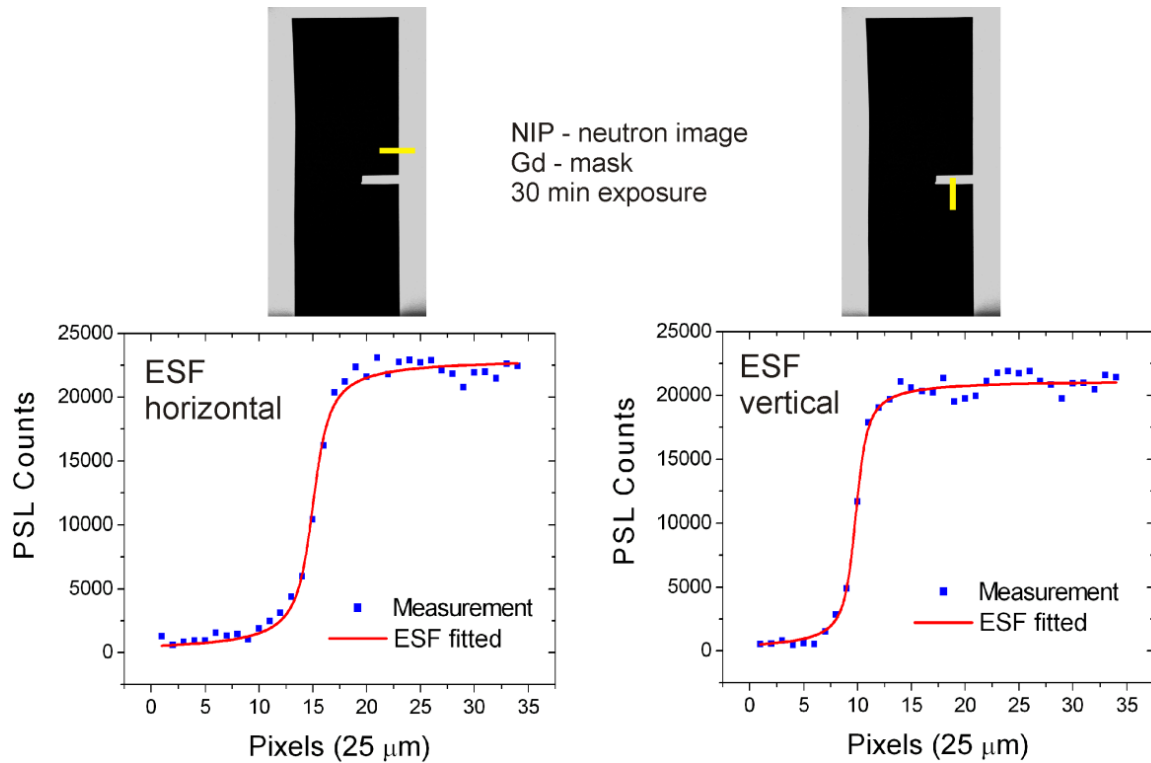


Figure 4-7: ESF - resolutions with the NIP; the ticks in the neutron images mark the positions of the edge profiles. The fits yield $\lambda = 0.8(2) \Rightarrow 60 \pm 15 \mu\text{m}$ horizontal, and $\lambda = 1.25(20) \Rightarrow 40 \pm 7 \mu\text{m}$ vertical resolution.

In Figure 4-6 we also recognize disturbing horizontal line structures from the scanning process which can be removed by a low-pass filter. The measured transmission through the 135 μm photostimulable layer plus the 370 μm polymer support is 19 %, which indicates a high detection efficiency of about 80 % in the NIP. The Gd-edge directly attached onto the NIP yields 60 μm resolution horizontally and 40 μm vertically Figure 4-7.

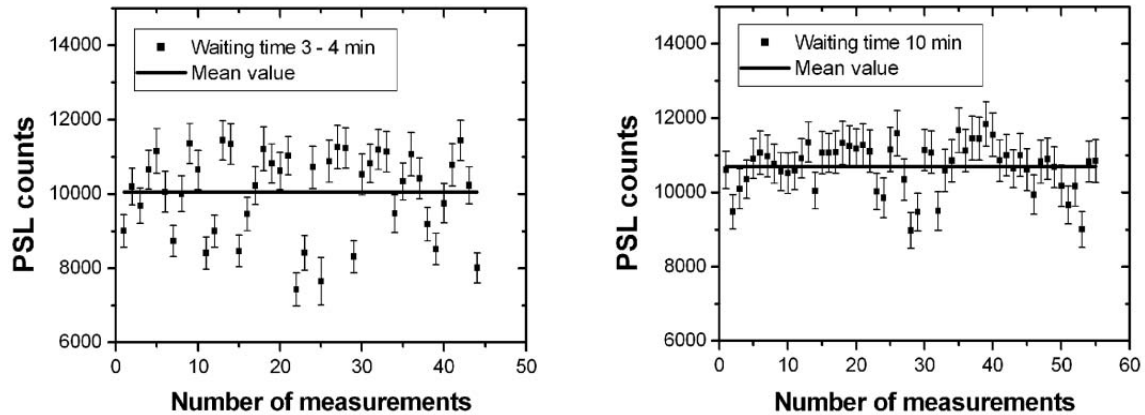


Figure 4-8: Reproducibility of NIP intensities by repeating always the identical measurement procedure: 10 min exposure → waiting time → scanning → 30 min erasing time.

Left: 3 – 4 minutes waiting interval, Mean = 10050 ± 1150

Right: 10 minutes waiting interval, Mean = 10700 ± 655

For the first batch of NIP measurements, the reproducibility of open beam intensities, repeated under identical experimental conditions and read-out parameters, was disappointing. The PSL counts at 10 min exposure varied between 7000 and 11000, far beyond the 3 % power fluctuations. Our supplier recommended a waiting time of at least 5 min before scanning in order to stabilize the latent image. We have chosen a 10 min waiting interval for all subsequent NIP scans and the reproducibility has improved Figure 4-8.

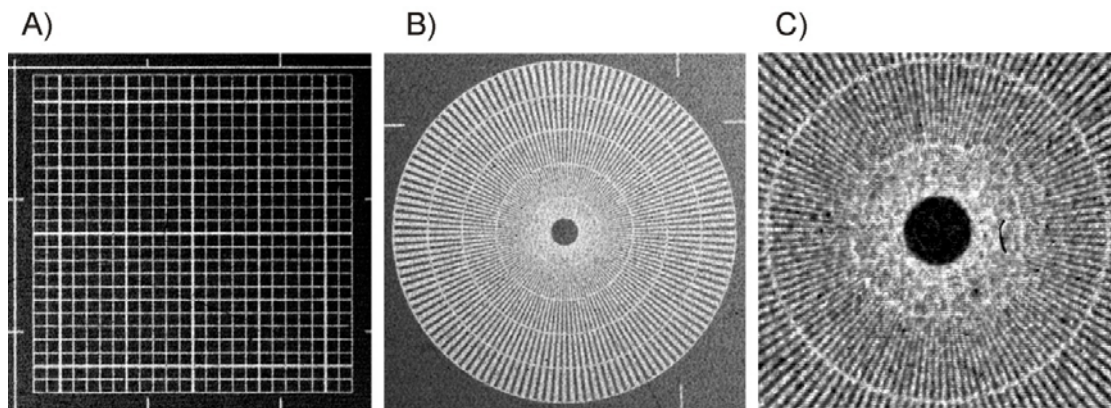


Figure 4-9: Imaging of the PSI Gd test mask with the NIP. A) The fine grid lines with 50 μm line width are clearly visible in the square. B) Siemens star with radial markers at 500, 400, 300, 200, 100, 50 μm line pair resolution. C) The visibility of the periodic spokes becomes blurred between 100 and 50 μm resolution.

Upgrading

Finally, the Gd-edge resolution has been compared with a recently developed gadolinium test mask consisting of a Siemens star, with spoke periods from 500 to 40 μm , and a square grid with line widths of 150, 100 and 50 μm . The 50 μm grid lines are easily resolved in Figure 4-9a, whereas the resolution of periodic spoke structures lies between the two innermost concentric radial markers of 100 and 50 μm . Here again the intrinsic granularity affects the detection of line pairs and periodic structures Figure 4-9 b,c.



Figure 4-10: Nitrogen filling for cooling the CCD camera.

Previously the CCD camera could only be filled once for a tomography measurement and the cooling lasted for a maximum time of 3 to 4 hours. This was a limitation. In order to exploit the full dynamic range, an arrangement has been made for a fixed nitrogen filling of the CCD camera. With the help of this arrangement, liquid nitrogen can be filled during measurement. Thus it is now possible to increase the exposure time and the total number of projections to get tomography measurements with good resolution and higher sensitivity. Promising applications of improved resolution and sensitivity have been presented in [Zawisky].

4.3 . Summary

Each of our detectors has specific advantages and preferential application fields. The 100 μm scintillator will preferably be used for tomography and NR time series, e.g., the penetration of water and consolidation agents in stones and building materials. Its strengths are reproducibility, position stability and low gamma sensitivity.

The imaging plate is devoted to high resolution imaging of hydrogen and absorber distributions in thin materials, textile fibers and museum objects. It offers the highest resolution, detection efficiency and image gradation among the three detectors.

It is shown in the following chapters that high spatial resolution down to the 50 μm regime is practicable with weak intensities of approximately $10^5 \text{ n/cm}^2\text{s}$. With the new detectors the limits of spatial resolution and image gradation at this beamline have been reached; a further enhancement of optical resolution would entail unrealistic exposure times and degrade the signal-to-noise ratio. Considering the constraints imposed by the collimation ratio and scattering artifacts, a 50 μm resolution can only be exploited with thin and weakly scattering samples mounted directly on the detection plate.

Specific features and preferential application fields of our upgraded digitized detectors are summarized in table 1. The 100 μm scintillation plate offers high position and intensity reproducibility which allows either sequential imaging in dynamic neutron radiography and tomography, or to increase statistical accuracy and sensitivity by repeated measurements. The spatial resolution cannot compete with imaging plates but in many cases, e.g. thick and

Upgrading

scattering samples, this disadvantage is of no practical consequence. Imaging plates offer best resolution and higher efficiency but our setup does not allow repetitive imaging. Granular artifacts in the plates are very disturbing in the inspection of material inhomogeneities.

Table 4-2: Detector performance and preferred application fields at our beam line

	Thin plate scintillators	Imaging Plates	ND&M
Plus	Reproducibility; Low gamma sensitivity;	High efficiency; High resolution; Homogeneous profile;	Good efficiency; Reproducibility; High resolution; Homogeneous profile; Efficient noise suppression;
Minus	Lower efficiency; Inhomogeneous beam profile; Medium resolution;	Poor position reproducibility; Micro-artifacts; Mechanical abrasion; Higher sensitivity to gammas and scattered radiation;	Long measurement times; Small detection area;
Applications	NT + sequential NR: Hydrogen distribution in materials; Penetration and diffusion of different consolidants in chemical restoration; Pore, grain, defect analysis in geology; Boron and rare earth analysis in steels and rocks;	High resolution NR: Sensitive hydrogen and absorber analysis in thin materials; Hydrogen in textile fibers; Investigation of museum objects;	High resolution + sequential NR: Absorber and defect analysis in engineering and geology; Imaging at reduced reactor power down to 20 kW or with monochromatic beams;

Upgrading

Useful high-resolution applications within the framework of our projects are the detection of non-uniformities of neutron absorbing elements and isotopes in engineering, grain, porosity and defect analysis in geology, penetration of moisture and consolidation agents in building materials, hydrogen distribution in textile fibers, and high quality investigation of museum objects down to 50 μm resolution. Due to the low beam intensity sample activation is negligible at our instrument in most applications.

We have quoted improvements in tomography, e.g., better grain resolution in feldspar and a more accurate 3D analysis of consolidation agents in lime-sandstones. Finally, we presented full dynamic range images of hydrogen distributions in thin samples which allow a very sensitive analysis of liquids in small sample regions. All these applications have been discussed in detail in the coming chapters. An application of the upgraded instrument was the continuation of steel inspection. The enhanced neutron transmission in thick boron alloyed steels has been confirmed with the new scintillator plate and the imaging plate detector as well. So far no boron inhomogeneities have been detected which could explain the enhanced neutron transmission.

Applications

Applications

5 ST. STEPHANS CATHEDRAL PROJECT

5.1 INTRODUCTION

St. Stephans Cathedral in the heart of Vienna has a volume of 20,000 m³, composed of different calcarenites (calcareous-sandstones), with an overall height of 137 m. The Cathedral has a long history, which started in the 12th century. It was nearly destroyed several times by war and fire, but was rebuilt each time to an increasingly larger cathedral. The corrosion due to wind, moisture, frost, acid rain, plant growth, bird excrements, etc., requires continuous restoration of its facade. The penetration of moisture into the highly porous stone texture creates a permanent mechanical stress on the weather exposed surfaces, e.g., conversion of calcite into gypsum and recurring freezing processes cause deep surface cracks and mechanical damages of the facade.

Nowadays, a widely employed, but still disputed technique is the extensive use of stone consolidants and impregnation products to make the surface more corrosion resistant. This procedure is costly and can be even counterproductive if moisture penetrates regions behind the strengthened layers. In addition, restoration agents can cause discoloration and yellowing of the original substance. A traditional alternative restoration technique is the exchange of damaged stones by new but untreated stones of similar composition. The Cathedral's stonemasons' lodge, has been the base for the preservation of the cathedral since the middle ages [<http://www.stephansdom.at/data/restaurierung/index.php>]. Their main effort deals with the restoration and preservation of the building and is financed with a yearly cathedral budget and donations from the public. Recently, we started cooperation with the stonemasons' lodge because neutron radiography (NR) and neutron tomography (NT) have been confirmed to be very useful for the non-destructive investigation of conservation agents [Nemec, 1999], moisture penetration [Pleinert, 1998; Gibbons, 1999; Abd, 2002; Hanzic, 2002; Lehmann, 2004], rocks and geological materials [Winkler, 2002; de Beer, 2004]. In this chapter first results of this cooperation are presented.

5.2 Restoration procedure and sample preparation

The main goal of our project is the investigation of the penetration and distribution of the stone consolidant (strengthener) because a deep and homogeneous penetration is essential

in every restoration procedure. We also want to investigate the long durability of the restoration and protection agents by comparing freshly processed stones with older stones which have been restored several years ago. All our samples have been prepared with consolidants derived from silicic acid ethyl ester, i.e. ethyl silicates [WACKER OH 100]. They are low-molecular agents with high penetration ability, the binder formed in the stones is of mineral nature, and it resembles the building material and is acid-resistant. When applied, the product gets absorbed via the capillaries and reacts with the atmospheric humidity or capillary water to form silicic acid gel ($\text{SiO}_2 \cdot x\text{H}_2\text{O}$), an amorphous solid substance. During the drying process ethanol removes some water from the hydrogel and evaporates together with water. Most of the strengthener is converted into the final gel after weeks under standard climatic conditions, when the final strength is reached.

The penetration ability of the consolidant crucially depends on the pre-treatment of the surface, e.g. dirty crusted surface layers must be cleaned to make the area dry and absorbent. Large areas typically are sprayed with the agent while smaller samples can be immersed in a bath. The spraying procedure has to be repeated several times to achieve the desired penetration. After the treatment the surface remains hydrophobic for a period of 1-2 months, but this effect then disappears. Therefore the restoration must be finished by water proofing, which in our project is realized by a polysiloxan impregnation agent which forms a thin hydrophobic macromolecular film of silicone resin polymer on the pore walls. The protective layers shield the surface against water penetration but maintain the necessary vapor permeability of the building materials. For our preliminary studies we obtained a few samples from the original substance of the facade, i.e. boreholes of 2.5 cm diameter drilled out at different locations. In addition several sets of freshly quarried calcareous arenites were prepared with similar composition, but untreated and not weather-exposed. On these reference samples we applied the restoration products under laboratory conditions, to study systematically the potentials of NR and NT.

5.3 Neutron studies on freshly prepared lime-sandstones

We began our studies with newly-drilled cores from different deposits in the Viennese basin, in St. Margarethen and Mannersdorf, covered by sea 16 million years ago. The Götzendorf sandstone was formed 5 – 8 million ago in the coastal region of a freshwater lake. These deposits are main resources for the Cathedral's building material [Müller, 1993]. The

calcarenites are classified by their deposit and several properties, e.g., hardness, porosity, grain size distribution, permeability, color. Stones with very different properties can be found in one deposit, which makes a systematic investigation very time-consuming. But the neutron transmission analysis is greatly simplified in calcareous sandstones because they are composed of weak-absorbing nuclei, e.g., quartz (SiO_2), calcite (CaCO_3), gypsum ($\text{CaSO}_4 \cdot 2\text{H}_2\text{O}$), and spurious elements like iron. Therefore the neutron attenuation is dominated by the hydrogen content. In case of small absorption and scattering the neutron attenuation can be approximated by the exponential transmission law:

$$T \cong e^{-\Sigma t} \quad (5.1)$$

Σ denotes the total macroscopic neutron cross section, and t the path length through the sample. The cross sections are tabulated for thermal wavelength ($\lambda_{th} = 0.18 \text{ nm}$) and must be converted to the experimental mean neutron wavelength $\bar{\lambda}$. The total cross section can also be expressed as the sum of all isotopic densities ρ_i :

$$\Sigma = \frac{N_A \bar{\lambda}}{\lambda_{th}} \sum_i \frac{\sigma_{th,i}}{A_i} \rho_i \quad (5.2)$$

The microscopic cross sections $\sigma_{th,i}$ and atomic weights A_i are tabulated for most isotopes; N_A represents the Avogadro number. The neutron transmission directly relates to the densities in the sample. By transmission tomography the complete volume distribution $\Sigma(x, y, z)$ can be visualized, which allows to distinguish volume effects from surface effects. A complete 3D analysis of strongly attenuating elements like hydrogen and boron is possible if some information about the sample composition is available [Zawisky, 2004]. The typical measurement time for a tomographic scan is three hours at the Atomic Institute where a well-moderated thermal neutron beam ($\bar{\lambda} = \lambda_{th}$) is available. The typical exposure time for one radiography image is 40s using a ^6Li -scintillation converter and a digital camera. The fast uptake of water and restoration agents can be detected by time-series of radiography images in one minute intervals.

St. Stephans Project

Table 5-1. Dominating microscopic thermal neutron cross sections (σ_{th}) in calcareous sandstones. The macroscopic cross sections (Σ_{th}) strongly depend on the physical properties (density, porosity, fossil)

<i>Element</i>	$\sigma_{th} (10^{-24} \text{ cm}^2)$	<i>Mineral</i>	$\Sigma_{th} (\text{cm}^{-1})$
H	82.35 bounded 38 unbounded	Water	5.6 bounded 3.7 unbounded
O	4.23		
C	5.56	Quartz	0.25
Ca	3.26	Limestone	0.34
Si	2.34	Quartz sandstone	1.5
S	1.56	Gypsum	2.0
Fe	14.18		

Our first observation was a variation in the migration rate of the consolidant which differs for every sample. Figure 5-1 shows two typical NR measurements, sample 1A is a hard St. Margarethen stone with low migration speed, and sample 1B, a soft and fine-porous stone from the same deposit but with faster migration and deeper penetration of the strengthener.

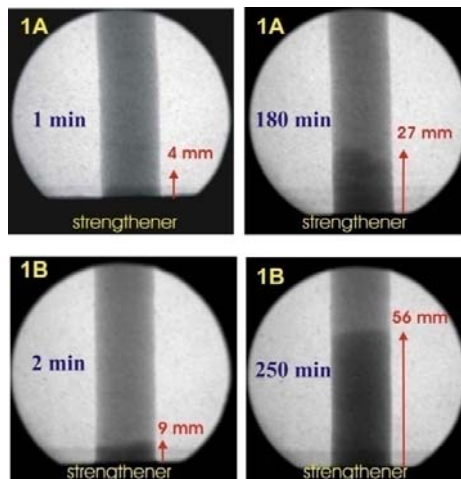


Figure 5-1. Neutron attenuation in two St. Margarethen during strengthening: 1A: hard, 1B: soft [Hameed, 2006].

Figure 5-2 shows the different migration behavior of water, strengthener, and impregnation agent, in a soft stone from Mannersdorf. The diffusion of water is always faster than of the consolidant. The migration of the consolidant is finally limited by solidification after a few days.

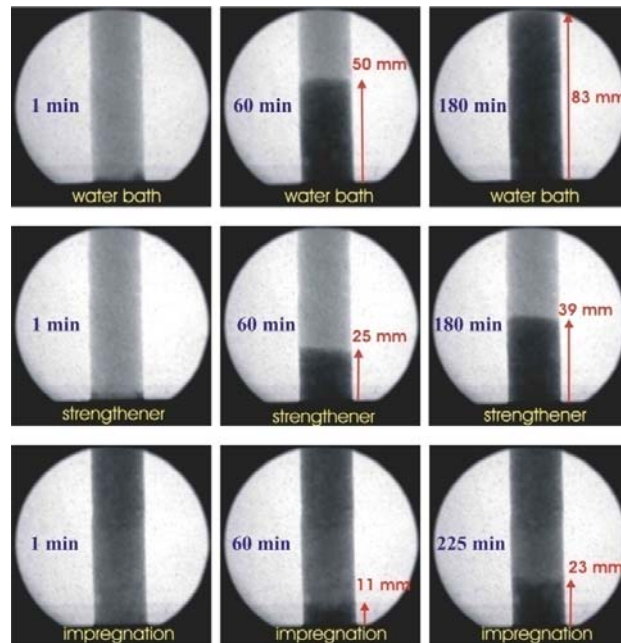


Figure 5-2. Freshly drilled cores from one block of soft Mannersdorf calcarenite. The stones were processed in a soaking bath of approx. 7 mm depth. Irrigation and consolidation were applied on the untreated dry stones. The water-repellent treatment was applied subsequent to the consolidation [Hameed, 2006].

Finally, we have confirmed that the consolidated and impregnated stones are water-resistant by soaking them again in a water bath and analyzing the transmission profiles at different times. These preliminary measurements have demonstrated that the solvent and gel formed by the strengthener cause strong neutron attenuation, which is easily detectable by NR technique. Experimentally, it is convenient to immerse the samples in a bath and follow in situ the migration of the consolidant by time-resolved neutron imaging. Such investigations could be useful for a comparison of different products used in the restoration of Vienna's sculptures and ancient buildings.

Our partners are particularly interested in investigations under realistic conditions, when the samples are prepared under similar conditions as in large-scale restoration, where

the spraying technique is widely used. For this purpose a new series of St. Margarethen stones was prepared to study the neutron sensitivity after spraying the consolidant over a larger surface. After twofold spraying of the strengthener and air-drying three samples were cut from one block and investigated with NR and NT methods without further processing. As the solvent partly evaporates the neutron attenuation decreases over a period of one month after the treatment. The tomographic reconstructions yield a clear picture of the penetration of the sprayed consolidant, which typically lies between 20 and 30 mm (Fig. 3), thus, the high neutron sensitivity was successfully confirmed also under realistic conditions.

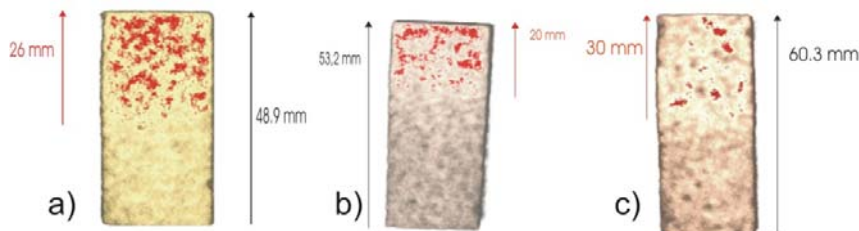


Figure 5-3. Tomographic images of three freshly cut and consolidated St. Margarethen limestones [Hameed, 2006]:

a) 4 days, b) 9 days, c) 11 days after spraying; red and bright regions show the strengthener.

5.4 NR and NT investigations of samples from St. Stephan's facade

The drilling of high-located, aged, and weather-exposed cores from the facade of the Cathedral is expensive, therefore samples can only be provided during ongoing restoration work. So far only five cores have been drilled out of the facade for our project Figure 5-4. The characterization and preparation history of the stones is summarized in Table 5-2.

Table 5-2: Characterization of the samples from St. Stephans facade

<i>Sample</i>	<i>Classification</i>	<i>Restoration procedure</i>
F1	Cylinder Ø = 2.5 cm Götzendorf, less porous, medium-grained siliceous-sandstone, rich in quartz	Spraying several layers strengthener Impregnation with water-repellent product Restoration period 1997 – 2004

St. Stephans Project

	Date: 1320 Location: Albertinischer Chor	Strongly weather-exposed, heavy winds
F2	Cylinder Ø = 2.5 cm Leithakalk Mannersdorf, highly porous, coarse-grained calcareous-sandstone Date: 1400 Location: Southern Tower eastside	Spraying several layers strengthener Impregnation with water-repellent product Restoration finished 2002 Less weather-exposed, not in main wind direction
F3	Cylinder Ø = 2.5 cm St. Margarethen highly porous, fine-coarse grained calcareous-sandstone Date: 1901 - 1903 Location: Southern Heiden-Tower	Spraying several layers strengthener Impregnation with water-repellent product Restoration period 1993 – 1995 Weather-exposed, windy conditions, not in main wind direction
F4	Profile 2.5 x 2.5 cm ² St. Margarethen calcareous-sandstone Date: 1860 – 1880 Location; High-Tower 70 m	Untreated Less weather-exposed

Surprisingly, the consolidant was not detectable in the outer regions of the cores Figure 5-6. In deeper regions the neutron attenuation was increased, either by higher density of calcium carbonate, or by higher hydrogen content that could be related to the consolidating gel or to linseed oil. Another explanation of the higher neutron attenuation could be iron hydroxide as natural deposit, because such a deep penetration of the sprayed consolidant is unlikely, and does not coincidence with our previous measurements. In addition, we recognize in the surface region at approx. 0 – 6 mm a crust of dirt, patina (iron hydroxide), gypsum, and in F3 probably also some silica gel as residues of the intervention. But neutron attenuation alone is not able to distinguish between the different impurities, deposits, and conservation products.

St. Stephans Project

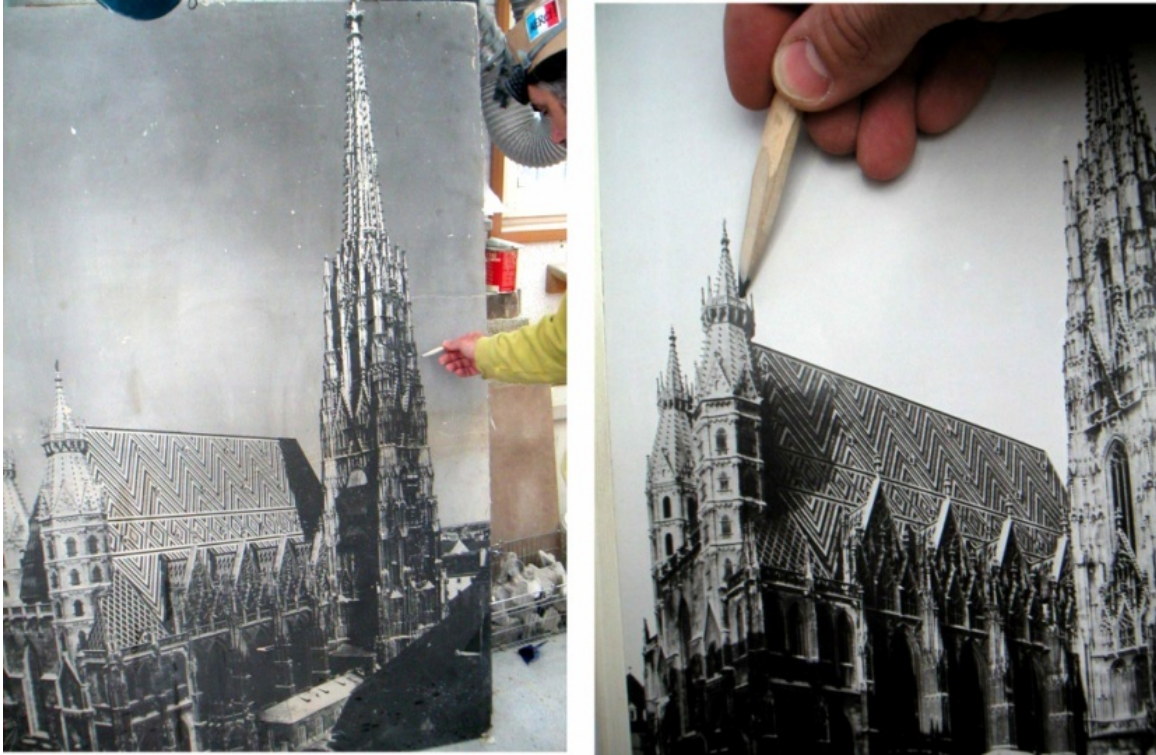


Figure 5-4: Sample F2 (left) was drilled from the weather-exposed Southern Tower, eastside. F3 (right) from the weather-exposed southern Heiden-Tower. These areas have been treated with different restoration techniques several years ago [Hameed, 2006].



Figure 5-5. Three cores drilled out from St. Stephen's facade. The diameter is approx. 25 mm and the arrows mark the weather-exposed outer surface [Hameed, 2006].

To verify whether the samples are still water-resistant several years after restoration and erosion, we performed a wetting from the outer surface in a soaking bath and recorded a time sequence of radiography images. The fast and deep penetration of the water in samples F1 and F2 confirmed our suspicion that the conservation products are no more effective Figure 5-7. Only F3 turned out to be water-resistant at the weather-exposed surface. But sample F3 reveals a similar pattern of neutron attenuation than F2; therefore an alternative detection method is required to get a clearer picture of the existence and distribution of the products.

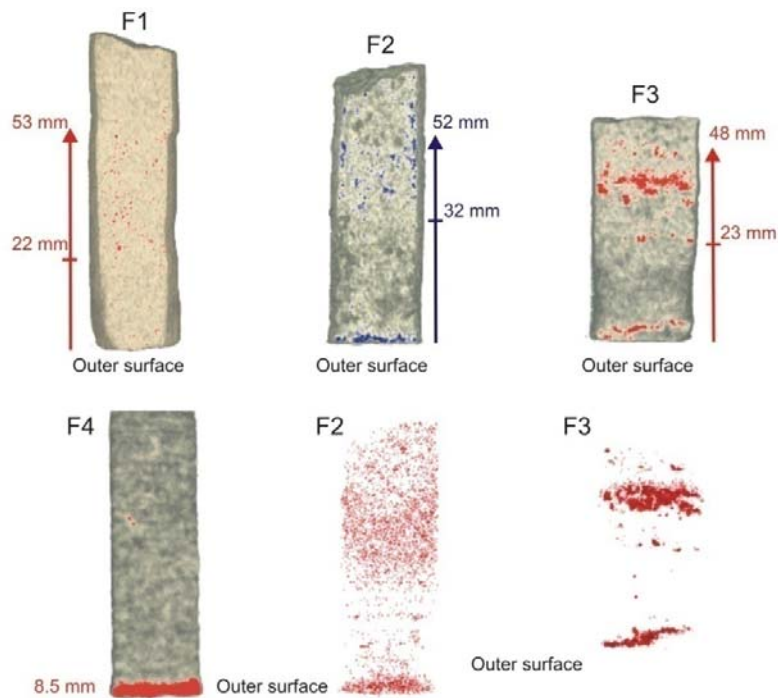


Figure 5-6. Tomography of three cores from weather-exposed areas of the Cathedral's facade, several years after restoration. Surprisingly, the consolidant was not visible at the outer regions. In the colored regions the neutron attenuation is increased by higher density and/or higher content of hydrogen and iron. In the bottom row the voxels of higher density and/or hydrogen content are extracted from the bulk in order to get a 3D impression of these regions of interest. In the untreated core F4 a surface crust is revealed at the weather-exposed surface (red layer) [Hameed, 2006].

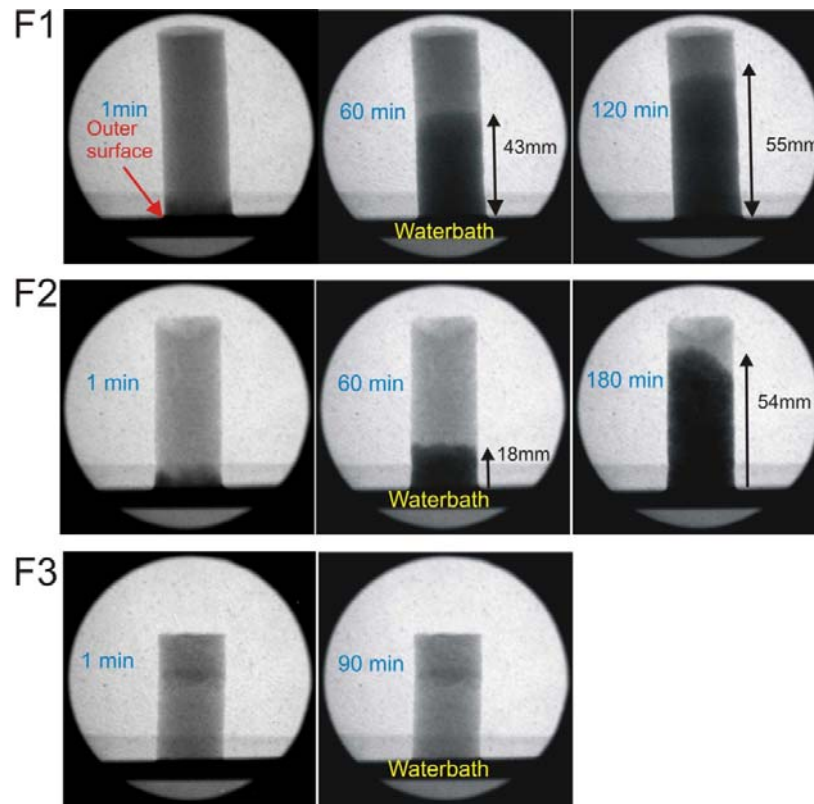


Figure 5-7. Testing the water-resistance of treated stones from the Cathedral's facade. Only in F3 moisture uptake was prevented effectively, while in F1, F2 the water-uptake was rather fast [Hameed, 2006].

5.5 Alternative inspection methods

A one-dimensional density profile can be obtained with ultrasonic detection. Two transducers were employed to determine the acoustic velocity along the sample height with a vertical resolution of 5 mm. The primary signal of acoustic measurements is the runtime of acoustic waves, which is delayed by circumventions in the presence of porosities because the waves preferably propagate through denser regions. Large velocities mark dense homogeneous regions, while increased porosity causes longer response times and marks regions of lower density.

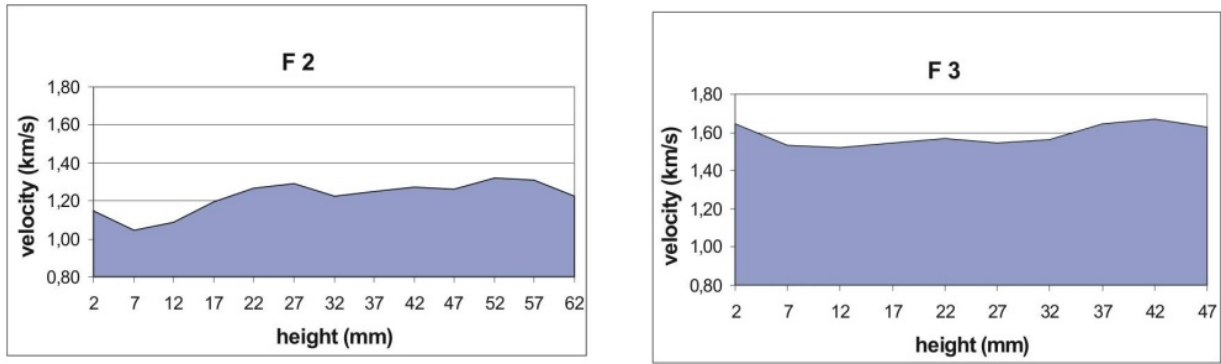


Figure 5-8 Acoustic measurements along the vertical sample axis. Higher velocities mark regions of higher density.

The acoustic measurements show reduced densities in the outermost 7 - 30 mm in all samples, followed by a region of higher densities, well in accordance with our tomographic results. We also recognize a compaction at the surface, approx. 7 mm deep, which was also revealed by neutron attenuation. The acoustic results therefore confirm, despite their poor spatial resolution, our tomographic measurements, but they cannot provide direct evidence for the penetration of the consolidant.

Further on, the permeability of samples was determined. The permeability is a characteristic measure for the frictional resistance of a fluid in the material. It depends on the viscosity of the liquid, and on material properties like composition, porosity, and capillary diameter. The permeability $k_f = k / \Delta p$ is the amount of water transmitted through a well defined area per time unit at pressure gradient Δp . We assume the same pressure gradients in all samples and calculate only the modified permeability k , defined as the amount of water flowing through an area of 1 m² per hour Table 5-3.

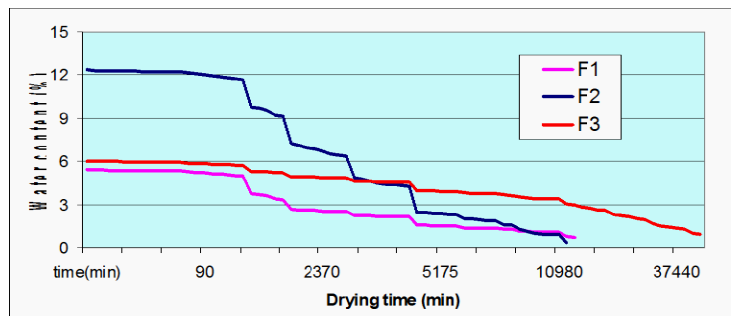


Figure 5-9 Left: Permeability measurement. The stones are hermetically sealed in vessels completely filled with water. Then the evaporation through the outer surface was measured over a time

period of 21 hours. Right: Measurement of drying rates of the wet stones in same configuration but empty vessels.

Table 5-3: Determination of the modified permeability k and the drying behavior

<i>Sample</i>	<i>Permeability (kg / hr·m²)</i>	<i>Drying time</i>
F1	0,302	280 h
F2	0,392	254 h
F3	0,243	785 h

Another test for the water-saturated samples was the examination of the drying rates at room temperature. We used the same setup as for the permeability measurements but without water in the vessels. Therefore it is guaranteed that the drying can only take place through the outer surface. Samples F1 and F2 reveal a typical drying curve as expected for the Götzensdorf and Mannersdorf calcarenites. The drying of F3 is strongly delayed by a surface compaction as confirmed with neutrons.

The following techniques are destructive because they require cutting and polishing of thin slices or grains. Another disadvantage of these methods is that they provide only local information which makes global conclusions about the distribution of the consolidant problematic. From F1-F3, thin-sections of approx. 30 µm thicknesses were prepared, suitable for further optical investigations. Figure 5-10 shows scanning images using a photo scanner, original scan resolution 4800 dpi, compressed to 600 dpi for presentation. These images are to be compared with the tomographic reconstructions in Figure 5-6. The regions of higher neutron attenuation are partly revealed in the thin-sections as zones of higher density and lower porosity, also the surface crust is visible.

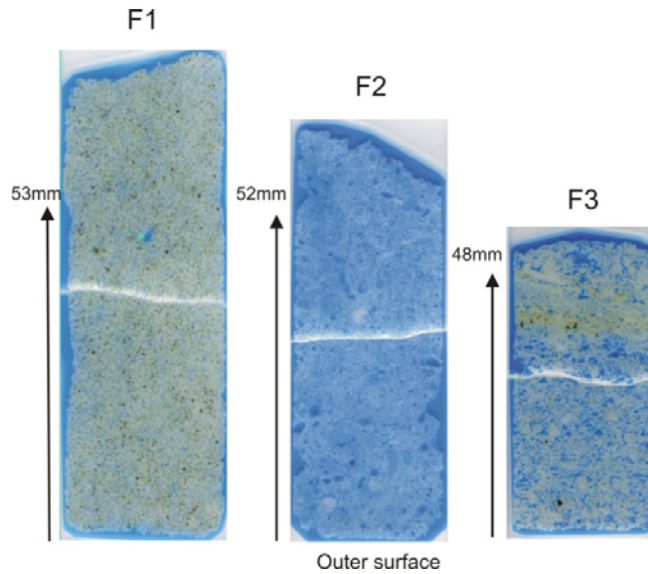


Figure 5-10 Optical scans of thin-sections. The surface crust and zones of higher density are clearly visible in F3, and partly also in F2. F1 shows a rather homogeneous and dense profile. In F1 and F3 we recognize grains of iron hydroxide (brown dots). The slices have been cut in two pieces (white dividing line) for polishing; the blue areas show the colored resin carrier.

Finally scanning electron microscopy (SEM) combined with energy-dispersive x-ray analysis (EDX, Philips XL30 ESEM) was performed for an accurate chemical analysis in some small selected areas. In order to discriminate the consolidant we focused on the silicon distribution at specific regions on the thin-sections. In addition to this, SEM studies were also performed on uneven sample planes. The SEM procedure with thin-sections, which were previously coated with carbon in order to achieve electrical conductivity, was the following: Using the back-scattered detector (BSE), we first scanned the surface at low resolution at a viewing field of approx. 500 x 500 μm . At pores and grain contact areas we increased the magnification up to 2 μm x 2 μm and searched for gel structures and fine gel filaments. In such areas of interest a chemical analysis was then performed using x-ray diffraction. The alternative procedure of examining uneven planes obtained by simply breaking the samples and sputtering the surfaces with gold used the secondary electron detector (SE) and focused on morphological features at magnifications up to 1,000 times. This procedure certainly demands an experienced expert and yields only a small sampling from the slice. The silicon analysis of F1 is complicated by the high content of quartz grains, only sporadic evidence of silica gel was found near the surface, up to a depth of 5-6 mm. In F2 again, only sporadic evidence of silica gel fixed on grain contact areas near the surface that could unambiguously

be related to the consolidant. In F3 we found smooth filament structures which clearly reveal the gel Figure 5-11, but again only sporadically distributed near the surface. We also found evidence of hydrophobic layers shown in Figure 5-11c. In all three samples we found no evidence of silica gel in the inner regions which supports our view that the higher neutron attenuation in the tomographic measurements are mainly due to the higher densities in these regions.

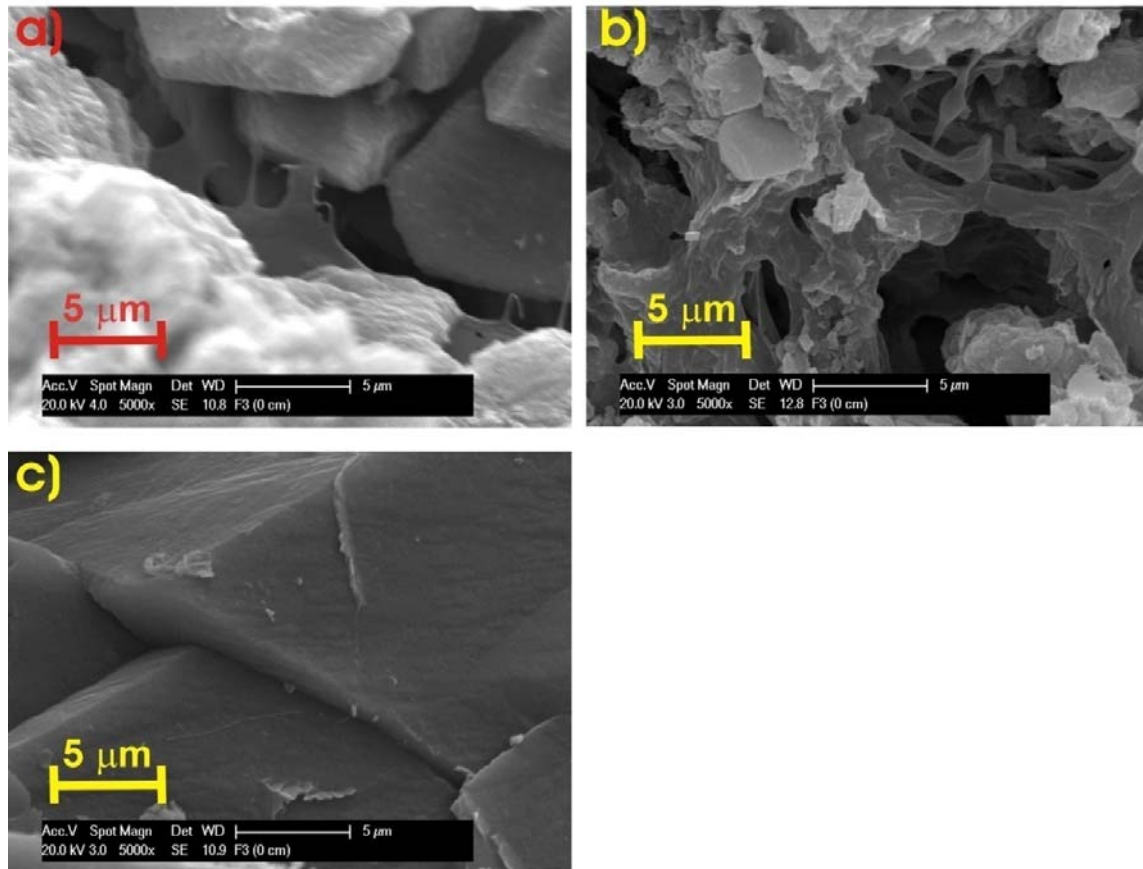


Figure 5-11: SEM detection of silica gel in F3: a) Fine filaments typical for gel formation b) Smooth amorphous gel structures in a pore c) Amorphous layers on grain surfaces indicate a thin hydrophobic film of silicone resin.

5.6 CONCLUSIONS

A comparison of the applied inspection techniques demonstrates that only the neutron method can provide a complete mapping of the strengthener. However, for an unambiguous identification of restoration agents the samples ideally should be measured before and after

St. Stephans Project

the consolidation treatment. Then neutron tomography is the preferred technique for systematic studies on the penetration and distribution of restoration products in building materials. One only has to consider the decreasing hydroxide content during drying over the first weeks and the long-term transformation of the silica gel because these processes reduce the neutron sensitivity. Neutron radiography is the preferred technique for a fast assessment of the impregnation procedure and the comparison of different restoration products.

The situation is more complicated if no information of the sample prior to the conservation treatment is available, as it was the case for the original cores from the Cathedral's facade. Then the distinction between hydrogen distribution (consolidant), different densities (crust, pores, fossils), and spurious elements (Fe), requires additional analysis with other techniques.

The comparisons of the results obtained with different techniques are in good agreement and allow a comprehensive assessment of the effectiveness of the applied restoration procedures. For the few provided samples it was found that the restoration products did not sufficiently penetrate the stones and that the hydrophobicity was not satisfactory in two samples. These results are surprising because they are in contradiction with our laboratory restoration experiments under ideal conditions using the same agents. More systematic studies are needed to investigate these discrepancies and in order to help to improve the restoration techniques.

6 INVESTIGATIONS OF STONE CONSOLIDANTS BY NEUTRON IMAGING.

6.1 Introduction

A stone consolidant should have sufficient stability and penetration so that the mechanical properties of the stone will be improved. The stone surface must not be sealed to ensure that the weathered stones are permeable to any existing humidity in the fabric as well as protected against further deterioration [Fleischer, 2005]. One of the properties that a consolidant must have is the ability to penetrate. The visualization of the penetration depth and distribution inside the stone is very helpful for conservators. Neutron imaging has been found to be very useful due to its high sensitivity and detection of hydrogen [Lehmann, 2005; Hameed, 2006; Cnudde, 2007]. Neutron transmission analysis is suitable for sandstones because they are made of quartz (SiO_2) or calcite (CaCO_3), which are weak-absorbing nuclei. In the case of weathered stones long after strengthening as the solvent evaporates, the neutron attenuation decreases. Neutron attenuation is therefore dominated by the hydrogen content [Hameed, 2008].

6.2 The consolidants

In this study, two consolidants have been used; silica ester (Wacker OH100) [Patent] and acrylic resin (Paraloid B 72) [DATASHEET]. These two types of strengtheners are very common in conservation. Silica ester is mostly used for the conservation of sandstone, whereas restorers use acrylic resin primarily for the conservation of marble or granite in Austria. In other European countries the use of Paraloid for the conservation of sandstones is also common. Silica ester is inorganic while Paraloid is an organic consolidant. There is a reluctance to use organic consolidants because acrylic resins are preferred by bacteria and other micro organisms. There is a danger of growing and feeding micro organisms. But if the change in physical properties is considered, the change of diffusion, strength, etc, paraloid maybe preferred in a low concentration as it fixes the particles together like glue. While silica ester fills the pores, reduces the water absorption and delays the dry out behavior.

6.3 Sample characterization and treatment

Three types of stone samples have been presented in this study. A fresh calcareous arenite from Aflenz, a calcareous arenite from St. Margarethen, and weathered quartz arenite sample form Flyschzone. A description of these samples has been given in Table 6-1.

Table 6-1: Characterization of the samples

Sample	Description	Treatment
Sample 1 (S1)	Cuboid with the dimensions 120mm x 51mm x 51mm. Calcareous arenite from Aflenz, Austria. Fresh sample from the quarry.	Strengthened with silica ester on one side and paraloid 5% on the other side.
Sample 2 (S2)	Cylindric with diameter 47mm, height 200mm Calcareous arenite, with large pores homogeneously distributed. From St. Margarethen, Austria.	Strengthened with silica ester on one side and paraloid 5% on the other side.
Sample 3 (S3)	Cylindric, diameter 47mm and height 180mm. Quartz arenite from the Flyschzone near Vienna; a strongly weathered sample from a building stone of the Cartusian Monastery in Mauerbach, Austria. Very homogeneous and fine pored.	Strengthened with paraloid 1%

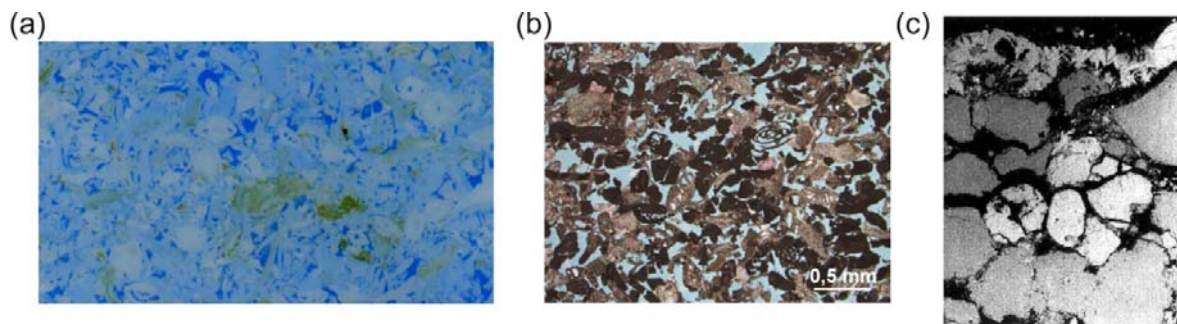


Figure 6-1: (a) Thin section of the highly porous calcareous arenite from Aflenz (blue stained resin) consisting of debris from calcareous red algae and foraminifers. (Length of the picture about 10mm) (b) Thin section of the highly porous calcareous arenite from St. Margarethen (blue stained resin) consisting of debris from calcareous red algae, echinoderms and foraminifers. (c) Thin section of

Investigation of stone consolidants

weathered quartz arenite from Lower Austria (Mauerbach) with a layer of crystallised gypsum on the surface (top of the picture); scale about 3x5 mm (crossed nicols).

The images in Figure 6-1 show the thin sections of the samples. The general physical properties have been given in Table 6-2. All these samples have been strengthened in the laboratory by capillarity method. The stone was placed in a glass bath containing the strengthener. After strengthening, the stone was removed from the bath and neutron tomography was performed.

Table 6-2: General physical properties of these stones

Properties	S1 - Calcareous arenite from Aflenz (Styria, Austria)	S2 - Calcareous arenite from St. Margarethen (Burgenland, Austria)	S3 - Quartz arenite from the flyschzone near Vienna (Austria)
Compressive strength-dry	9- 16,5 N/mm ²	49,0 N/mm ² (42,6 - 56,1)	70 N/mm ²
Apparent density	1,75 - 1,95 g/cm ³	2,08 g/cm ³ (1,97 - 2,26)	2,59 g/cm ³ (2,2 - 2,64) in correlation to the state of weathering
Water adsorption	12 – 16 M. %	7,9 M. % (3,6 - 10,2)	4 M. % (3 - 7)

6.4 . Experimental procedure and results

Neutron radiography (NR) and neutron tomography (NT) were performed. All samples have been strengthened in the laboratory by the capillarity method. The stone was placed in a glass bath containing the strengthener. After strengthening, the stone was removed from the bath and systematic NR and NT experiments were performed at the neutron imaging facility at Atomic Institute (ATI) in Vienna [Zawisky, 2008]. Later on neutron imaging was

performed at a higher flux at ANTARES, FRM 2 in Munich, Germany [Schillinger, 2004; Gruenauer, 2005].

6.4.1 Comparison of ethyl silicate and paraloid 5% measured at ATI

This experiment was performed with S1. The sample was strengthened with ethyl silicate on one side and paraloid 5% on the other side. From the results obtained, it was understood that the distribution of the two strengtheners is different. In the case of Paraloid 5% a high unwanted concentration of the strengthener on the surface was visible. This had to be investigated further. So experiments were planned at ANTARES where neutron imaging is performed with cold neutrons at a high flux. Hence a higher sensitivity and better resolution was expected.

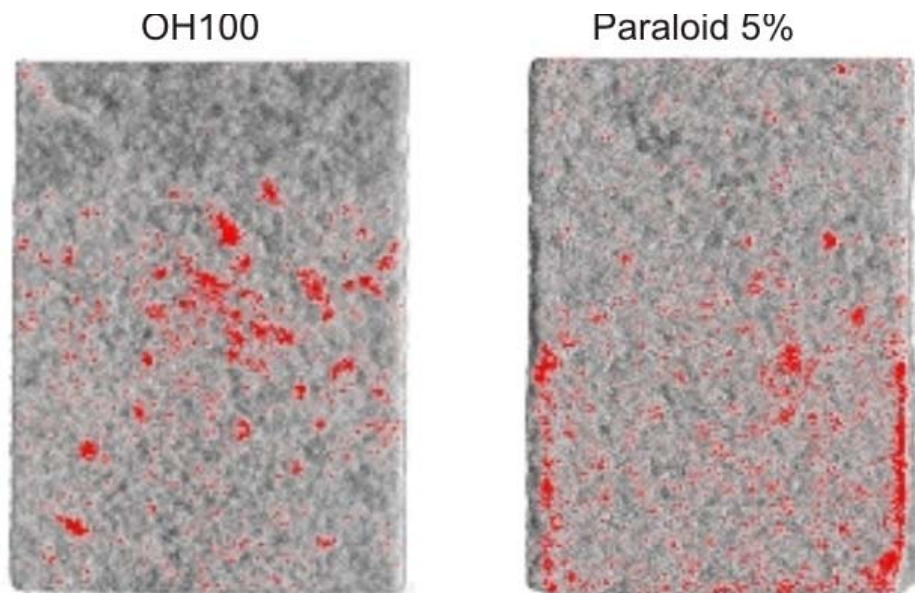


Figure 6-2: The NT of S1 with different consolidants. Left) A homogeneous distribution of OH100. In right, there is a surface effect. This NT was performed one month after strengthening when the consolidants had stabilized. The neutron attenuation was higher in the initial NT measurements and lower afterwards which is due to the evaporation of the solvent over time. A 400 μm ^6Li based scintillator and a CCD camera were used. The exposure time was 40s per image and the number of projections was 180.

6.4.2 Comparison of ethyl silicate and paraloid 5% measured at ANTARES

S2 was strengthened with the two different strengtheners then the NT measurements were made. These measurements were made with a commercially available scintillator (NE 426) coupled to a CCD camera. In this case the exposure time per image was 9s and the L/D ratio used was 800. The total number of projections was 400.

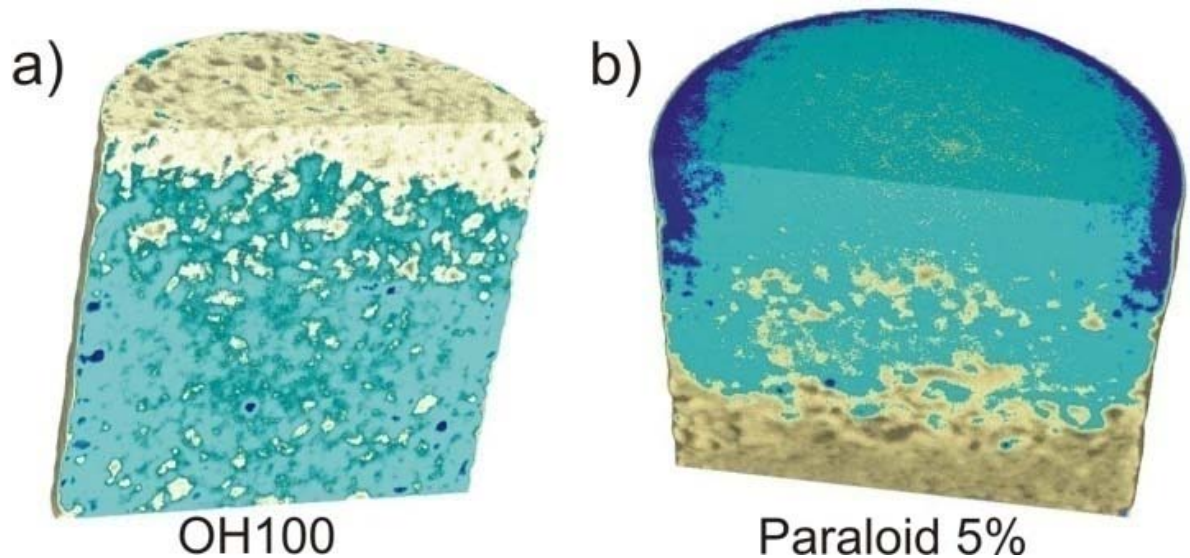


Figure 6-3: a) NT-bottom part of the stone strengthened with OH100. The NT measurement shows that OH100 is homogeneously distributed. b) NT of the top part of the stone strengthened with paraloid 5%. It is well visible that the distribution is different from the first case. The light colour shows low density of strengthener and the dark blue segments represent high density areas. These results are very interesting for geologists and conservators.

On the surface of the stone there is a high density distribution of paraloid. With the help of these measurements this effect can be clearly seen. It has been shown that the distribution of the two strengtheners in the same stone is different. Figure 6-3b shows the pores at the surface are completely filled which is very bad as humidity cannot leave the stone through the dense surface. A stone needs to “breathe”. In other words, the stone should remain permeable to water vapor and liquid, in order to avoid any build up of moisture (and consequent shear stresses) at the interface between the treated zone and the untreated stone below. After these results it was suggested that the concentration of paraloid should be reduced. Further experiments were performed with paraloid in 1% concentration.

6.4.3 Experiments with reduced concentration of Paraloid B72 on real weathered samples

Several weathered samples were investigated. The most interesting results have been discussed for S3. These measurements were performed at ATI. The concentration of the consolidant was now reduced from 5% to 1%.

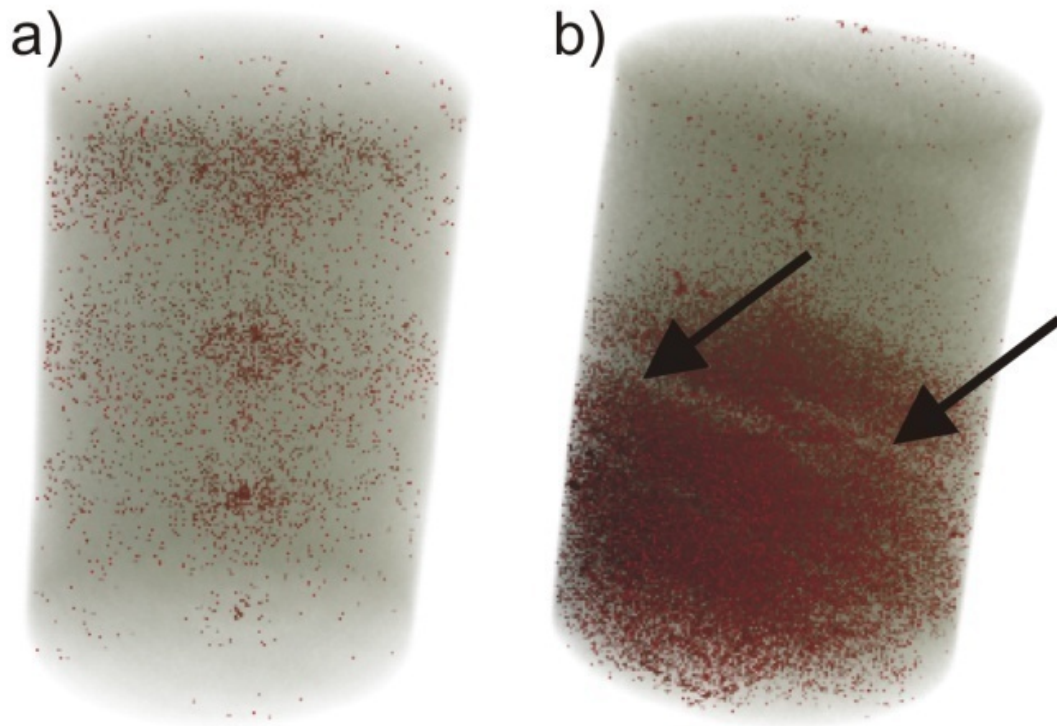


Figure 6-4: NT of S3; a) NT before treatment, the dark segments represent humidity or mica. b) NT after treatment with paraloid 1%. In b) the arrows indicate layers where a lower concentration of the solution is visible. Figure 4b) shows NT of the stone soon after strengthening. A low concentration of the dark segments could be a result of sedimentary layering in more porous weathered regions. A rather homogeneous distribution has been obtained. By reducing the concentration, there is no negative surface effect visible.

6.4.4 Time series experiments with different strengtheners.

Time series NR images were made during the strengthening process at ATI. An image was acquired every minute approximately. The line profiles obtained from these images may be used to determine the speed and depth of penetration of the strengtheners. For small absorption and scattering the neutron attenuation can be approximated by the exponential attenuation law. Neutron transmission due to single and multiple scattering are only slightly enhanced ($< 10\%$) at the tomography position. Using simple exponential attenuation, we get the transmission

$$T \cong e^{-\Sigma t} . \quad (6.1)$$

Σ denotes the total macroscopic neutron cross section, and t the path length through the sample. Using eq. (6.1) Σ can be determined from the NR image. This value was obtained for the strengthened stone and then the density of hydrogen ρ_H was found using eq. (6.2):

$$\rho_H = \frac{\Sigma_H A_H}{\sigma_H N_A} \frac{\bar{\lambda}}{\lambda_{th}} . \quad (6.2)$$

Where A_H is the atomic weight and σ_H is the microscopic cross-section of hydrogen at thermal wavelength $\lambda_{th} = 0.18$ nm. N_A is the Avogadro number. By transmission tomography the volume distribution of the total cross-section $\Sigma(x, y, z)$ can be visualized, which allows to distinguish volume effects from surface effects.

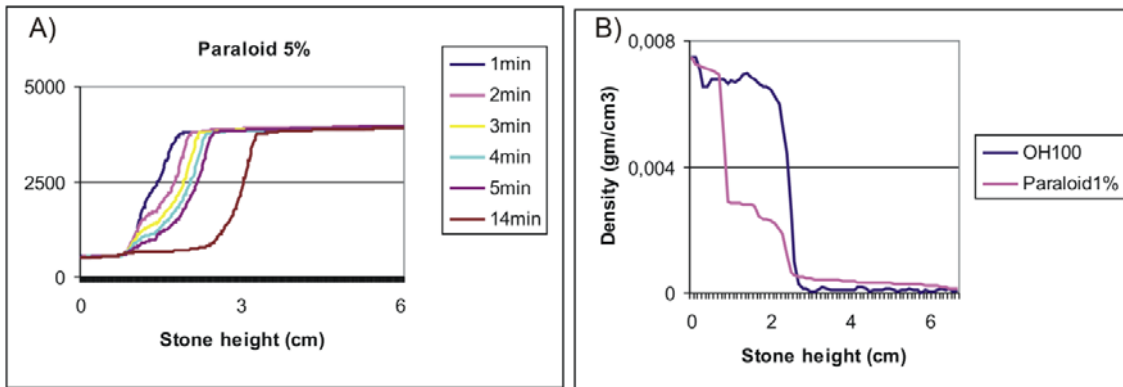


Figure 6-5: A) The line profile taken vertically along the centre of NR images of the time series. B) The density distributions of two different strengtheners along the height of the stone. The stones were strengthened to a height of approximately 3cm. The higher density at the bottom of the stone is due to the liquid in the bath.

6.5 Summary and Outlook:

Different penetration and distribution of the strengtheners have been found with NR and NT. The results show clearly that the penetration of different stone consolidants depends on the physical properties of the stones, pore size, grain size and state of weathering. Paraloid 5% is a very high concentration for a successful consolidation. The concentration has to be reduced. Neutron imaging techniques could become a very useful tool to evaluate conservation and restoration in combination with classical methods. NT is non-destructive and complete, yielding a 3D mapping of the consolidants.

7 NEUTRON SOURCES

A major field of neutron radiography applications is the inspection of nuclear fuel and control rods, reactor materials and components of irradiation devices for testing of nuclear fuels and materials [Domanus, 1992]. Cracks were detected in TRIGA fuel rods at the Atomic Institute by the method of neutron radiography [Pochman, 1977]. Non-destructive analysis of nuclear fuel has been performed by means of thermal and cold neutrons [Lehmann, 2003]. Except for their nascent condition all objects from this area are radioactive and have therefore to be handled carefully. Due to the high radioactivity and poor penetrability, X-ray radiography cannot be used.

Various issues can be addressed when neutron imaging is applied for nuclear applications. This method may be used to non-destructively check fuel assembly condition, check of component behavior, and check for leaks, quality control functional and dimensional evaluation and inspection of irradiation devices and components.

A neutron radiograph will distinguish between the isotopes of many materials since these often have very different neutron cross-sections. Such differences are readily detectable. Neutron radiography can be used for quantitative measurements if sample geometry and composition is known sufficiently. It must be made clear that this method detects material of high neutron attenuation cross-section only and is not able to label an individual element.

At the Atomic Institute in Vienna, different neutron sources are in use for instrument calibration and fast neutron applications. For the MCNP5 simulation of the experiments, the information about their geometry and material composition was required. Neutron imaging is a suitable method to get this information non-destructively. These investigations have been performed with digital imaging systems [Koerner, 2001; Zawisky, 2008] hence the quantitative determination and evaluation have been possible [Hameed, 2008].

As the sources are radioactive, care was taken with regards to radiation protection. The time, date and duration of the irradiation has been documented. The output of the isotopic neutron sources was the same after the irradiation. During these measurements, at 40cm distance, gamma ambient dose was measured to be 1.37 $\mu\text{Sv/hr}$ for the PuBe source and 438 $\mu\text{Sv/hr}$ for the AmBe source. For AmBe gamma background is high and can be shielded with

a thickness of 4cm lead because the energy of these gammas is very low, 60keV. The neutron strength of the source had a maximum value of 3Ci, which emits 5.65×10^6 n/s in 4π . In one meter distance, the ambient neutron dose rate can be 80 – 100 μ Sv/hr. This can be shielded with 40 – 50cm borated polyethylene or paraffin. In our case 30cm thick concrete was used for shielding. There is also a 10cm thick block of lead at the front part of the station for shielding gammas. The irradiation during the neutron imaging measurements did not change the neutron emission of the sources.

An area enclosed at a distance of 2m from the NR station was sealed during the measurement. As according to the radiation protection laws in the institute the radiation level outside the sealed area was below 10 μ Sv/hr total (including neutrons and gammas).

7.1 SAMPLES

Three isotopic neutron sources were investigated. Two PuBe sources of different sizes, a small one and a larger one and an AmBe source.

7.1.1 Plutonium-Beryllium (α , n) Sources

Plutonium forms an intermetallic compound with beryllium of the definite form PuBe_{13} with a density of 3.7 g/cm^3 . The conveniently available plutonium isotope is Pu^{239} , which emits 5.1MeV alpha particles. The half-life is about 2.3×10^4 years. The gamma rays emitted in the radioactive decay of Pu^{239} are weak and of low energy. Therefore Pu-Be sources offer the advantage of long half-life and the favorable characteristic of a low intensity of gamma radiation.

The source is enclosed in a steel cylinder. The shape and geometry of the source was not known. In order to simulate the shielding for the source the thickness of the container and the exact geometry of the source were required. With the method of neutron imaging it has been possible to obtain the required information non-destructively.

7.1.2 Americium-Beryllium (α , n) Sources

Americium also alloys with beryllium to form AmBe_{13} . Am^{241} has a half-life of about 470 years. Although this isotope decays by emitting alpha particles of about 5.4 MeV, these particles are followed by gamma rays in the 40 to 60 keV region in the majority of the disintegrations. This gamma-ray emission makes americium appear less satisfactory than plutonium for the preparation of neutron sources. The preparation of two types of sources with AmBe alloys has been described. One of these had a Be/Am atomic ratio of 263:1 and the other, identified as AmBe_{13} , had an atomic ratio of 14:1 [Curtiss, 1958].

7.2 Measurements and results

Non-destructive analysis of radioactive sources was performed at beam line NR II. Both the visualization of the structure of samples and its quantitative description are important aspects in materials research. A neutron source can be described in all its three spatial dimensions with the method of tomography. The three dimensional tomography of radioactive sources is more challenging due to the higher background level and long exposure times in the highly absorbing materials.

7.2.1 Neutron Radiography measurements

Two dimensional neutron radiography measurements were made using the scintillation detector and the neutron imaging plate (NIP) detector. According to the application, each detector has its advantages and disadvantages as has been discussed in the following sections.

7.2.1.1 PuBe source

The cross section of the source was estimated to see the feasibility of the measurement. The information available about the sample was that the source was in the form of an alloy PuBe_{13} . The density of alloy was 3.7 g/cm^3 . This alloy was enclosed in a steel container, the inner dimensions of which were not known.

The cross-section was calculated by the following formula [Domanus, 1992]:

$$\Sigma_c = \rho \frac{N_A}{A} \sum \sigma_i \quad (7.1)$$

Neutron sources

Where Σ_c - macroscopic cross-section of compound, cm^{-1} ; ρ - density of compound, $\text{g}\cdot\text{cm}^{-3}$; N_A - Avogadro's number, A – Atomic weight of compound; σ_i – microscopic cross-section of each atom, cm^2 .

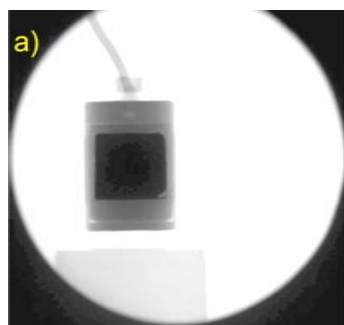
Table 7-1: Cross section values of the elements in the sample [Domanus, 1992]

Element	Atomic no.	Atomic weight	Macroscopic cross-section cm^{-1}			Microscopic cross-section in barns (10^{-24}cm^2)		
			Absorption	Scattering	Total	Absorption	Scattering	Total
Be	4	9	1.24×10^{-3}	0.865	0.865	0.0076	7.61	7.6176
Pu	94	239	57	0.478	57.5	1011.7		1011.7

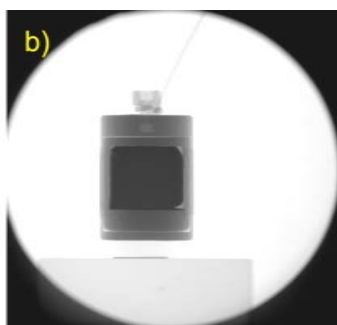
For the case of the PuBe source where plutonium forms an intermetallic compound with beryllium of the definite form PuBe_{13} [Curtiss, 1958], we have:

$$\Sigma_c = \rho \frac{N_A}{A} \sum (\sigma_{\text{Pu}} \cdot 1) + (\sigma_{\text{Be}} \cdot 13) \quad (7.2)$$

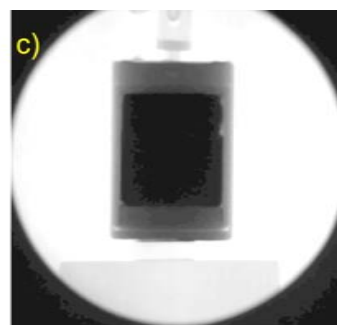
Substituting the values taken from literature [Curtiss, 1958; Domanus, 1992], the cross-section comes out to be 6.9 cm^{-1} , which shows that this material is highly absorbing. The transmission should be more than the background. Considering the parameters of the NR II facility and our experience with highly absorbing boron alloyed steels [Zawisky, 2004], this measurement should be possible.



a) Scintillator NR



b) Imaging plate NR



c) Scintillator NR

Figure 7-1: a) A neutron radiograph of a small PuBe source using the scintillator detector. The exposure time was 360s. b) Imaging plate radiograph with an exposure time of 50min. c) Neutron radiograph of the larger source obtained with the scintillator having an exposure time of 360s.

Neutron radiography images were made with different detectors. Figure 7-1a shows a NR image with a 0.1mm thin scintillator detector coupled to a CCD camera. The scintillator is a 0.1mm ZnS (Ag)-6LiF coupled to liquid nitrogen cooled Astrocam slow scan CCD camera. The exposure time was 360s and the sample was placed close to the detector. The camera chip has a sensitive area of 12.3 x 12.3 mm with 512 x 512 pixels; each pixel being 24 x 24 μm . The lens used for these measurements was Nikon NOKT 105 mm F 2.0. Imaging plate detector has also been used. The BAS-5000 IP Reader [Fujifilm] enables the scan of BAS-ND 20_25 cm^2 neutron sensitive imaging plates with 25 μm nominal and 40 μm effective resolution.

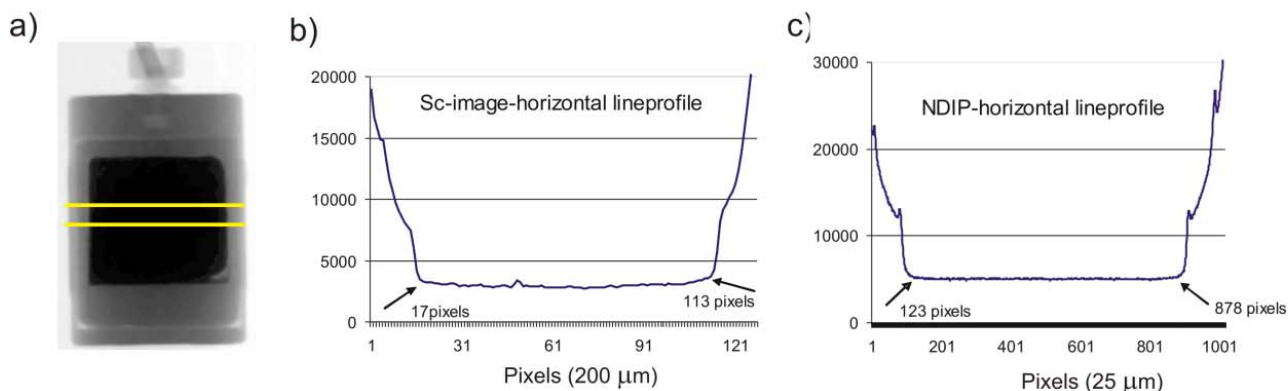


Figure 7-2: a) A scintillator NR of the smaller PuBe source made with an exposure time of 360s. b) A graph showing the horizontal line profile taken as shown in a). From the line profile the diameter of the inner alloy has been determined. c) A line profile taken horizontally from a neutron imaging plate NR.

In the NR images there are two steel cylinders one inside the other and then the source was inside. The empty spaces seen in the NR are filled with air. These may be called voids. The dimensions of the sample were determined by different methods. Using the software Image Pro [Image-Pro Plus 6.0 software], the grey values corresponding to the pixels could be determined. In order to extract data or pixel values from an image, line profiles are taken.

Figure 7-2 shows the line profiles for the images. Table 7-2 shows the values of the height and diameter of the inner alloy of the smaller source determined from the scintillator image and the NR made with an imaging plate detector. The imaging plate detector has a higher resolution and hence enables the determination of dimensions with a higher precision.

Table 7-2: The height and diameter of the inner alloy of the PuBe source has been determined using different methods

	Height (cm)	Diameter (cm)
Scintillator image (visually from the image)	2 ± 0.02	2.04 ± 0.02
Scintillator image line profile	1.76 ± 0.02	1.92 ± 0.02
NIP image line profile	1.88 ± 0.0025	1.64 ± 0.0025

7.2.1.2 AmBe source

A NR measurement of the source was made with the imaging plate detector. The sample was placed as close as possible to the imaging plate. This measurement was not successful. There was a high overflow. The reason for this was probably that this source is a high gamma emitter and the imaging plate is very sensitive to gamma. So the next measurement was made at a distance of 15cm from the imaging plate detector with an exposure time of 15 min. This measurement was successful, although it was not very sharp because of the large sample to detector distance. After this measurement more images were taken with different distances from the detector and with and without lead shielding to see the difference. These images have been shown in Figure 7-3. Increasing the distance between the detector and the sample leads to a loss of resolution. For the scintillation detector, it was possible to make a neutron radiograph with the sample placed close to the detector as the scintillator is not sensitive to gammas. Hence the scintillator image has been used for further analysis.

Neutron sources

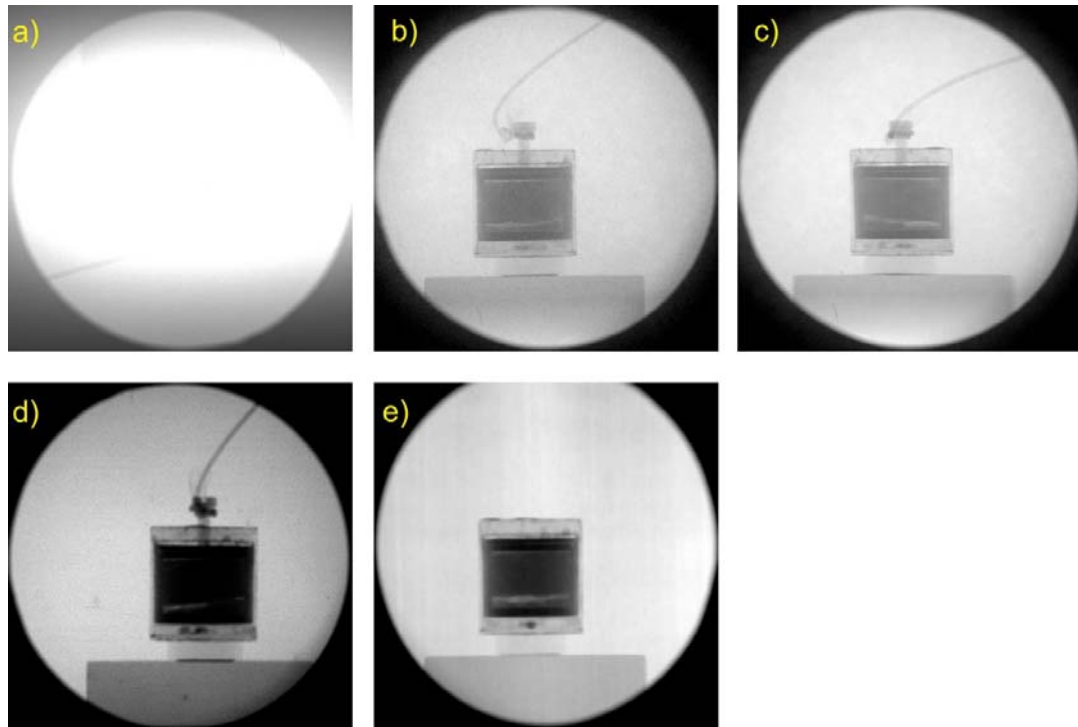


Figure 7-3: a) to d) shown neutron radiographs made with the imaging plate detector. These images have been made at different distances from the detector. Also images were made with and without shielding to get best results. e) is a scintillator image and hence is not affected by the gammas.

Table 7-3: Different NR measurements of the AmBe source

Image	Shielded	Detector	Distance	Exposure time	Mean counts
a)	Unshielded	NIP	6cm	20 minutes	54823
b)	Shielded	NIP	5cm	6 minutes	3056
c)	Shielded	NIP	6cm	30 minutes	14855
d)	Unshielded	NIP	15cm	15 minutes	30489
e)	Unshielded	Scintillator	Close to detector	6 min	30294

Neutron sources

Figure 7-3, a) shows the NR of the source placed close to the detector without shielding, which may be the reason for the high overflow. Shielding refers to a 3cm thick block of lead that was placed between the detector and the sample. Table 7-3 shows that with the NIP it was not possible to obtain a meaningful image close to the detector without any shielding placed in between. Although when the distance between the detector and the sample was increased to 15cm, NR image could be made without placing any shielding between the NIP and the sample. The scintillator may be considered to be suitable for the imaging of this source as it is not sensitive to gammas and the source can be placed close to the detector to obtain a sharp image.

The NR showed a crack in the source which led to the conclusion that it is not an alloy, but a powder pressed together. After the formation of crack, the crack was probably filled with helium gas as this was a product formed during the reactions inside the source. The material containing the source that is the container was thought to be steel. But from the neutron image it was found that there were two different containers, one inside the other. The two containers were made of different materials. In this image the source had been placed upside down. At the bottom of the source (which was seen at the top in the image), there seemed to be two layers of unknown material as the attenuation levels were different. It was then suggested to make a calculation of the cross-section of these materials with the help of which the density could be calculated and an attempt made to determine the material.

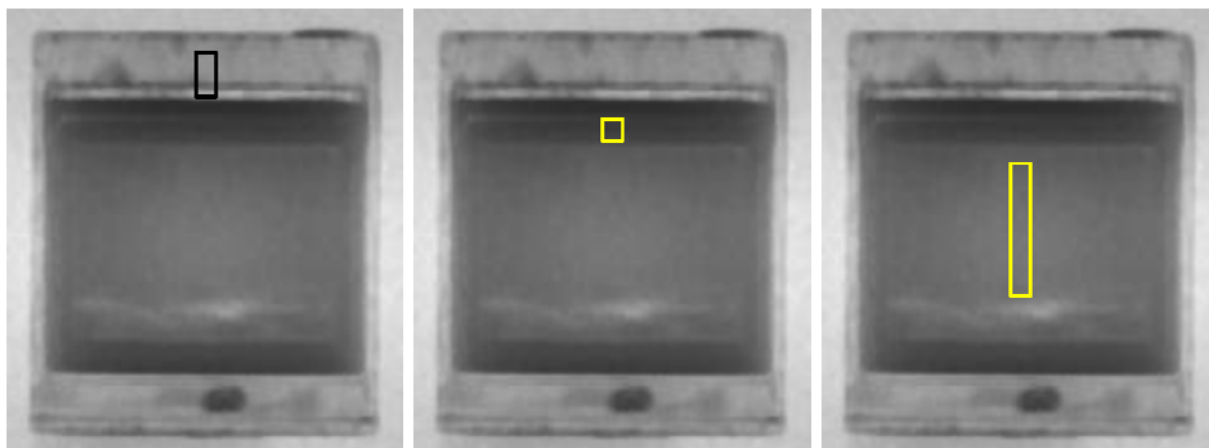


Figure 7-4: The NR image of the AmBe source. a) The rectangular area shows the area of interest that was analyzed to determine the material of the outer container. b) The rectangular area represents the

region analyzed to determine the material of the inner cylinder. c) The rectangular region was analyzed to find the density of the source which was required for the input file of the MCNP calculation.

For analysis, open and dark images were used. The sample image was rescaled. After applying a median filter and the corrections, an area of interest was chosen as shown in Figure 7-4. The mean intensity was measured from the histogram and the transmission calculated. Then the macroscopic cross-section can be given by:

$$\Sigma \cong \frac{-\ln T}{t} \quad (7.3)$$

T is the transmission and t is the thickness or the distance traversed by the neutron beam through the sample. For the area of interest (AOI) shown in Figure 7-4 a), the experimental value of the cross-section was found to be 0.122 cm^{-1} . The value of the cross-section [Domanus, 1992] 0.098 cm^{-1} corresponds to aluminum (Al). So it was concluded that the outer container is made of aluminum. By a similar analysis, the material corresponding to the aoi shown in Figure 7-4 b), which is the inner cylinder, is platinum or steel. In order to determine the density of the source, an aoi of interest as shown in Figure 7-4 c) was chosen.

Table 7-4: Dimensions of all three sources measured from the scintillator radiographs.

Source	Diameter of alloy (cm)	Height of alloy (cm)
PuBe-small	1.76 ± 0.02	1.92 ± 0.02
PuBe-large	2.8 ± 0.02	3 ± 0.02
AmBe	2.24 ± 0.02	1.5 ± 0.02

The experimental value of Σ , the macroscopic cross-section of the AmBe source was found to be 0.2029 cm^{-1} . Using the formula:

$$\rho \cong \frac{\Sigma A \bar{\lambda}}{\sigma N_A \lambda_{th}} \quad (7.4)$$

There are two possibilities of calculation of the density. The AmBe source can have Be/Am atomic ratio of 263:1 and the other, identified as AmBe₁₃, had an atomic ratio of 14:1 [Curtiss, 1958]. Using the first atomic ratio, the value of ρ is 0.4054 g.cm⁻³ and using the second ratio, the value of the density is found to be 0.6542 g.cm⁻³.

7.2.2 Neutron tomography measurements

Neutron tomography measurements of the PuBe source (small) were made with a 0.1mm Li based scintillator coupled to a CCD camera. Two sets of measurements were made. The first set comprised of 80 projections with an exposure time of 120s each. For the second set of tomographic measurement 150 projections were acquired each having an exposure time of 180s. As the source is highly absorbing, there were problems of enhanced background, strong absorption and beam hardening artifacts.

7.2.2.1 Correction of beam hardening

The use of polyenergetic thermal neutrons is very useful for the investigation of strong absorbing materials, because at the tail of the Maxwellian energy distribution the neutrons have sufficient energy to penetrate thick materials with large macroscopic cross sections. Surprisingly, such low transmission experiments can be performed with rather poor neutron intensities ($\approx 10^5$ n cm⁻² s⁻¹) [Zawisky, 2004], and even tomography of strong absorbing objects is now performed routinely at our beam line [Zawisky, 2004]. The disadvantage of using polyenergetic neutrons is the pronounced beam hardening artifact causing an enhancement of neutron transmission in thick and strong absorbing materials. The beam hardening effect yields inhomogeneities in tomography measurements, i.e., in the centre of the sample the density is apparently lower than expected from a homogeneous absorber distribution.

Neutron sources

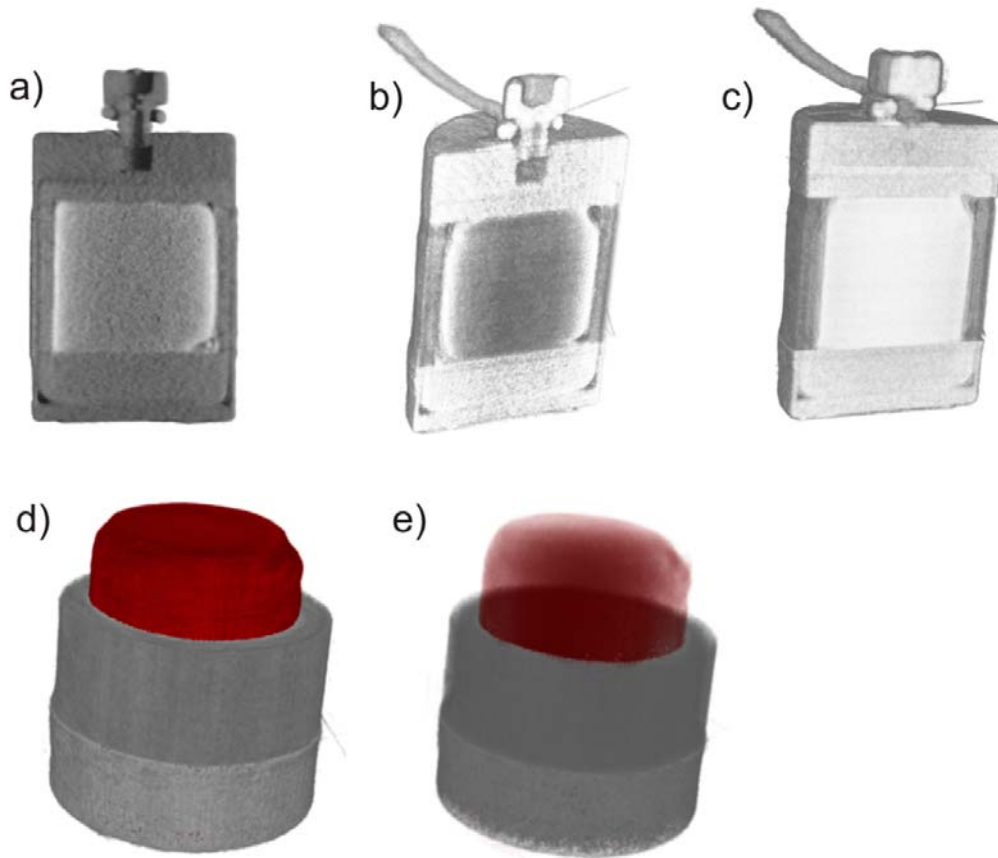


Figure 7-5: a) A reconstruction with Octopus software [Octopus software]. b) A reconstruction with IDL software without beam hardening correction. c) A reconstruction with IDL software with beam hardening correction. d) A 3-D view after beam hardening correction. e) A change in the transparency shows that beam hardening has been corrected to some extent; there are still regions which show a lower density.

In a simple model, where the Maxwellian neutron spectrum is approximated by a Gaussian, the beam hardening artifact can be corrected by an exponential term which depends only on the spectral width $\delta\lambda$ of the wavelength spectrum as additional parameter ($\delta\lambda = 0.075$ nm, $\lambda_{th} \equiv 0.18$ nm) [Zawisky, 2004]:

$$T_{corr} \cong T \cdot \exp\left(-\frac{\delta\lambda}{2\lambda_{th}} \int \sum_{ray\ i} \Sigma_i ds\right)^2 \quad (7.5)$$

The correction procedure is the following, using a self-written IDL (ITT Visual Information Solutions) program. First the macroscopic cross sections Σ_i and the source geometry are estimated from radiography measurements. Then, by assuming constant cross sections in Eq. (7.1), the exponential correction term is applied to the experimental transmission T when calculating the sinogram. The rest follows the standard filtered back projection algorithm. With this very simple but effective correction technique good results have been obtained for boron alloyed steel rods [Zawisky, 2004], and now also for strong absorbing neutron sources as shown in Figure 7-5. It should be mentioned here that the beam hardening correction indicates a smaller cross-section of approx. 5 cm^{-1} than the estimated value for the PuBe-source represented by the red regions in Figure 7-5.

7.3 Conclusions and outlook

The geometry of the neutron sources was determined with the method of neutron radiography. The unknown material density of the AmBe source was calculated. This confirms that the method of neutron imaging can be used to non-destructively get information about samples containing materials which have cross-sections that can provide a good contrast. Non destructive analysis of radioactive sources was performed. Both the visualization of the structure of samples and its quantitative description are important aspects in materials research. Another aspect is the three-dimensional investigation. Neutron radiography and tomography were performed to get qualitative and quantitative information about the sources.

It will be interesting to perform imaging of these radioactive sources with transfer technique [Domanus, 1992]. Traditionally, Dy or In is used as a primary detector where converter reaction by neutron capture takes place in fields with high gamma content. The induced activity is later used to stimulate a radiation sensitive film. Recently imaging plates have been used successfully instead of X-ray films [Lehmann, 2003]. Imaging plates have the advantage of higher sensitivity, the option for digitization and a high dynamic range. Films may have a better spatial resolution which may be required for some special applications. A regime can be applied for the extraction of the induced images on the imaging plate by either

Neutron sources

the short-lived component (for half an hour directly after the end of the neutron exposure) or some hours later (with image plate exposure for about 4 hours). These experiments were performed at PSI. At ATI we may make systematic studies of the comparison between these two different runs and determine the optimum exposure times in our case.

8 TEXTILE FIBERS

8.1 Introduction

Tencel Lyocell fibers are used in duvets. The basic requirement of a quilt is thermal insulation. During sleep the human body perspires, therefore moisture management of the duvet is essential for a comfortable sleep. The release of humidity has to be accommodated by the quilt. Hence moisture absorption and humidity transport are very important when designing a coverlet [Schuster, 2004; Abu-Rous, 2007].

Neutron imaging is suitable for studying moisture transport processes due to the sensitivity of neutrons for hydrogen [Zeilinger, 1976; Rauch, 1977; Weder, 2004]. Neutron radiography was used to investigate the moisture distribution in textile fibers under praxis conditions. Real time neutron radiography made it possible to follow the dynamics of the moisture transport without disturbing the ensemble during measurement.

8.2 Experiments and Results

The experiments were performed at the NR II station at the Atomic Institute. Here we have a collimated thermal beam having a neutron flux of $1.3 \times 10^5 \text{ cm}^{-2}\text{s}^{-1}$. Digitized neutron imaging with a high dynamic range of 16 bits can be performed. Different detectors may be used. Li based scintillator in combination with a CCD camera, 200 μm resolution and an imaging plate detector, 50 μm resolution. These detectors due to their characteristics have specific applications [Zawisky, 2008].

At the Atomic Institute we have a long tradition of neutron radiography. Moisture transport is one of the interesting topics we have been working on [Rauch, 1977; Hameed, 2006].

8.2.1 Dynamic neutron radiography

Dynamic neutron radiography or real time neutron radiography means that images can be made continuously after a fixed time interval depending on the exposure time chosen. So the process can be followed in real time without any disturbance to the experimental arrangement.

Textile fibers

A humidifier was used to provide moisture at a controlled temperature. On the humidifier, an aluminum box with a partition in the centre was placed. Non-woven fiber samples were placed in the two compartments of the box. Two layers of non-woven were used as half of the first layer could not be seen; it was hidden behind the wall of the humidifier.

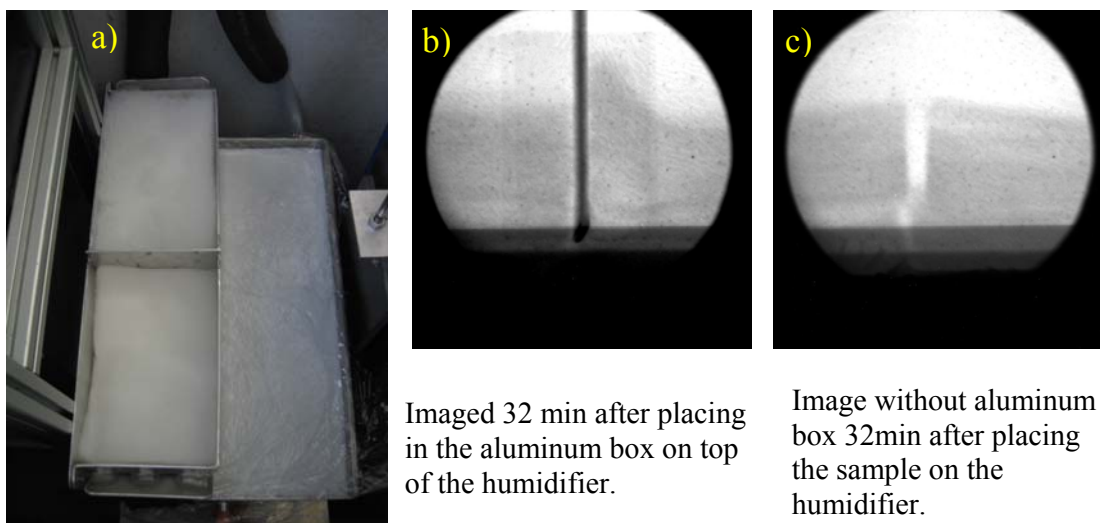


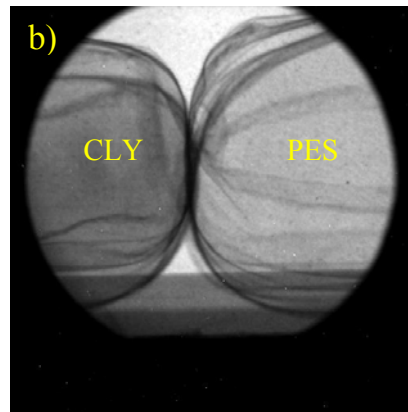
Figure 8-1:(a) The experimental arrangement showing the aluminum box placed close to the scintillator. (b) NR of the fiber samples inside the aluminum box. (c) NR of the fiber samples without the box. On the lower side the dark region shows the wall of the humidifier.

In the middle of the Al-box, there was a double wall of about 6mm thickness. This Al-layer is visible to neutrons and the area covered in the image is quite large. So the experiment was then performed without aluminum box.

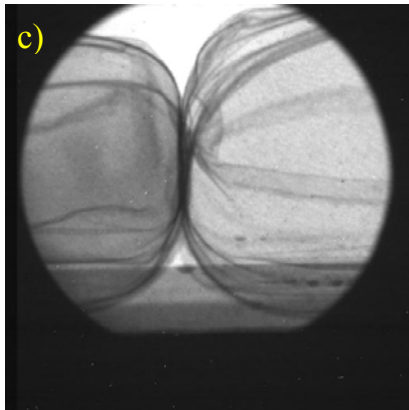
8.2.2 Experiments of fibers enclosed in pillows

The fibers were enclosed in stitched pillow bags, to simulate real conditions and to avoid evaporation. Aluminum wires were placed on the humidifier walls at a height of about 1.5cm in order to see the bottom of the fibers. The purpose was to raise the samples so that the lower part was not hidden behind the walls. The fibers were then placed on top of the wires.

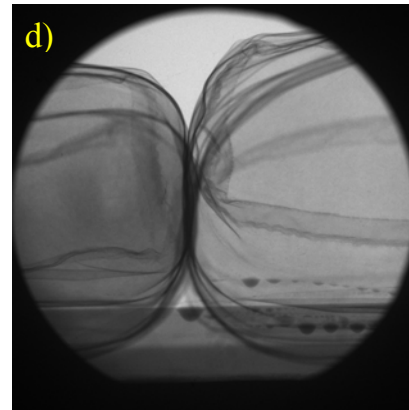
Textile fibers



Room temperature, after 53s, first image of the time series.



50°C temperature, after 80min, image number 90 of the time series.



NR with imaging plate detector after two and a half hours. Exposed for 10 min at a temperature of 50°C

Figure 8-2: a) the experimental arrangement showing the fiber samples in pillows. b) NR showing lyocell on one side and polyester on the other side. c) NR showing condensation along the wires after 80min. d) a high resolution NR made with the neutron imaging detector. CLY represents Lyocell and PES stands for polyester.

These were placed on the humidifier at room temperature of 24°C. A few images were made in these conditions. Then the thermostat was switched to a temperature of 35°C. A series of 90 images was started at room temperature. The temperature became stable at 35°C in about 15 minutes and was maintained for half an hour. After that the temperature was increased to 50°C (which took about 15 min). Again this temperature was maintained for half

an hour. During all this time, images were taken at an interval of 53 seconds (the exposure time being 40s with a grabbing time of about 13s).

A time series of neutron radiographs was made with the scintillator and CCD camera. The exposure time for each image was 40s. Then an image was made with the imaging plate detector. The exposure time for the imaging plate detector can be between 10min and 50min. An exposure of 50 minutes yields maximum hydrogen sensitivity and 16 bit image gradation. After exposure, time is required for scanning and erasing the plate before it can be reused. So the repetition interval between two such images would be about one hour.

No considerable difference in the water content in the fibers could be observed. Maybe this was due to the pillows (covers). It was then decided to perform the experiments without pillows.

8.2.3 Imaging plate neutron radiography measurements

Imaging plate was then used to get a high resolution image in the beginning of the dry sample (sample at room conditions) and after humidifying at 35°C. Then the difference in the gray values can be seen qualitatively and quantitatively.

The fibers were placed without the pillows (covers) directly on the humidifier without using wires. The condensation of the water is clearly visible at the image in Figure 8-3 where the temperature difference from the surroundings is almost 40 °C. Due to the temperature differences, the water condensation takes place on hydrophobic polyester fibers. Hygroscopic Lyocell fibers absorb water, the neutron images appear in dark–grey color.

Textile fibers



Photo at the beginning of the experiment



Photo at the end of the experiment. The CLY fibers seem to have collapsed.

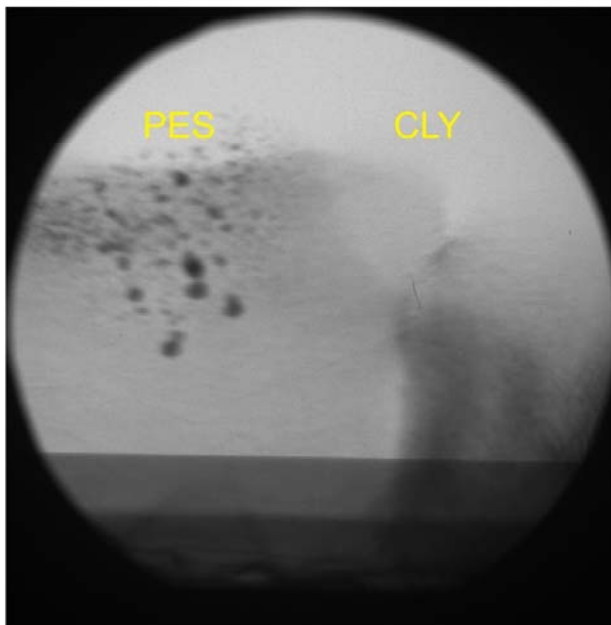


Figure 8-3. Top: Experimental setup. The humidifier was filled with water (textile was fully wet) and the Lyocell foil was placed on the top of the wet textile. In this setup, the wires weren't used to make a distance between the foil and textiles. Bottom: Imaging plate NR of the filling fibers, exposure time 10 min at 62C. This image shows the condensation near the surface; it seems that the water droplets are placed "above the fiber sample". This phenomenon has to be clarified.

Textile fibers

The image in Figure 8-3 raised the question if the condensation occurs on the polyester fiber or on the walls of the imaging plate as well. This was checked by imaging without the sample and no condensation was found. So it can be said that the condensation was not on the detector.

Figure 8-4 shows the images with the imaging plate at different temperatures. These images were made with an exposure time of 10 minutes. The graphs show the change in moisture with respect to temperature and time.

The analysis was done by measuring the grey values. The lower the value, the higher is the quantity of water absorbed by the sample. In case of small absorption and low scattering, the neutron attenuation can be approximated by the exponential law:

$$I \cong I_0 e^{-\Sigma t} \quad (8.1)$$

Where I is the intensity of the transmitted neutrons after penetrating a distance t into the target. In our case t is the thickness of the sample. I_0 is the intensity of the beam incident on the sample. Σ is the macroscopic cross-section. The measurement of neutron transmission through the sample allows in principle an absolute determination of the sum of cross sections and densities in the sample:

$$T = \frac{I}{I_0} = e^{-\Sigma t} \quad (8.2)$$

$$\Sigma = \sum_i \Sigma_i \quad (8.3)$$

$$\Sigma_i = \frac{N_A \sigma}{A} \rho_i \quad (8.4)$$

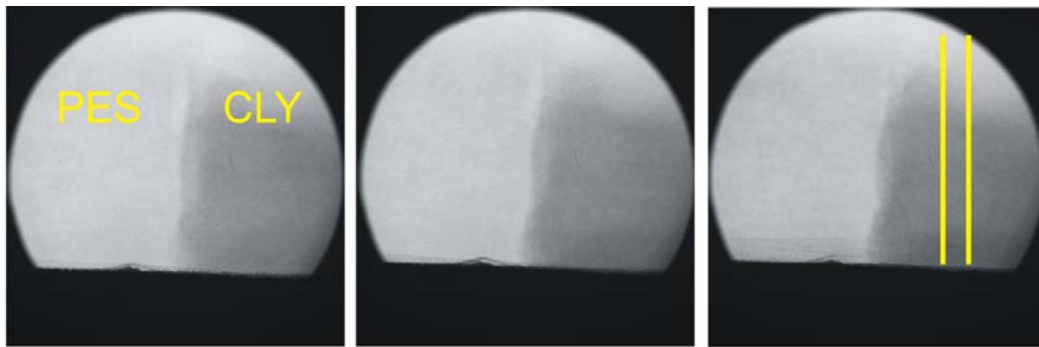
From the neutron radiograph, the macroscopic cross-section can be calculated. From the macroscopic cross-section, the density of the material may be determined. ρ is the density of the material in gcm^{-3} , A is the atomic weight, N_A the Avogadro's number and σ the microscopic cross-section in cm^2 .

In this project we are mainly interested in the water content, therefore one has to normalize the intensities behind the wet sample to the dry sample in order to determine

Textile fibers

$$T_{water} = \frac{I_{wet}}{I_{dry}} = \exp(-\Sigma_{water} t) \quad (8.5)$$

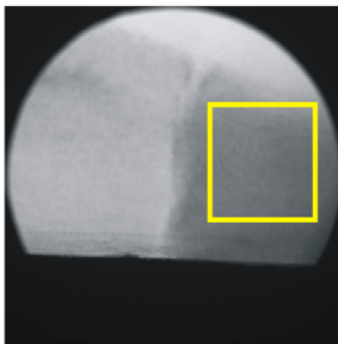
From Σ_{water} the absolute water density ρ_{water} could be evaluated. This was not possible in this project because dry samples have not been prepared for the measurement of I_{dry} .



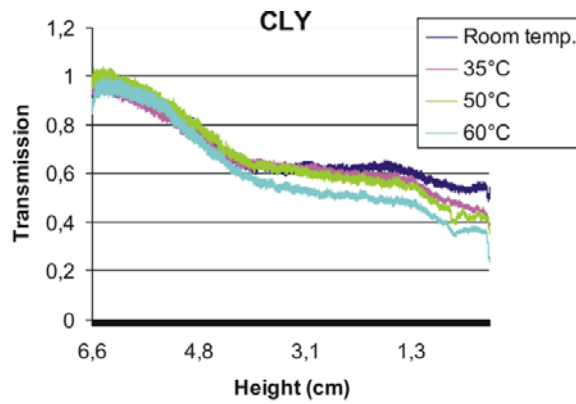
At room temp.

At 35°C

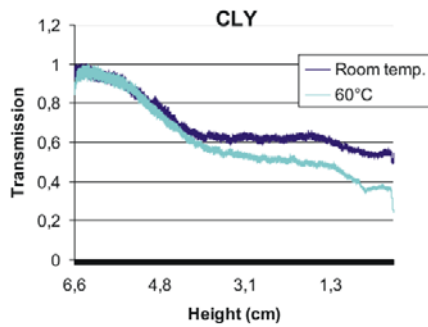
At 50°C



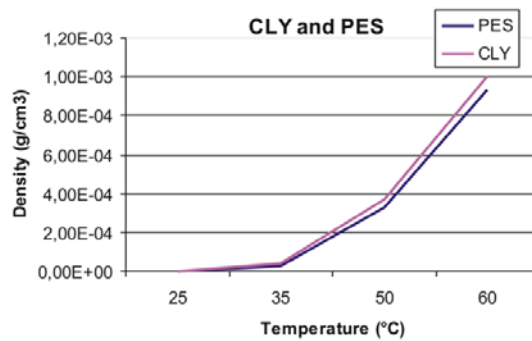
At 60°C



Graph 1



Graph 2



Graph 3

Figure 8-4: Neutron Radiographs with imaging plate detector, starting with room conditions. Graph 1 and graph 2 show the line profiles taken along the height of the lyocell fiber at different temperatures. Graph 3 shows the preliminary analysis of the density of water or hydrogen relative to temperature.

From the graphs in Figure 8-4 it can be seen that the temperature has a detectable influence on the water content. The higher the temperature of humidifier, the higher is the water content and the lower is the neutron transmission. Time of the sample at certain temperature is not a considerable influencing factor because the grey-values do not differ a lot when exposing the sample at 35 °C for a longer time period.

For graph 1 shown in Figure 8-4, a line profile was taken vertically along the height of the sample starting from the bottom to about 2cm above the Lyocell sample. The height of the Lyocell sample was 4,5cm and that of the polyester sample was 6cm. The transmission was calculated and plotted relative to the height. Lower transmission corresponds to higher value of moisture content. So we see that there is higher moisture content on the lower part of the sample which is close to the humidifier. As the temperature increases, the transmission decreases and hence the moisture content increases. Graph 2 shows a significant change with temperature. There is a non linear relationship between the transmission and the water content.

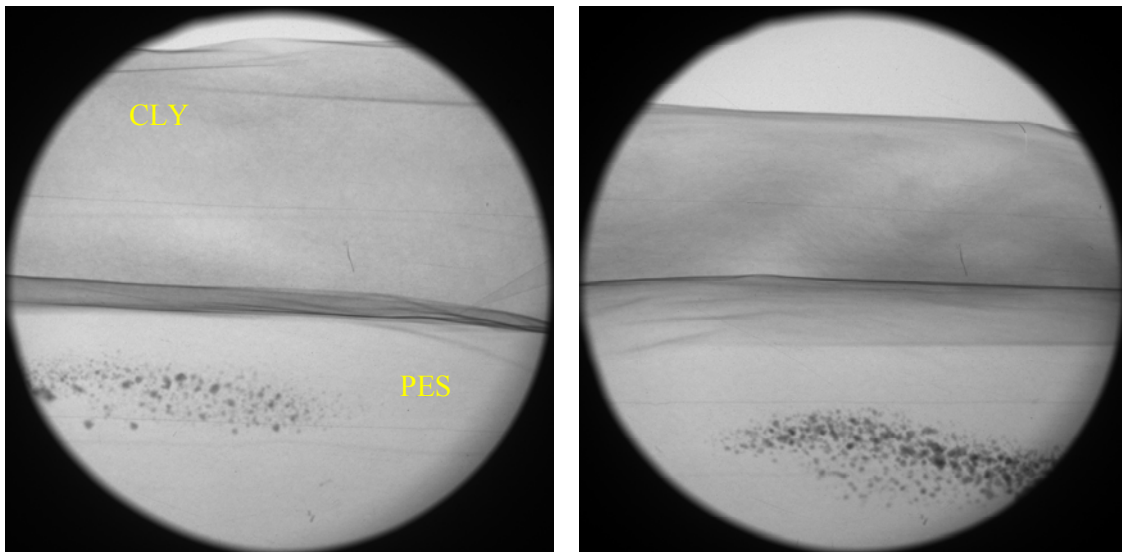
An analysis was done of the density of water in the two kinds of fibers relative to temperature. This density is not an absolute value. I_0 is not I_{dry} , so Σ and ρ are not Σ_{water} and ρ_{water} respectively. If I_{water} is known, the value of ρ_{water} can be determined. As we don't know the density of the completely dry samples without any humidity, we have taken a difference between the wet sample and the sample at room conditions which contains a certain amount of moisture. It has been assumed that $I_0 = I_{dry}$ for the determination of ρ_{water} . This analysis has been presented in graph 3. The area of interest for this analysis was a square area chosen each on the Lyocell sample and the polyester sample as shown in Figure 8-4.

The sample changes its shape a little bit during the experiment. After the experiment was done, the sample mass was determined gravimetrically. Polyester fibers seem to distribute moisture very homogenously all over the sample while for Lyocell fibers, the water remains more at the bottom of the sample. Lyocell sample was not wet homogenously. Lyocell fibers absorb water into the fiber structure and therefore the water transport is not so

quick like for polyester fibers. Polyester fibers have high surface water-conductivity and that's why the water is distributed homogenously all over the non-woven.

8.2.4 Imaging of fiber samples enclosed in plastic bags

The two types of fibers Lyocell and polyester were humidified to different levels or percentage of humidity and enclosed in plastic bags. Then neutron imaging was done under stable conditions, due to which the exposure time was increased to 50 min to get a higher sensitivity.



Imaging plate NR of the fibers in a plastic bag with 10% humidity.

Imaging plate NR of the fibers in a plastic bag with 30% humidity.

Figure 8-5: Neutron radiographies made with an imaging plate with an exposure time of 50 minutes. These images clearly show the humidity distribution in the two types of fibers.

8.3 OUTLOOK

A quantitative analysis of the mass fraction of water is possible. For this purpose the value of the density of the completely dry sample is required. The relation of the humidity content with temperature and time may be studied. A comparison can be made with the gravimetric analysis. Such an investigation can give interesting insight into the diffusion phenomena.

Textile fibers

Further experiments can be performed using H₂O and D₂O. Light water and heavy water give a very good contrast for neutron radiography. This can be useful for investigating moisture transport in moist samples [Rauch, 1977]. Neutron tomography under stable conditions can also be performed to get a three dimensional distribution of humidity.

9 HYDROGEN TRANSPORT STUDIES

9.1 Introduction

Water in building materials like stones and concrete can be detected with a high sensitivity using the method of neutron imaging. The method of neutron imaging is suitable for studying moisture transport due to the high cross-section of neutrons for hydrogen [Arif, 2003]. Neutron radiography experiments have been performed in the past with a film detector to investigate the diffusion of water [Rauch, 1977]. Rauch studied the diffusion of light and heavy water due to the good contrast that hydrogen and deuterium have for neutrons. [Pleinert, 1998] developed a method for the neutron transmission analysis using point scattered functions. [Pel, 1993; Abd, 2004; Cnudde, 2008] carried out studies on the diffusion of water inside porous building materials. Recently [Hassanein, 2006] has developed a quantitative neutron imaging program based on [Pleinert, 1998] and [Kardjilov, 2005]. This software makes corrections to the scattering disturbances in radiography images. The advantage of modern digital detectors is the high linearity with the beam intensity and a high dynamic range. Along with visualization, the quantification of the water content is also possible. Another improvement is the shorter recording time and better reproducibility. A time series of neutron radiography measurements can be compared pixel wise. A loss of sharpness and resolution compared to the film method is the drawback of digital detectors.

Projects based on the hydrogen sensitivity of this method to study the transport of hydrogen in building materials and textile fibers have been carried out. Dynamic neutron radiography made it possible to follow the dynamics of the moisture transport without disturbing the ensemble during measurement.

9.2 Hydrogen detection sensitivity in thin materials at ATI

To quantify the hydrogen content in rocks and consolidated stones one has to consider single and multiple scattering. In thin samples and sufficient detector distance the beam attenuation is determined by Eq.(9.1) using the total macroscopic cross section $\Sigma = \Sigma_a + \Sigma_s$ ($\Sigma_{a,s}$ = absorption, scattering cross sections). Multiple scattering occurs if the sample thickness d approaches the neutron's mean free path length ($L = 1/\Sigma_s$); it enhances neutron

transmission and causes deviations from the ideal exponential transmission law [Sears, 1975]. Figure 9-1 gives an example for hydrogen quantification in a calcareous arenite with 4 mm thickness. From the measured hydrogen density one derives a mean path length of $L = 40$ mm and a thickness-to-path-length ratio of 0.1 which indicates that multiple scattering remains negligible in wetted thin-slices. Empirically, by changing the sample-to-detector distances from 2 – 29 cm, we found no scattering artifacts in wetted slices up to 4 mm thickness, and only a slight transmission enhancement of 10 % at 1 cm detector distance.

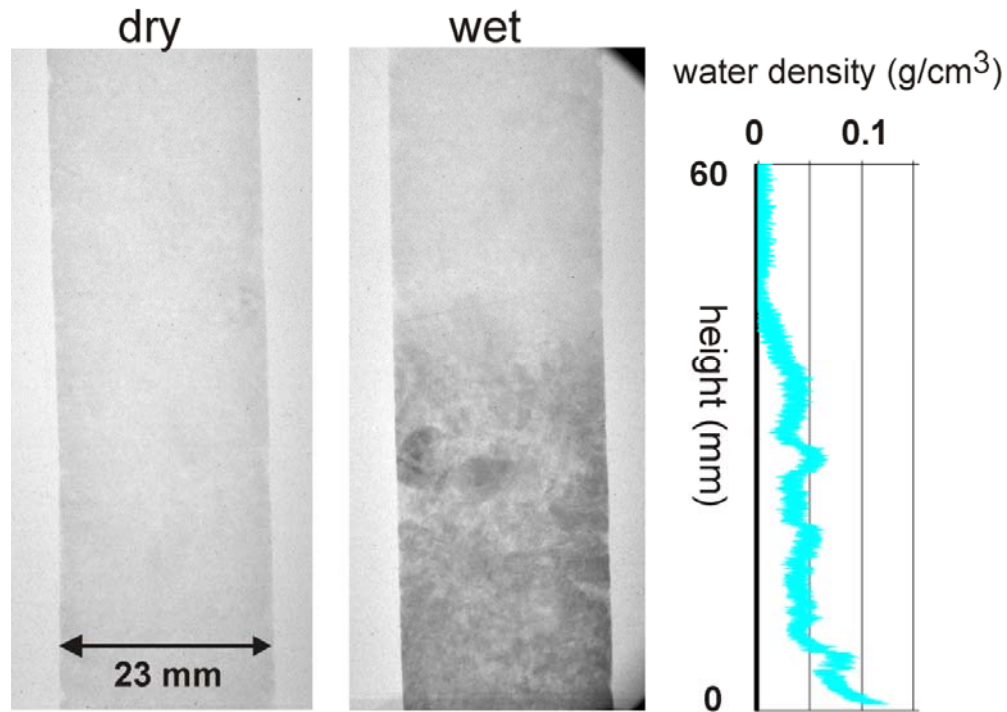


Figure 9-1: NIP images of a 4 mm thin-slice calcareous arenite in dry and wet condition after 30 min wetting in a soaking bath. The density profile was determined along the vertical axis in steps of 25 μm .

A lower bound for density resolution $\Delta\rho$ in small sample areas can be derived from the variance of pixel count numbers in the area of interest [Sears, 1983]:

$$T_{water} \cong \frac{N_{wet}}{N_{dry}} \cong e^{-\Sigma d} = \exp\left(-\frac{\rho \sigma N_A d}{M}\right) \quad (9.1a)$$

$$\Delta\rho_{water} \geq \sqrt{\left(\frac{\delta N_{wet}}{N_{wet}}\right)^2 + \left(\frac{\delta N_{dry}}{N_{dry}}\right)^2} \frac{M}{d \sigma N_A} \quad (9.1b)$$

Here, N_{wet} , N_{dry} represent the total count numbers of the wet and dry samples in an area of interest, with variance δN . As shown in [Zawisky, 2008] the scintillator's and imaging plate's variances of pixel values are larger than the ideal Poissonian variance. σ denotes the microscopic cross section of water, M the molecular weight and N_A the Avogadro constant. The statistical accuracy in density measurements of wetted thin-slices with 4 mm thickness Figure 9-1 reaches 10^{-3} g/cm^3 in 1 mm^2 region of interest ($= 40 \times 40$ pixels), when analyzing a full dynamic range NIP image, i.e., $N_{\text{dry}} \approx 60000$ counts in the $25 \times 25 \mu\text{m}^2$ pixels.

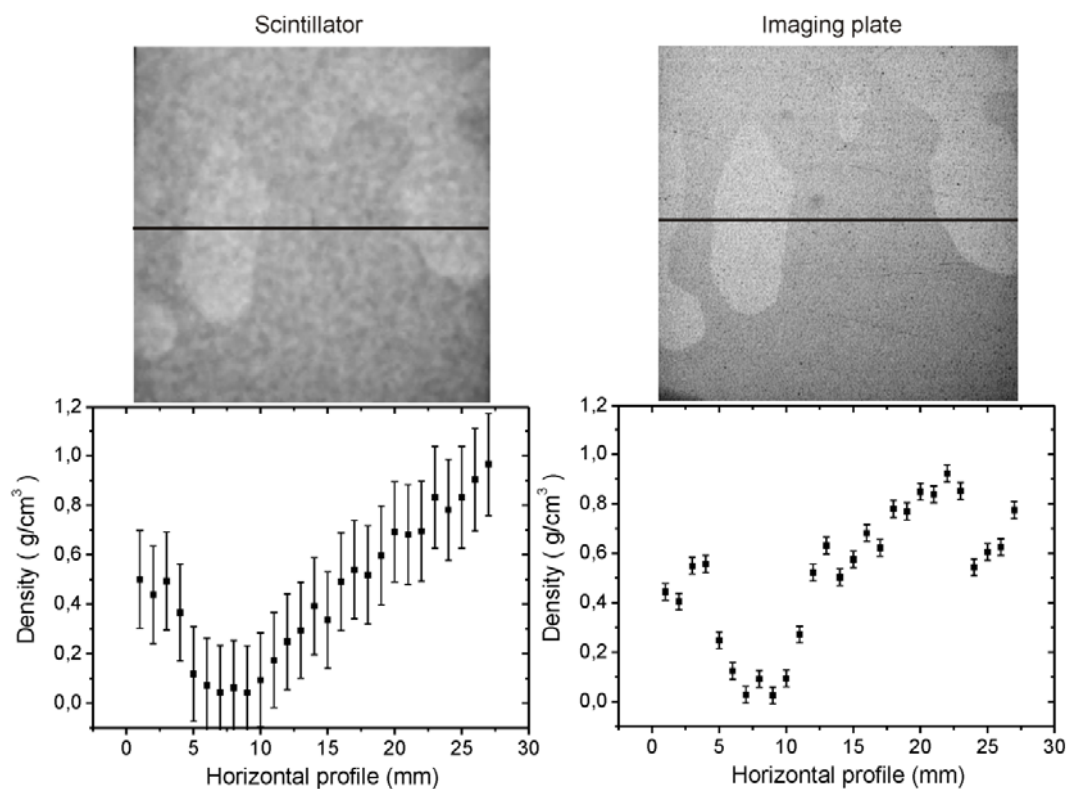


Figure 9-2: Comparison of two full dynamic range images of a thin water layer between two aluminum plates with $40 \mu\text{m}$ thickness on average. Left: $100 \mu\text{m}$ thin plate scintillator with $200 \times 200 \mu\text{m}^2$ optical resolution. Right: Imaging plate, $25 \times 25 \mu\text{m}^2$ readout resolution. Dry and wet regions are clearly resolved in both detectors but the better spatial resolution of the imaging plate allows a more precise density analysis (contrast of the raw images enhanced only for presentation).

Finally, spatial resolution and hydrogen sensitivity of the imaging plate and the thin-plate scintillator have been investigated. Figure 9-2 shows neutron images of a thin water film

with 40 μm thickness on average, where the NIP provides a much sharper picture and higher sensitivity to film inhomogeneities. According to Eq. (9.1) the images of the wet sample have to be normalized to the dry images for determining the water density. The density resolution in the film approaches $\Delta\rho \approx 0.03 \text{ g/cm}^3$ using the imaging plate, but only $\Delta\rho \approx 0.2 \text{ g/cm}^3$ with the scintillator due to the much lower total count numbers in the areas of interest. By choosing areas of 1 mm^2 along the black lines in Figure 9-2 for density analysis one integrates 5×5 pixels in the scintillator (200 μm optical resolution) but 40×40 pixels in the imaging plate (25 μm resolution). When comparing full dynamic range images the higher resolving detector also yields higher sensitivity in the same area. To achieve high sensitivity and image gradation full 16 bit pixel saturation is required, i.e., 50 min exposure time with the NIP at 25 μm pixel resolution.

9.3 Investigation of liquid transport by dynamic NR

Neutron radiography studies of the mutual diffusion of light and heavy water were first performed by [Chountas, 1968] at temperature of 0-15 $^{\circ}\text{C}$. Based on the Fick's second law the diffusion coefficient could be determined when an experimentally obtained concentration profile was available. Concentration profiles were obtained after different times after the start of the diffusion process. The diffusion results had a good agreement with literature, but some significant deviations were observed as expected for a constant diffusion coefficient. These deviations suggested a concentration dependence of the diffusion coefficient. Hence more detailed investigations were undertaken [Rauch, 1977].

[Pel, 1993; Abd, 2004] also made similar studies for the diffusion of water in porous building material and calculated the diffusion coefficient of water in porous stones. The diffusion coefficient was referred to as moisture diffusivity.

[Pleinert, 1998] developed a neutron transmission analysis technique based on the Point Scattered Functions. This technique was optimized for the study of moisture in building materials to extract the quantitative information from the experimental data. The diffusion coefficient were referred to as moisture transfer coefficient.

The exponential law of attenuation equation (5.1), is for an "ideal" neutron radiograph transmission image with a monoenergetic neutron beam. In reality there are deviations from

this law due to various factors. A considerable factor is the neutron scattering. The neutrons scattered from the sample appear as an extra intensity in the radiographs, which lead to the interpretation of reduced attenuation or as lower mass density of the material. Apart from this, neutrons that do not pass through the sample can be scattered at the surrounding of the sample, for example the camera box or at the neutron shielding. This background scattering leads to an extra intensity at the detector. As the neutron beam is usually polyenergetic, there are further distortions. Beam hardening effects may be expected as the cross sections of materials for neutrons usually decrease with increasing neutron energy. So the effective attenuation coefficient decreases with the sample thickness. As the neutron spectrum behind and in front of the sample is not the same, the energy dependent detector efficiency has to be taken into account.

In order to make corrections for the effects mentioned above, [Hassanein, 2006] developed a correction algorithm based on [Pleinert, 1998; Kardjilov, 2005]. This software is known as QNI (Quantitative Neutron Imaging). This software was applied to investigate the penetration of water and NaCl solution in different stones [Hassanein, 2006]. Various transport phenomena are involved in the process of moisture transport. These phenomena include capillary transport and diffusion and involve the transport of water in both gaseous and liquid phases. A simple expression to describe capillary uptake is obtained by solving the Washburn equation (9.2):

$$x = \sqrt{\frac{\sigma r_{eff}}{2\eta\gamma^2}} \sqrt{t} \quad (9.2)$$

In the above equation, the intrusion depth of the water front is represented by x , the surface tension by σ , the viscosity of water by η and t is the time. γ denotes the tortuosity and the effective capillary radius of the stone pores is r_{eff} .

[Cnudde, 2008] also made a similar analysis and made a confirmation by comparing with classical geological methods. A simple model of capillary transport approximates the wetted region as a saturated wet front, ‘a sharp wet front’ or a ‘moving boundary’. Using the following equation, the penetration coefficient can be determined:

$$x = b\sqrt{t} \quad (9.3)$$

x represents the penetration depth of the wet front, is the length-related penetration coefficient which can be determined experimentally based on the radiographs taken over time.

Analyses have been made to study the penetration of water in different stones that are used in historical buildings and monuments in Vienna using the method of dynamic neutron imaging.

9.4 NR series of the imbibition of H₂O with thermal neutrons at ATI

NR series were made of IV17-STM which is a fresh calcareous arenite from St. Margarethen. This was a cylinder of height 20cm and diameter 4.7 cm. The NR measurements were made at ATI with a 400 μm ⁶Li based scintillator. The distance between the sample and the detector was 9 cm. The exposure time for each image was 40 s. The sample was placed in a bath containing water and then the measurements were made. Before starting the time series, a NR image of the dry sample was made for reference.

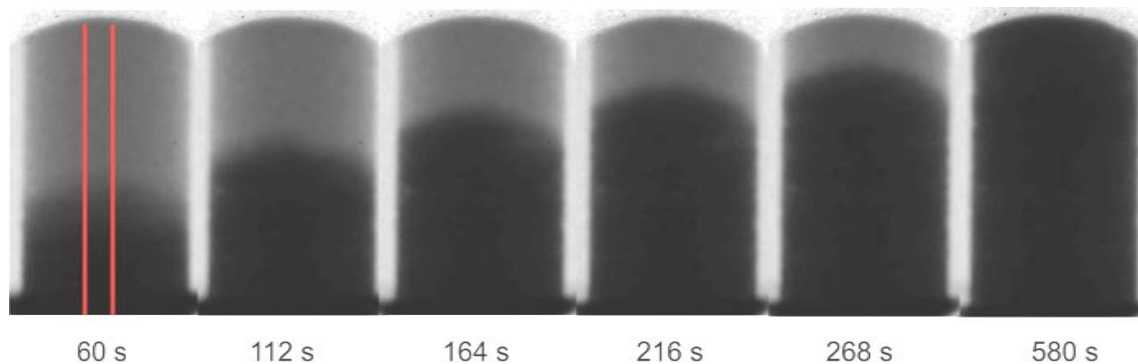


Figure 9-3: Time series showing NR after different intervals of time. The red lines represent the line profile take vertically.

Figure 9-4, left shows the transmission line profiles of the neutron radiography images taken after different time intervals. The right side shows a graph of the water wave front position versus the square root of time. This graph is for the 10th image which was made after about 9 minutes. This was the last image in this radiography series as the field of view was limited and the water had reached the maximum height visible in this field of view, which is

about 9 cm. The slope of the curve gives the penetration coefficient which in this case is $0.35 \text{ cm s}^{-1/2}$.

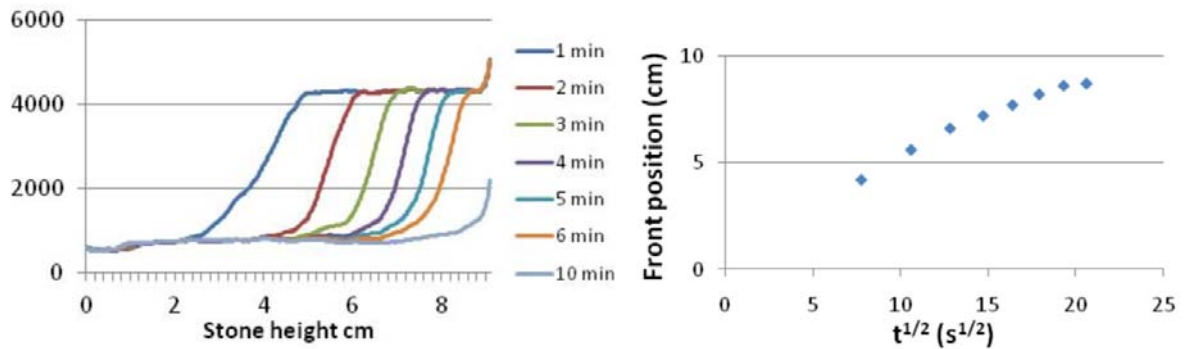


Figure 9-4: Left – line profiles showing the penetration of water in the stone after different intervals of time. Right: A graph showing the front position versus the square root of time. The slope of this curve is $0.35 \text{ cm/s}^{1/2}$.

In Figure 9-5, the mass thickness of water has been evaluated. The mass thickness of water refers to the amount of water vertically along the center of the stone expressed in g cm^{-2} . This quantity of water has been evaluated from the transmission data of the neutron radiograph number 10. The right side shows the evaluation after correction for the distortions mentioned in section 9.1 with the QNI software.

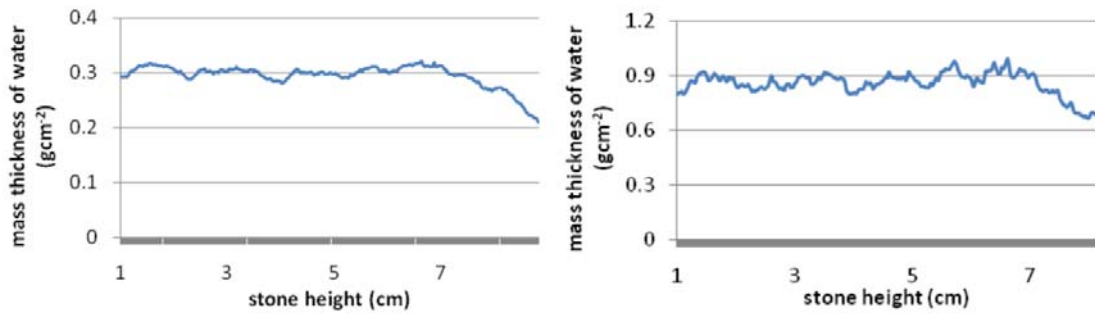


Figure 9-5: Left: the mass thickness of water in the stone calculated without correction. Right: the mass thickness of water after applying corrections.

9.5 NR series of the imbibition of H₂O with cold neutrons at ANTARES

A time series of neutron radiography measurements were made with a similar stone called IV23-STM at ANTARES. This was also a St. Margarethen porous limestone of cylindrical shape and same dimensions as IV17-STM. An L/D ratio of 400 was used and the exposure time for each image was 2s.

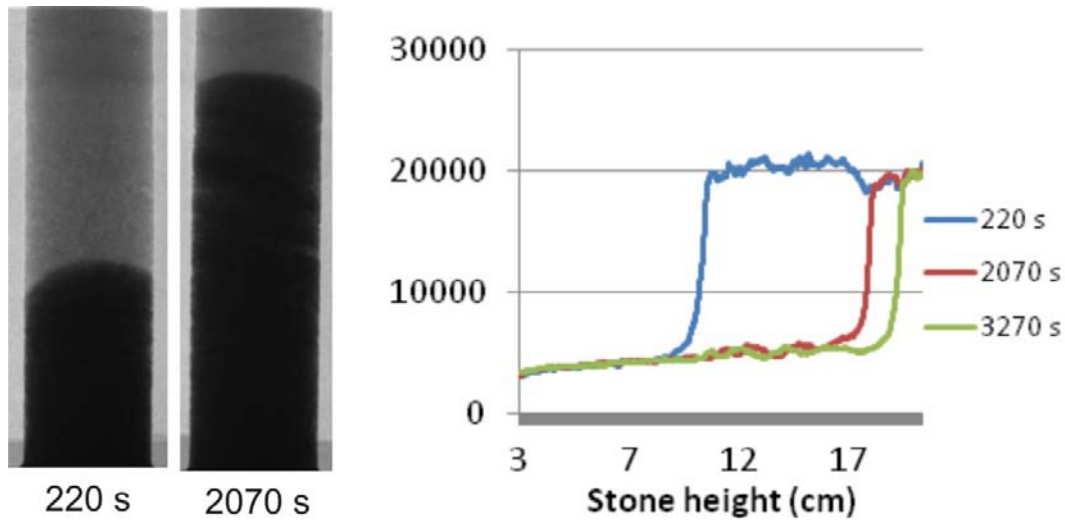


Figure 9-6: Left: the NR images after different intervals of time showing the imbibition of water. Right: Line profiles taken vertically along the height of the stone after different time intervals.

Figure 9-7 shows a quantitative analysis of the dynamic radiography made with a higher time resolution. Hence we have larger number of data points and a larger field of view. The analysis of the mass thickness of water has been done for an image in the series which was taken after about 9 min, the same time that the last image for the measurement of IV17 was taken. As in this measurement we had a bigger field of view so we can see that water has not yet penetrated to the upper part of the stone.

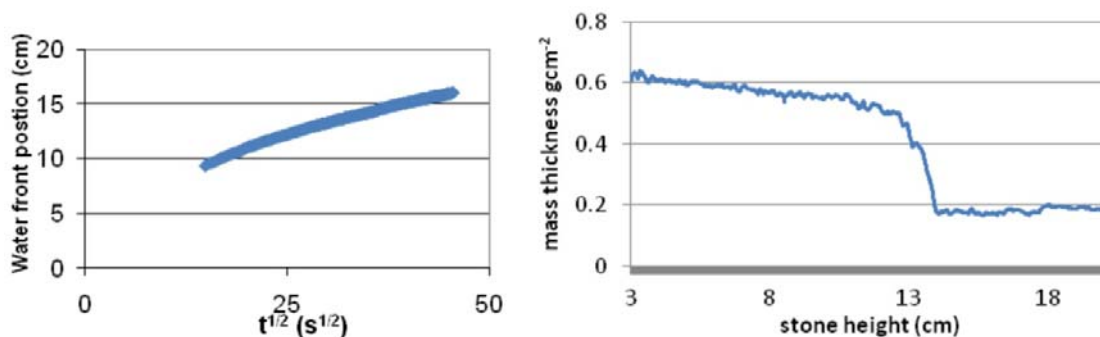


Figure 9-7: Left: a graph showing the position of the water front relative to the square root of time. Right: the mass thickness of water in the stone after about 9 min. The slope of the curve on the right gives the penetration coefficient of water which in this case is 0.2 cm/s^{1/2}.

Comparing the NR series measurement of two similar stones carried out at ATI and ANTARES. While making such a comparison it should be kept in mind that the parameters of the two measurements were different. In the case of the ANTARES measurement, the field of view was larger and the time series could be made for a height of about 19 cm and therefore for a longer duration of time. For the ATI measurement, the first image was obtained about 60 s after pouring water in the bath, while for the ANTARES measurement, the first image starts after about 220s. The time resolution at ANTARES is better than at ATI. At ATI, we got an average of one image per minute. At ANTARES, an average of 6 frames was obtained per

minute. Moreover the energy spectra of the two facilities were different. The spectra of the two facilities have been discussed in chapter 3. At ATI we have a thermal spectrum, while at ANTARES, there is a cold spectrum and a much higher flux. There was a higher sensitivity in the case of the ANTARES measurements. There is a difference of about 2 cm for the water front positions after similar time intervals. For the ANTARES measurement the water front is 2 cm more. A possible explanation could be that for that measurement, the stone was placed in a larger bath of water. The height of water in the bath was about 2 cm; the diameter of the bath was also larger. For ATI, the height of water in the bath was 0.9 cm. So for the ANTARES measurement, a larger part of the stone was immersed in water. The penetration coefficient determined from the ATI measurement is $0.35 \text{ cm/s}^{1/2}$ and that for the ANTARES measurement is $0.2 \text{ cm/s}^{1/2}$.

Such an analysis can be performed to find out the penetration coefficients of different strengtheners in different stones. The mass thickness of hydrogen or the mean density can be determined. This method can be used to analyze the NR measurements of textile fibers with relation to moisture transport with respect to temperature.

9.6 X-ray investigation

X-ray measurements were made to try to obtain some information about these studies with an alternative technique. X-ray tomography was made of different samples. A conical beam was used. RAYSCAN 250 XE (extended) was the name of the system that was used for these measurements. This is an industrial CT (computed tomography) system.

Figure 9-8 shows the X-ray CT of a dry St. Margarethen calcareous arenite. The resolution of the measurement was $90 \text{ }\mu\text{m}$. The source object distance was 34.5 cm and the source detector distance was about 154 cm. The voltage was 215 kV and the current was 330 μA . The number of projections was 720. The time for one CT was about 33 min.

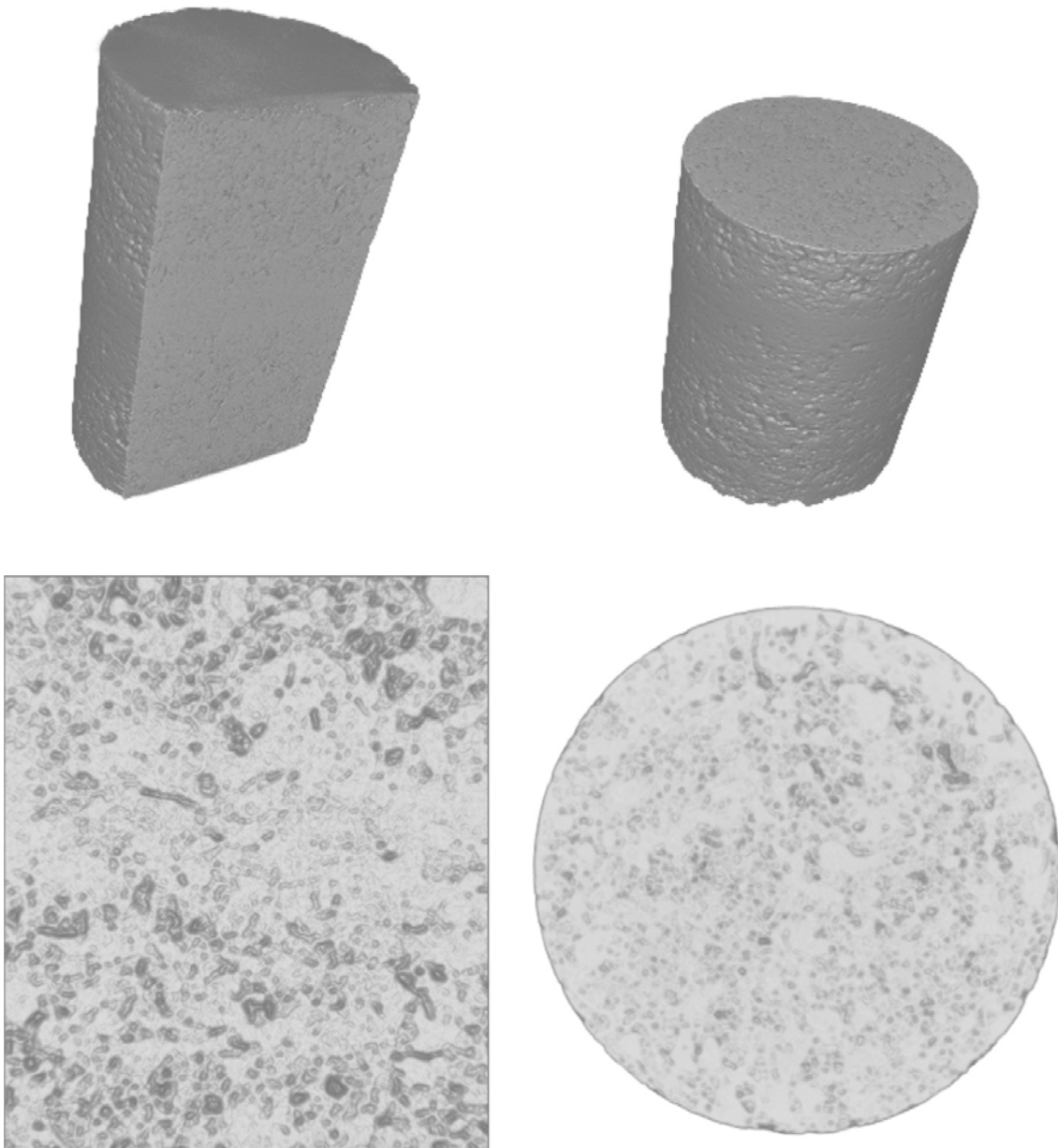


Figure 9-8: An X-ray CT of a calcareous arenite stone. Below, a front view of a vertical cut and a view of the horizontal cut of the stone.

Similar measurements were performed with a strengthened stone and a wet stone. But in that case the measurements were not successful. The strengthener in the stone could not be identified. With X-rays we expect beam hardening when there is water or hydrogen in the sample. We can only distinguish between two materials when the density difference is 5 to 10

%. In this case the difference is much less. Another dry stone, a weathered quartz arenite stone was measured; this stone has very fine homogeneous pores. We were not able to see these in the CT.

An attempt was made to make a time series of water penetrating into a stone. We saw that the penetration of water inside the stone could not be observed with this method as there wasn't enough contrast. There seemed to be no considerable difference between the first and the last image. The number of projections was 1350 which were made over a time of one hour. It was not possible to make dynamic studies of the imbibition of water in the stones.

We may conclude by saying that for dry samples, it is possible to use X-rays for visualizing their structure. The resolution in this case can be better than neutron radiography. For the case of hydrogen based studies, it is not possible to use X-rays for visualizing water or a consolidant inside a stone. For that case the neutron method is suitable. Hence we see that X-ray and neutron imaging are complementary techniques. Each radiation has advantages and disadvantages. Thus they should be used accordingly. For the studies performed in this thesis, neutrons were the most suitable.

10 SOME MORE APPLICATIONS

10.1 Measurement of porosity

A cooperation was started recently with the structural processes group, in the department of Geodynamics and Sedimentology. They are working on the modeling of natural fault systems. The aim was to use the method of neutron tomography to study grain sizes and distributions.

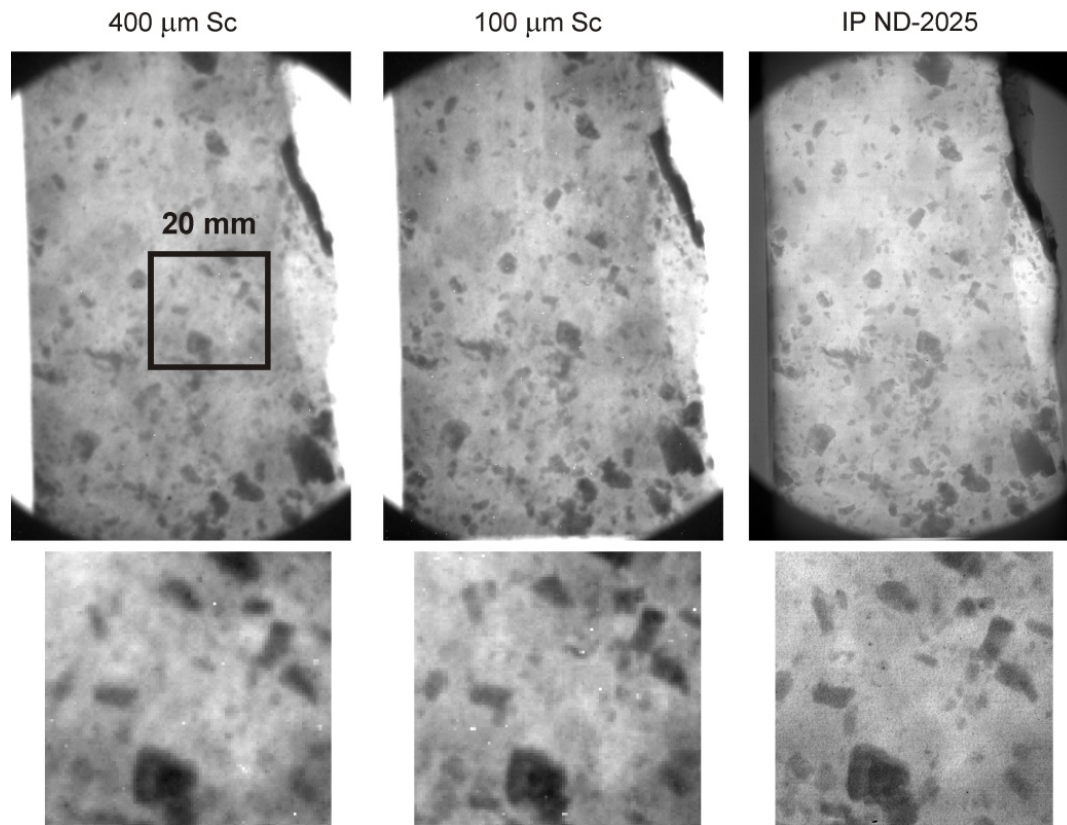


Figure 10-1: Neutron images of 35 mm thick feldspar reveal dark regions of boron (3.3%) in tourmaline, hydrogen in muscovite (mica), and spurious rare earth elements in garnet. The unprocessed images demonstrate the hierarchy of detector resolution, the best result with the NIP (right), which is also free of white spots as seen in the scintillator images (left and middle).

The features that were of interest were “Deformation Bands”. They form at an early stage after the deposition of the Sediment when it is still rather soft, so that no distinct fault surfaces are generated, but instead are characterized by a broad irregular zone of increased compaction and pore space reduction [Shipton, 2003; Draganits, 2005]. The idea was to treat

More applications

samples with some resin (e.g. ester or epoxy), to make the pore space well visible in the neutron tomography. This would then give the 3D distribution of reduced pore space, thus the 3D geometry of the deformation bands. Using this as input for 3D mechanical models, geologists can draw conclusions for the mechanical properties and stress conditions during formation of these structures. Good spatial resolution and high detection sensitivity for hydrogen and rare earth elements are the basis for these projects [Winkler, 2002; Solymar, 2003]

Some preliminary results have been presented. In Figure 10-1 parallel cut feldspar, with 35 mm thickness and two plane surfaces, was placed directly in front of the detector. Despite the large thickness, the NIP result is much better defined than the scintillator images. Also the gammas do not significantly affect the image quality, and a three centimeter lead block, chosen as additional gamma shield to the present 4 cm bismuth filter, yields no improvement Figure 10-2. This example also emphasizes the superiority of the neutron imaging plate in comparison with a conventional Gd-film detector using a 25 μm thick gadolinium foil as neutron converter and an x-ray film (Structurix D7).

More applications

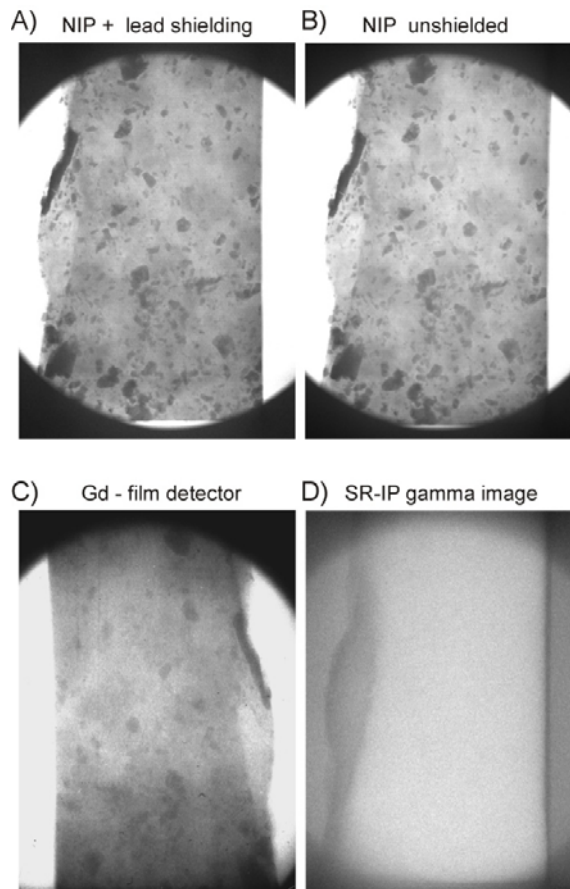


Figure 10-2: A) Imaging of Feldspar directly in front of the imaging plate with 3 cm lead for additional gamma shielding. B) Same sample without lead shielding, in both cases the transmission through the feldspar is 47 % on average. C) Despite the longer exposure time (30 min Gd converter x-ray film / 10 min NIP) the image gradation is much smaller in the film detector. D) The poor gamma image emphasizes the strengths of neutrons for the investigation of geological samples.

The tomography of the same feldspar with the new 100 μm scintillator plate yields a better resolution in comparison with the 400 μm detector but the measurement time has to be extended in order to accumulate comparable count numbers in the detector pixels

Figure 10-3. Typically, 200 projections are used yielding total measurement times of approx. 4 hours with the 400 μm scintillator and 11 hours with the 100 μm scintillator. On demand, the number of projections and measurement time can be extended over several days to exhaust the full dynamic range of the CCD chip. IDL (ITT Visual Information Solutions) and Octopus software (University Ghent, Belgium) is implemented for tomographic reconstruction, and VGStudio (Volume Graphics GmbH) for 3D rendering.

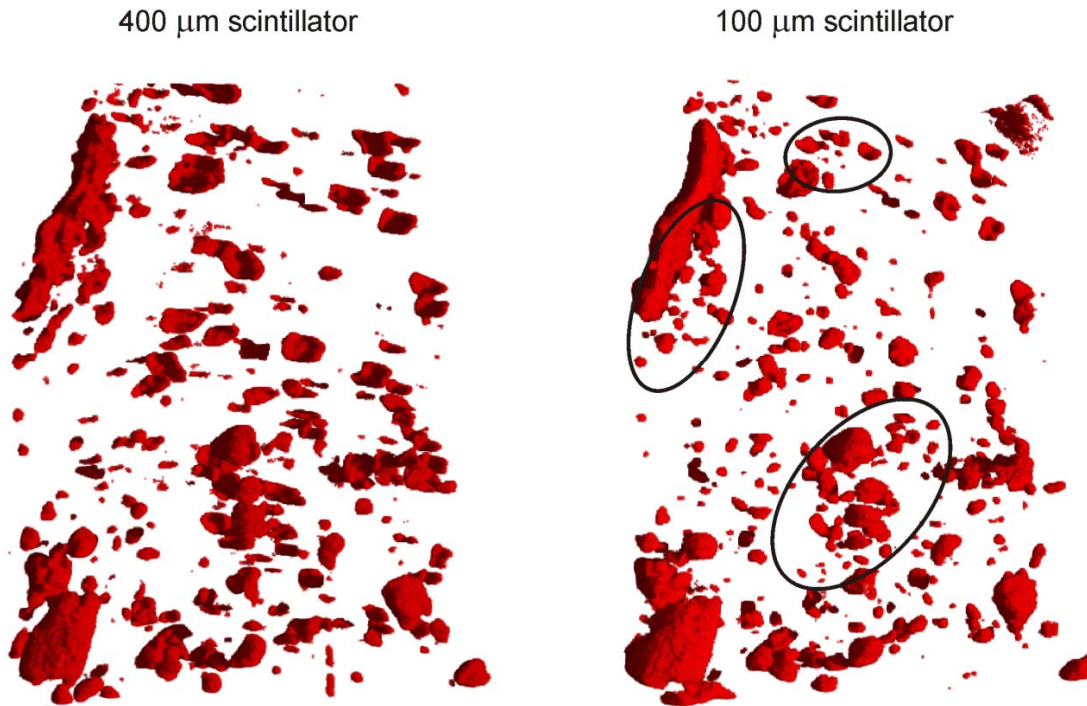


Figure 10-3: Tomography of feldspar.

The red regions show tourmaline, mica and garnet grains where hydrogen, boron and rare earth elements cause higher neutron attenuation. These grains have been colored red and then extracted from the stone. The higher resolution with the 100 μm scintillator enables a better distinction between different grains as highlighted in the right image. The 3D analysis yields 343 grains, a mean grain volume of 2.8 mm^3 , and a grain/stone volume (porosity) of 1.3 % in this sample.

Figure 10-4 shows neutron tomography of two St. Margarethen calcareous arenite samples. This measurement was made with the 400 μm Li-6 based scintillator with an exposure time of 40 s for each image. In Figure 10-4 c) the stone has been made transparent and the red segments represent the porosity. These were dry samples without any treatment. The red color represents regions of higher attenuation, which may be the humidity in the pores. This result shows that the two samples have different porosity distribution. The dark red region between the stone stones is the tape that was used to stick the two stones together.

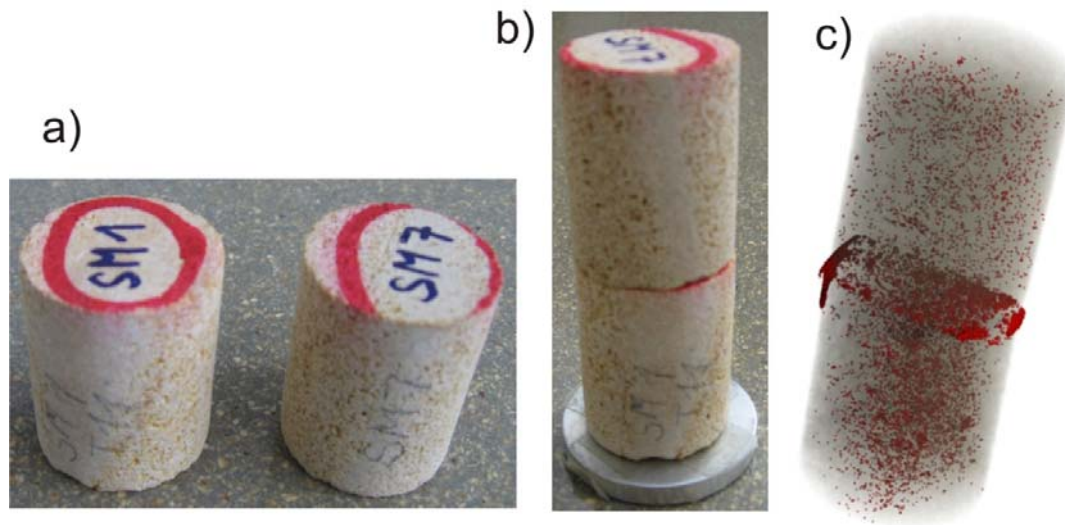


Figure 10-4: a) Two St. Margarethen calcareous arenite samples. b) For measurement, the samples were placed one on top of the other. c) A NT measurement of the stones.

Such measurements will be analyzed for the statistics of the pores, which is the number of pores, pore size, location, etc. This statistical data will then be used as an input for 3D mechanical models by geologists to draw conclusion for the mechanical properties and stress conditions during formation of these structures. This information is thus important for structural studies.

10.2 Boron alloyed steels

Boron being a strong absorber of neutrons is used for making boron alloyed steels which are used as a nuclear shielding. These steels manufactured by Böhler Bleche GmbH, Mürtzschlag in Austria, are used for shielding neutrons from radioactive waste. Examples are compact fuel racks for the intermediate storage of spent fuel elements. For such applications, these steels should have sufficient absorption in order to rule out criticality accidents.

At the neutron imaging facility NR II at ATI, a well defined thermalized neutron beam is available. This is close to the neutron field under realistic conditions when spent fuel rods are stored. In spite of the modest beam intensity, the Maxwellian energy distribution yields sufficient neutron transmission even through strong absorbing materials. Transmission

More applications

measurements of steel plates up to 2.5 cm thickness have been performed [Zawisky, 2004; Zawisky, 2004; Bastuerk, 2005]. Left over pieces are machined to steel sheets with identical thickness. These steel sheets having the same composition and each having a thickness of 0.137 cm can then be combined to stacks of different thicknesses as shown in figure 1. The minimum content boron is 1.88 weight percent and the fraction of the B-10 isotope amounts to 0.35 weight percent. The following expression was used to determine the transmission:

$$T = \frac{N_s - N_b}{N_o - N_b} \quad (10.1)$$

N represents the pixel counts and the subscripts s, b and o stand for the sample, open beam and background respectively. The transmission using equation (10.1) can be determined pixel wise for the scintillator measurements. However for the neutron radiography measurements made with the imaging plate, due to the reduced position reproducibility, the background has been averaged. The background has a significant effect on low transmission experiments when N_s approaches N_b . The background depends mainly on the intrinsic in the CCD camera and gammas in the imaging plate [Haga, 1999; Zawisky, 2008].



Figure 10-5: Neutron radiography measurements of different thicknesses of the boron steel plates were made using the scintillator detector. The distance between the detector and the sample was also varied.

More applications

After the upgrading mentioned in chapter 4, the neutron imaging plate detector was used to investigate the steel homogeneity. For this purpose the BAS-5000 readout scanner was used with 25 μm nominal resolution. The boron steel plates were placed directly in front of the NIP with 40 μm vertical and 60 μm horizontal effective resolution. The intrinsic granular micro-structure complicates the analysis of absorber inhomogeneities [Zawisky, 2008]. The plate has to be placed in exactly the same position for open beam correction, equation (10.1), to correct for this granularity. For a pixel scale of 25 μm , this is a challenging task. This was achieved by overlapping three or more dark pixel areas which appear in contrast enhanced sample and open beam images. Besides the intrinsic NIP artifacts, no significant boron inhomogeneities were found in the steel plate. The steel homogeneities and the NIP artifacts are expected on a similar scale, thus the NIP in the present setup is not optimal for such investigations.

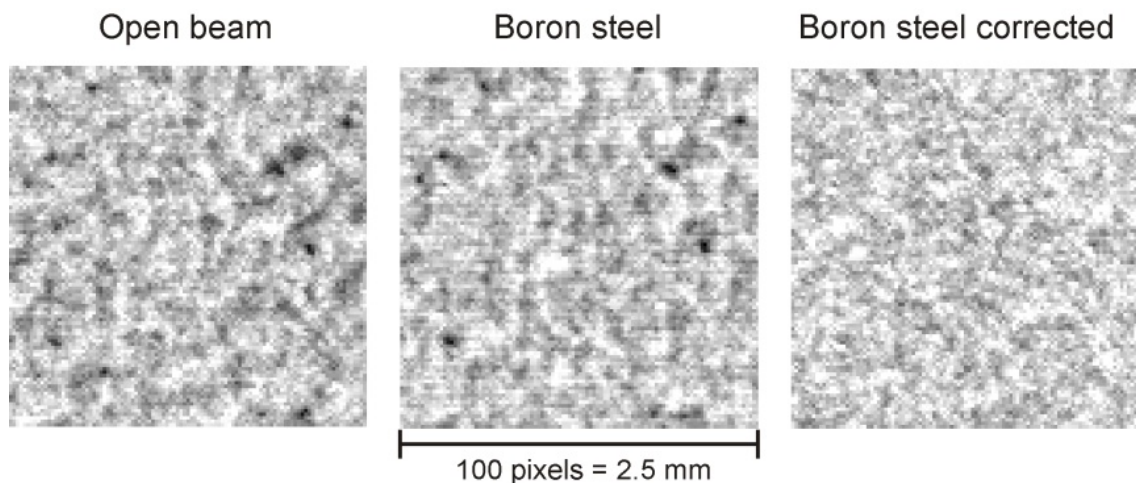


Figure 10-6: NIP images of the steel inspection. Left: the intrinsic granular structure of the NIP. Middle: Transmission image of the boron alloyed steel superposed by the granularity of the NIP. Right: after open beam correction, no significant inhomogeneities remained.

The neutron imaging plate inspection of the boron steel is shown in Figure 10-6. This measurement has a 25 μm nominal resolution and 40 μm optical resolution. For this investigation,

$$\frac{I_{max} - I_{min}}{I_{max} + I_{min}} \approx 10\% \quad (10.2)$$

More applications

The contrast of the images in Figure 10-6 has been enhanced for presentation only. After performing measurements with different detectors, it can be concluded that the scintillation detector is suitable for low transmission experiments as compared to the imaging plate detector. The scintillator is suitable due to superior reproducibility, easier open-beam and background correction and negligible gamma background. So far all transmission measurements have revealed enhanced neutron transmission.

11 CONCLUSION AND OUTLOOK

The experimental setup at the neutron imaging facility NR II at The Atomic Institute (ATI) has been upgraded. The spatial resolution has now improved with the help of a new scintillation detector and an imaging plate detector. With the upgrading, high resolution imaging beyond the resolution of 340 μm with the old scintillator is now possible. We have a best resolution of 150 μm for the 100 μm thin scintillator. For the neutron imaging plate an effective resolution of 40 μm can be achieved. Imaging plates at our setup are being used for static measurements.

It is now possible to perform longer neutron tomography measurements because of the fixed nitrogen filling installation. Previously the CCD camera could only be filled once for a tomography measurement and the cooling lasted for a maximum time of 3 to 4 hours. This was a limitation. In order to exploit the full dynamic range, an arrangement has been made for a fixed nitrogen filling of the CCD camera. With the help of this arrangement, liquid nitrogen can be filled during measurement. Thus it is now possible to increase the exposure time and the total number of projections to get tomography measurements with good resolution and higher sensitivity. Longer measurements can now be made for important experiments where higher sensitivity and resolution are required. Thinner scintillators can now be tested for selected applications because of the automatic filling station. Thinner scintillators may be useful for static measurements. Thus it is now possible to perform neutron imaging with a higher resolution and better sensitivity at a low power research reactor. It has been shown that high spatial resolution down to 50 μm regime is practicable with weak intensities of 10^5 n/cm²s.

The unique properties of the neutron interaction with matter and the improved instrumental setup have been utilized for promising applications in various fields. The new applications investigated were ideally suited to neutrons. Elements having small atomic numbers like hydrogen do not give sufficient contrast in X-ray radiography. On the other hand neutrons have a high sensitivity for hydrogen, a high cross-section. Different projects based on the hydrogen sensitivity of this method have been successfully carried out. Qualitative investigation has provided valuable results. Quantitative studies have also been performed to study the transport of moisture in building materials and textile fibers. Neutron imaging has been employed to study the penetration and distribution of consolidants in stones for the

Conclusion and Outlook

purpose of conservation and restoration. The distribution of moisture in different textiles fibers has been studied using neutron radiography. Neutron radiography and tomography methods have been used successfully to get 2D and 3D information about these samples. These techniques have the advantage of being non-destructive.

The techniques of neutron imaging have been applied in the nuclear industry. The non-destructive studies of radioactive isotopic neutron sources and transmission studies of boron alloyed steel used for shielding nuclear waste have been done. X-rays do not possess high penetration ability into materials having high atomic number. Consequently neutron radiography and neutron tomography are an important tool for studies of radioactive materials. The complementary properties of neutrons and X-rays can be exploited for non-destructive evaluation of materials. The samples studied were ideally suited to neutrons. The work with the neutron sources can be further extended by using the transfer technique employing the imaging plate.

Neutrons are able to distinguish between different isotopes; hydrogen and deuterium are a good example. Further experiments can be performed using H₂O and D₂O. Light water and heavy water give a very good contrast for neutron radiography. This can be useful for investigating moisture transport in moist samples. Important applications could be the investigation of diffusion of humidity in textile fibers, building materials and fuel cells.

Systematic studies on hydrogen quantification are needed in order to validate the new correction software at this instrumental setup. Analysis of the distortions in the quantitative information at the experimental setup at NR II can be studied in detail. Quantitative study of moisture transport is an interesting topic with various important applications.

Further measurements may be performed to study the structural changes in geological samples based on their porosity. Deformation bands in rocks can be visualized and the statistical data of the pores can be obtained three dimensionally. This data can then be entered into mechanical models by geologists to draw conclusions for the mechanical properties and stress conditions during formation of these structures. Good spatial resolution and high detection sensitivity for hydrogen and rare earth elements are the basis for these projects

12 APPENDIX I

12.1 NR investigations of weak, fair and strong absorbers

In order to study the behavior of weak, fair and strong absorbers, NR measurements were made using plates of uniform thickness from aluminum, copper, steel and boron alloyed steel. These materials were chosen due to their varying cross-sections for neutrons. Aluminum is almost transparent for neutrons, copper and steel are fair absorbers, whereas boron alloyed steel as discussed in chapter 11 is a strong absorber [Zawisky, 2004; Bastuerk, 2005]. Radiograph measurements were made using the Li-6 based 400 μm scintillator coupled to a CCD camera. NR measurements were made for different thicknesses by changing the number of plates. The description of the measurements performed has been given in the Table 12-1:

Table 12-1: Sample description of the different materials studied by NR

Material	No. of plates	Thickness of each plate (cm)	Exposure time (s)
Aluminum	20	0.3	35
Copper	10	0.3	35
Steel	20	0.14	35
Boron alloyed steel	15	0.137	60

After performing the measurements, Image Pro software was used to process the images. The following expression was used to determine the transmission:

$$T = \frac{N_s - N_b}{N_o - N_b} \quad (12.1)$$

N represents the pixel counts and the subscripts s; b and o stand for the sample, open beam and background respectively. The transmission using equation (12.1) can be determined pixel wise for the scintillator measurements. The transmission was evaluated relative to thickness. Using the transmission values, the attenuation coefficient Σ was determined. Figure

12-1 shows the effective macroscopic cross-section of the different materials plotted versus the thickness.

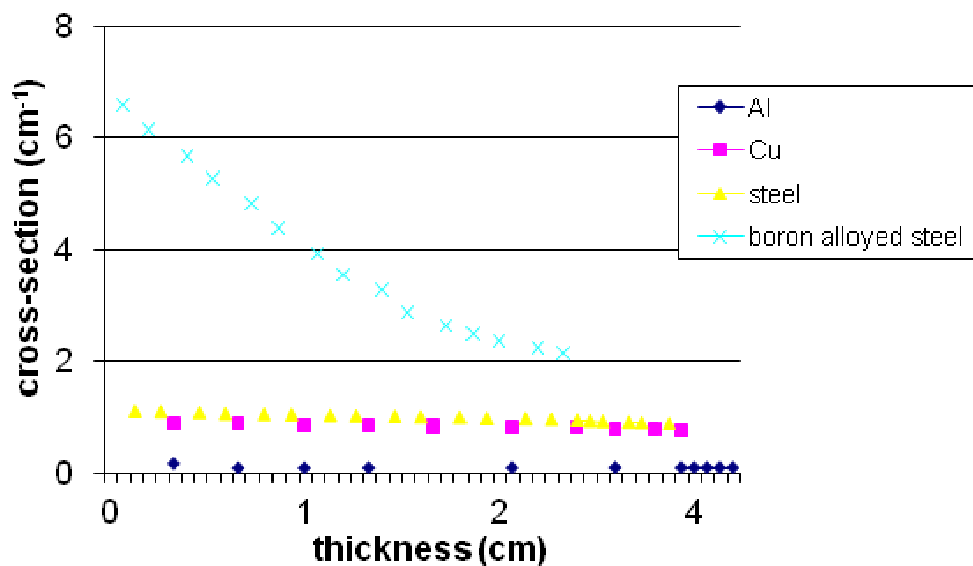


Figure 12-1: A graph showing the effective attenuation coefficient or macroscopic cross-section of the different materials relative to thickness.

Comparing the experimental values in Figure 12-1 with the tabulated values given in Table 12-2, it is seen that the deviation of aluminum is negligible, while the fair absorbers, steel and copper show a slight deviation but boron alloyed steel shows a significant deviation. The enhanced transmission of boron alloyed steel has been discussed in chapter 11. One of the important reasons for this deviation is the beam hardening effect [Zawisky, 2004]. The boron inhomogeneity in the steel is being investigated.

Table 12-2: Tabulated values of the attenuation coefficients for the materials

Material	Σ (cm ⁻¹)
Aluminum	0.1
Copper	0.98
Steel	1.16
Boron alloyed steel	7.3

12.2 Labview program for the shutter

The shutter of the NR II beam line was operated with the help of a switch. In order to make its operation comfortable, a code was developed in the Labview environment to control the shutter from the instrument computer.

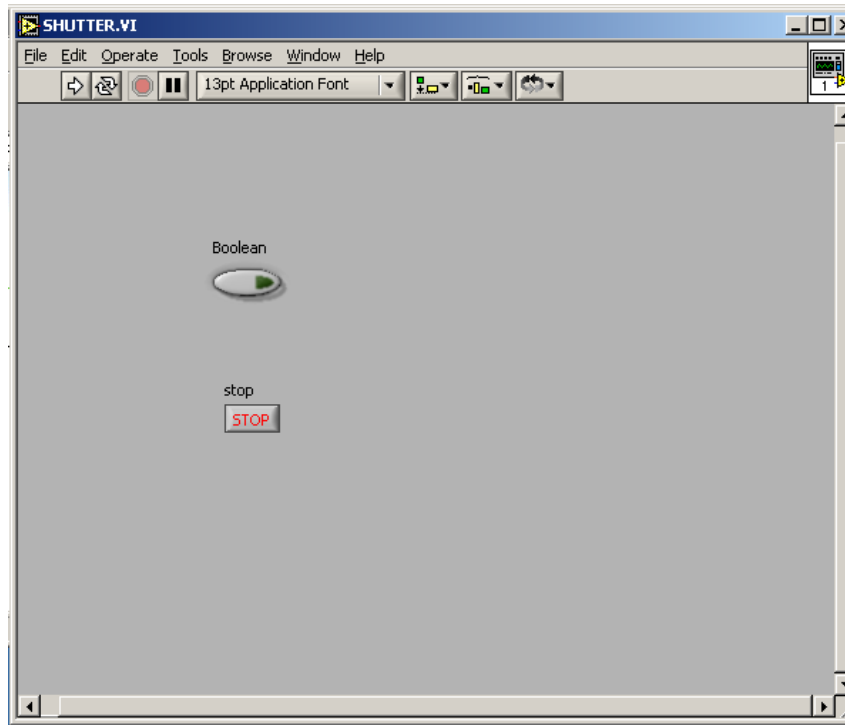


Figure 12-2: the window used to control the shutter from the instrument computer

The shutter of the NR II facility is controlled by a Labview program. The electronics of the shutter have a parallel port and so the program is based on a parallel port routine. The Figure 12-3 shows the code which is executed through a runtime engine.

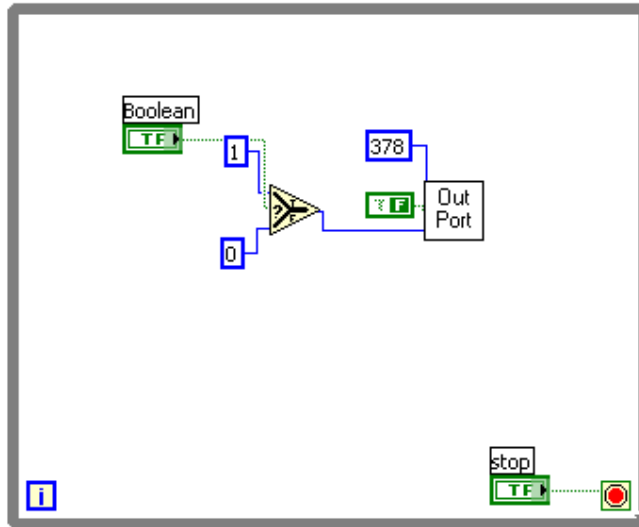


Figure 12-3: The code for opening and closing the shutter.

12.3 Gold chain

There was a discussion in the institute about a gold chain that seemed too light and its authenticity was being questioned. It was suggested that neutron radiography could help. With the help of neutron radiography which was made with the imaging plate detector, it was clearly visible that the design of the chain was such that it was hollow from within. Thus the weight was less than expected.

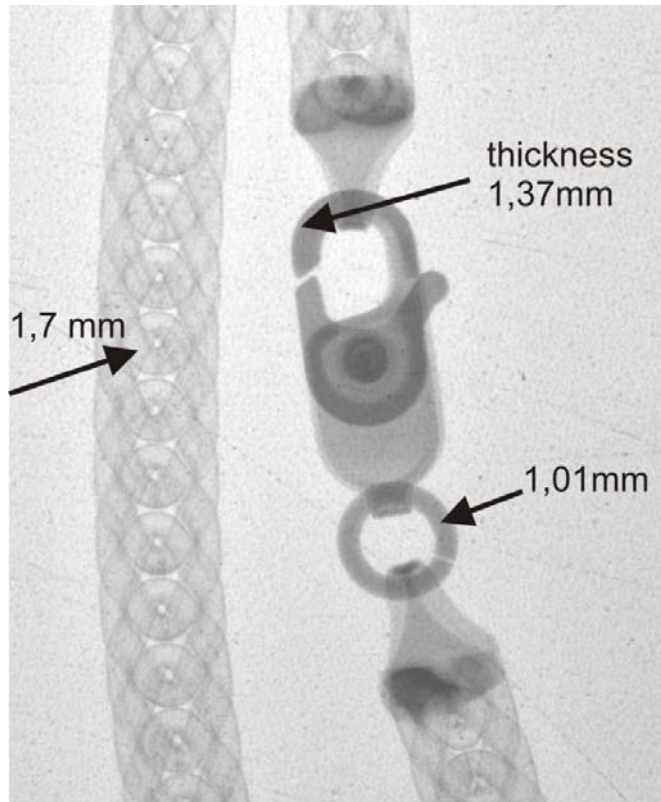


Figure 12-4: Neutron radiography of a gold chain showing the hollow design. The thickness here refers to the distance the neutrons have to travel through.

The dimensions shown in Figure 12-4 were measured with a digital micrometer screw gauge having an accuracy of 10mm.

13 APPENDIX II – NT OF RESTORED ORIGINAL SAMPLES

Conservation and restoration of important historical buildings and monuments is very challenging. Among the different techniques that are applied, the use of chemical consolidant agents is also employed. In order to ensure a successful restoration, continuous monitoring and assessment has to be performed. Different techniques are used for the assessment such as ultra sonic measurements, drilling force method, etc [Price, 1996; Rodrigues, 2001; Fleischer, 2005]. Neutron imaging is a non-destructive technique that is very useful in this regard. Neutron radiography gives 2D information about the depth of penetration. Neutron tomography gives a complete 3D mapping of the consolidant inside the sample [Hameed, 2006; Hameed, 2008]. Original samples were obtained from historical buildings and monuments. These samples had been restored. The history of the samples had been carefully documented. A red mark on each of these samples as shown in the photographs represents the outer surface. An assessment of the restoration was carried out using the method of neutron tomography. Results of these measurements have been presented in the sections below.

13.1 Sample 1

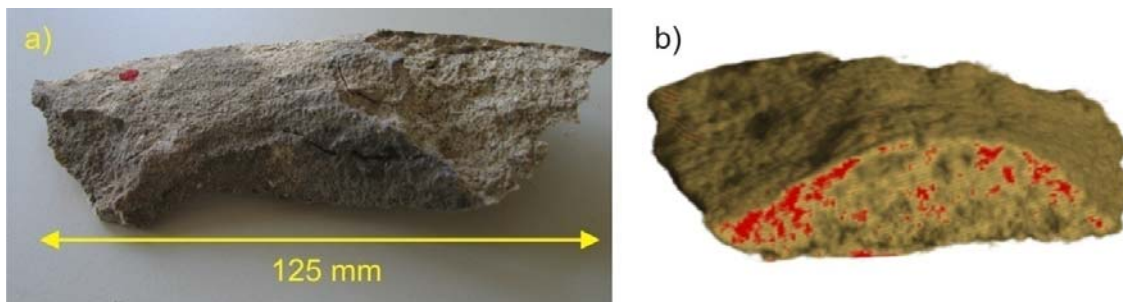


Figure 13-1: a) Sample photograph. The outer surface is represented by a red dot. b) NT of the sample where the red segments represent the consolidant. A vertical cut of the stone has been shown.

The information given with the sample is as follows:

Internal no.: W9578

Source: From the sculpture of a female goddess, Baroque sculpture

Appendix

Treatment:	With 100 OH (ethyl silicate) (which is the same as Wacker OH100)
Method:	Bath method. Which means the whole statue was dipped in a bath containing the strengthener.
Expected:	Complete penetration is expected
Time of treatment:	13-04-07 (fresh consolidation)
Age of sample:	18 th century
Type of stone:	Calcareous arenite from Stotzing. Maybe the stones were exchanged with the original ones which were similar to sample 3, i.e. calcareous arenite from Zogelsdorf.
Weight:	72.476g

Neutron Tomography measurement was performed about three and a half months after consolidation. The Li-6 based scintillator having a thickness of 100 μm was used and the exposure time was 120 s per projection. After reconstruction, Figure 13-1b) shows the highly attenuating regions in red color. In this case the high attenuation is due to the hydrogen content of the strengthener. From the figure it can be deduced that the consolidant has penetrated the stone as expected.

13.2 Sample 2

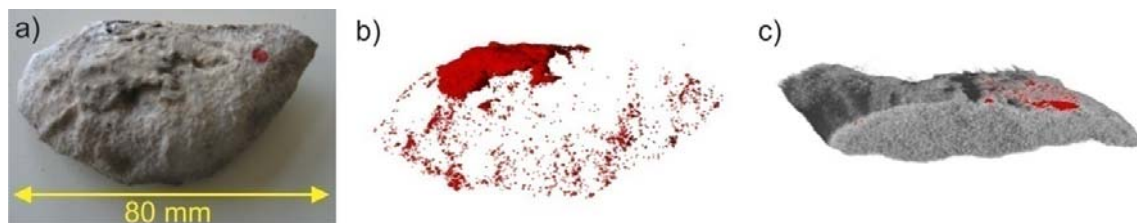


Figure 13-2: a) Photograph of the sample. b) NT of the sample. The stone has been made transparent to reveal the highly attenuating regions.

Appendix

Source:	Baroque sculpture of Hercules from Burgenland
Treatment:	OH100 (this is the same as 100 OH, i.e. ethyl silicate) in a bath. (Remember that Remmers 100 is different)
Method:	Bath method
Expected:	Complete penetration expected
Time of treatment:	December 2006
Age of sample:	1758
Type of stone:	calcareous arenite from (Au/Leithagebirge)
Weight :	46.820g

The big red region on the surface of the stone in Figure 13-2 is gypsum. Gypsum contains hydrogen and so it is very prominent in the tomographic reconstruction. Gypsum hindered the imbibition of the consolidant. The surface of the stone was probably too dense for the strengthener to penetrate. This is usually a problem in conservation. A thin section analysis of this sample is recommended.

13.3 Sample 3

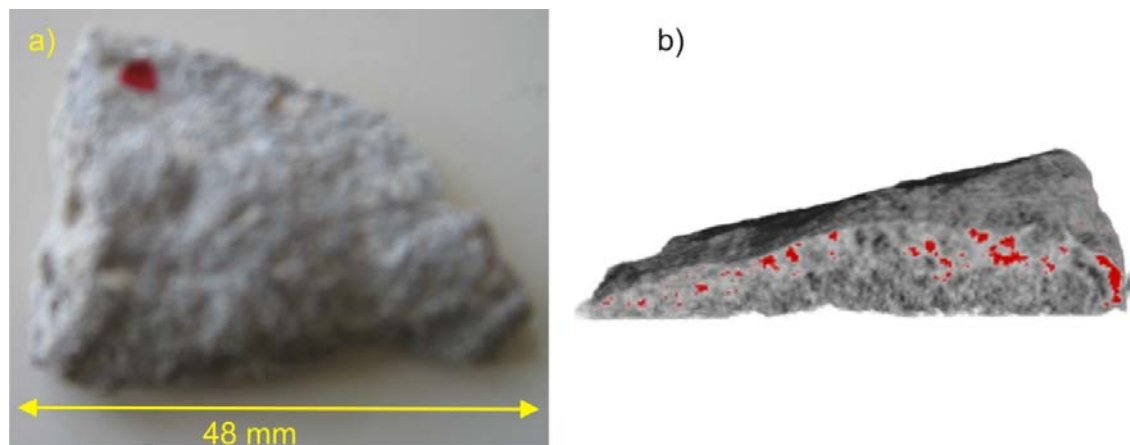


Figure 13-3: a) Photograph of the sample. b) NT showing the consolidant in red color.

Appendix

Source:	Similar to sample 1
Treatment:	Wacker OH (different from OH100, (Wacker OH is silica ester without silicon resin - hydrophobic)
Method:	floating, that is the strengthener was poured on it.
Expected:	2 -3 mm penetration expected
Time of treatment:	1996
Type of stone:	Calcareous arenite from Zogelsdorf
Weight :	10.960g

A neutron tomographic reconstruction has been shown in Figure 13-3 b. The red segments represent the stone consolidant. The NT result agrees with the expected penetration of the strengthener. It may be concluded that the restoration was successful and the desired depth of penetration was achieved.

13.4 Sample 4

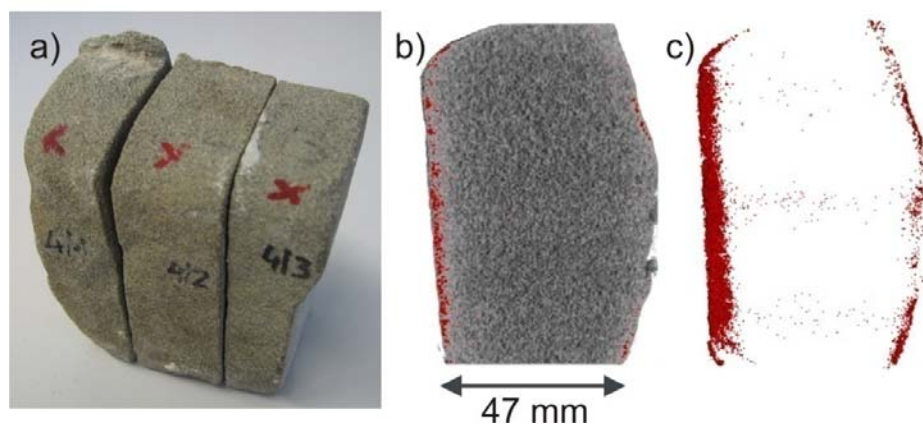


Figure 13-4: a) Photograph of the sample. b) A vertical cut of the reconstructed sample revealing the consolidant in red color. c) The stone has been made transparent to show the strengthener.

Appendix

Source:	Quartz sandstone also called St. Margarethen, this stone was used in the west of Austria for a Gothic window.
Treatment:	Tried by ethyl silicate – Wacker OH in 1992
Method:	floated twice
Expected:	5 – 10 mm
Time of treatment:	1992
Age of sample:	14 th - 15th century
Type of stone:	Quartz sandstone from Vorarlberg (Molassezone) also called St. Margarethen.
Weight :	572.824g

This was a large sample hence it has been cut into three pieces shown in the photograph Figure 13-4. The consolidant has been represented by red color in the tomographic reconstruction. Red segments are clearly visible on the surface which agrees with the prediction that the penetration of the strengthener is a few millimetres deep on the outer surface.

13.5 Sample 5

Source:	Monastery in Salzburg, from the facade
Treatment:	Ethyl silicate (another concentration – silical ester), Remmers 300, gel is different
Method:	Floated twice
Expected:	1 cm to 2cm of penetration
Time of treatment:	Smells fresh - 2007
Age of sample:	18 th century

Appendix

Type of stone: Quartz sandstone

Weight: 277.130g

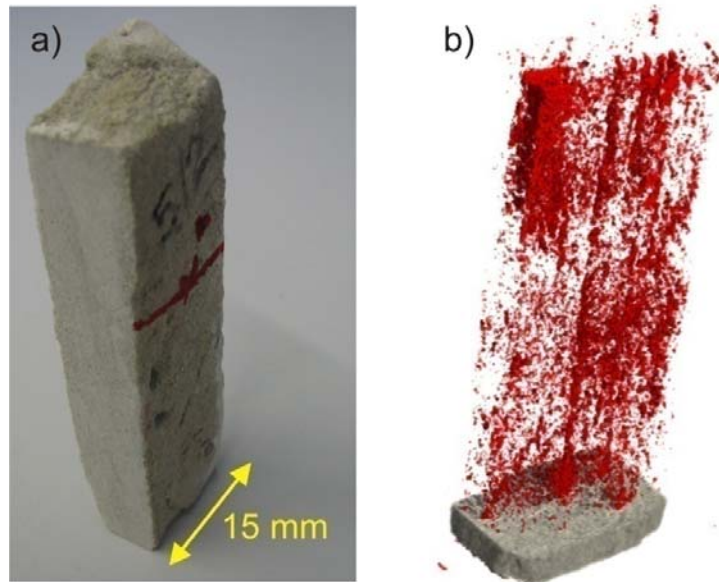


Figure 13-5: a) Photograph of the sample. b) The highly attenuating region shown in red color has been extracted from the reconstructed 3D rendering.

This was a large sample, thus it was cut into three parts to get an appropriate size for measurement according to our beam size. This sample is interesting because of its shape. It has two holes in it. After the tomographic 3D rendering, with VG Studio software, the high attenuating regions represented by red color were extracted. The resulting image is shown in Figure 13-5. The consolidants have reached the expected depth but are not uniformly distributed.

List of abbreviations

ANTARES	Advanced Neutron Tomography and Radiography Experimental Setup
ATI	Atomic Institute
BSE	back scattered detector
BSS	Bonner sphere spectroscopy
CCD	charge coupled device
CLY	lyocell
CT	computed tomography
Dpi	dots per inch
ESF	edge spread function
Etc	et cetera
FB	filtered backprojection
FRM	Forschungs Reaktor Muenchen
FWHM	full width half maximum
IDL	interactive data language
ISNR	International society for neutron radiography
LSF	line spread function
MCNP	Monte Carlo Neutron Particle Transport
Min	minute(s)
NAA	neutron activation analysis
NIP	neutron imaging plate
No.	number
NR	Neutron radiography
NT	Neutron tomography

List of abbreviations

PES	polyester
PSI	Paul Scherer Institute
PSL	Photo stimulated luminescence
2D	2 dimensional
3D	3 dimensional
ND&M	Neutron detector and monitor
ILL	Institute Lau Langevin
QE	quantum efficiency
QNI	quantitative neutron imaging
SE	secondary electron detector
SEM	scanning electron microscopy
TRIGA	Training, Research, Isotopes General Atomics
TU	Technical University
TUWIEN	Vienna University of Technology
USA	United States of America
USANS	ultra small angle neutron scattering

List of Figures

FIGURE 2-1: PRINCIPAL COMPONENTS OF A NEUTRON RADIOGRAPHY SYSTEM [DOMANUS, 1992].	15
FIGURE 2-2: ILLUSTRATION SHOWING THE ASSOCIATION OF VARIOUS RADIATION FLUX QUANTITIES WITH FUNCTIONAL PLANES AND SYSTEM COMPONENTS [DOMANUS, 1992; MISHRA, 2005].	16
FIGURE 2-3: UTILIZATION OF THE TRANSMISSION SIGNAL FOR THE TOMOGRAPHIC RECONSTRUCTION OF THE CROSS-SECTION $\Sigma(X, Y, Z)$ [ZAWISKY].	18
FIGURE 2-4: PRINCIPLE OF TOMOGRAPHIC PROJECTION	19
FIGURE 2-5: TOMOGRAPHIC RECONSTRUCTION WITH FILTERED BACKPROJECTION: A) CALCULATION OF THE PROJECTION DATA. B) +C) EACH PROJECTION DEFINES A LINE IN FOURIER SPACE. D) IDEAL OCCUPATION OF THE FOURIER SPACE IN THE LIMIT OF A LARGE NUMBER OF PROJECTIONS. E) THE HIGH-FREQUENCY PART FROM THE BACKPROJECTION IS AMPLIFIED.	21
FIGURE 3-1: <i>THE NEUTRON BEAM LINES AT THE TRIGA MARK II RESEARCH REACTOR.</i>	23
FIGURE 3-2: <i>NR FACILITIES AT TRIGA MARK II RESEARCH REACTOR.</i>	24
FIGURE 3-3: <i>THE MAXWELLIAN DISTRIBUTIONS OF NEUTRON FLUENCE AND DENSITY OF NR II.</i>	26
FIGURE 3-4: <i>UNFOLDED AND FITTED NEUTRON SPECTRA AT THE THERMAL COLUMN OF THE TRIGA MARK II RESEARCH REACTOR.</i>	27
FIGURE 3-5: FLOOR PLAN OF THE NR II STATION AT ATI.	28
FIGURE 3-6: <i>THE COMPOSITION OF THE FIRST PART OF COLLIMATOR AT NR II FACILITY.</i>	29
FIGURE 3-7: <i>A SCHEMATIC DIAGRAM OF THE DIGITAL DETECTION SYSTEM AT NR II – ATI FACILITY IN VIENNA.</i>	31
FIGURE 3-8: SCHEMATIC OVERVIEW OF ANTARES FACILITY.	32
FIGURE 3-9: SETUP OF THE ANTARES FACILITY	33
FIGURE 3-10: SPECTRAL NEUTRON FLUX DENSITY IN THE ENERGY REGION BETWEEN 1MEV AND 0.1EV	35
FIGURE 3-11: SPECTRAL NEUTRON FLUX DENSITY IN THE ENERGY REGION BETWEEN 0.1MEV AND 1MEV	35
FIGURE 4-1: LEFT: THE 100 μM THIN-PLATE SCINTILLATOR WITH 10 X 15 CM^2 DETECTION AREA TOGETHER WITH THE OLD 400 μM SCINTILLATOR; THE 25 X 20 CM^2 IMAGING PLATE INSERTING IN THE BAS-5000 SCANNER. RIGHT: SAMPLE AREA OF THE UPGRADED INSTRUMENT.	38
FIGURE 4-2: ESF MEASUREMENTS WITH DIFFERENT LENSES. THE PIXEL SIZE DENOTES THE OPTICAL RESOLUTION OF THE LENSES, LEFT $F = 105 \text{ MM}$, RIGHT $F = 180 \text{ MM}$. THE FIT YIELDS $\lambda = 1.1(1)$ AND $145 \pm 13 \mu\text{M}$ RESOLUTION IN THE RIGHT PLOT.	40
FIGURE 4-3: INHOMOGENEITIES IN THE OPEN BEAM PROFILE.	41
FIGURE 4-4: COMPARISON OF THE DARK NOISE (LEFT, CAMERA-SHUTTER CLOSED) AND GAMMA NOISE (RIGHT, BEAM-SHUTTER CLOSED). THE DOMINATING DARK NOISE INCREASES WITH $N_{\text{Dark}} = 293 + 0.4 \times \text{time}(s)$ AND THE GAMMA BACKGROUND WITH $N_{\text{Gamma}} = 0.23 \times \text{time}(s)$	42
FIGURE 4-5 LINEARITY OF THE NIP COUNT NUMBERS AT 25 μM PIXEL RESOLUTION.	43
FIGURE 4-6 OPEN BEAM INTENSITY VARIATIONS AND NIP ARTIFACTS.	44

List of Figures

FIGURE 4-7: ESF - RESOLUTIONS WITH THE NIP; THE TICKS IN THE NEUTRON IMAGES MARK THE POSITIONS OF THE EDGE PROFILES. THE FITS YIELD $\lambda = 0.8(2) \Rightarrow 60 \pm 15 \mu\text{m}$ HORIZONTAL, AND $\lambda = 1.25(20) \Rightarrow 40 \pm 7 \mu\text{m}$ VERTICAL RESOLUTION.	45
FIGURE 4-8: REPRODUCIBILITY OF NIP INTENSITIES BY REPEATING ALWAYS THE IDENTICAL MEASUREMENT PROCEDURE: 10 MIN EXPOSURE \rightarrow WAITING TIME \rightarrow SCANNING \rightarrow 30 MIN ERASING TIME.....	46
FIGURE 4-9: IMAGING OF THE PSI GD TEST MASK WITH THE NIP. A) THE FINE GRID LINES WITH 50 μm LINE WIDTH ARE CLEARLY VISIBLE IN THE SQUARE. B) SIEMENS STAR WITH RADIAL MARKERS AT 500, 400, 300, 200, 100, 50 μm LINE PAIR RESOLUTION. C) THE VISIBILITY OF THE PERIODIC SPOKES BECOMES BLURRED BETWEEN 100 AND 50 μm RESOLUTION.	46
FIGURE 4-10: NITROGEN FILLING FOR COOLING THE CCD CAMERA.....	47
FIGURE 5-1. NEUTRON ATTENUATION IN TWO ST. MARGARETHEN DURING STRENGTHENING: 1A: HARD, 1B: SOFT [HAMEED, 2006].....	55
FIGURE 5-2. FRESHLY DRILLED CORES FROM ONE BLOCK OF SOFT MANNERSDORF CALCARENITE. THE STONES WERE PROCESSED IN A SOAKING BATH OF APPROX. 7 MM DEPTH. IRRIGATION AND CONSOLIDATION WERE APPLIED ON THE UNTREATED DRY STONES. THE WATER-REPELLENT TREATMENT WAS APPLIED SUBSEQUENT TO THE CONSOLIDATION [HAMEED, 2006].	56
FIGURE 5-3. TOMOGRAPHIC IMAGES OF THREE FRESHLY CUT AND CONSOLIDATED ST. MARGARETHEN LIMESTONES [HAMEED, 2006]: A) 4 DAYS, B) 9 DAYS, C) 11 DAYS AFTER SPRAYING; RED AND BRIGHT REGIONS SHOW THE STRENGTHENER.	57
FIGURE 5-4: SAMPLE F2 (LEFT) WAS DRILLED FROM THE WEATHER-EXPOSED SOUTHERN TOWER, EASTSIDE. F3 (RIGHT) FROM THE WEATHER-EXPOSED SOUTHERN HEIDEN-TOWER. THESE AREAS HAVE BEEN TREATED WITH DIFFERENT RESTORATION TECHNIQUES SEVERAL YEARS AGO [HAMEED, 2006].....	59
FIGURE 5-5. THREE CORES DRILLED OUT FROM ST. STEPHAN'S FACADE. THE DIAMETER IS APPROX. 25 MM AND THE ARROWS MARK THE WEATHER-EXPOSED OUTER SURFACE [HAMEED, 2006].	59
FIGURE 5-6. TOMOGRAPHY OF THREE CORES FROM WEATHER-EXPOSED AREAS OF THE CATHEDRAL'S FACADE, SEVERAL YEARS AFTER RESTORATION. SURPRISINGLY, THE CONSOLIDANT WAS NOT VISIBLE AT THE OUTER REGIONS. IN THE COLORED REGIONS THE NEUTRON ATTENUATION IS INCREASED BY HIGHER DENSITY AND/OR HIGHER CONTENT OF HYDROGEN AND IRON. IN THE BOTTOM ROW THE VOXELS OF HIGHER DENSITY AND/OR HYDROGEN CONTENT ARE EXTRACTED FROM THE BULK IN ORDER TO GET A 3D IMPRESSION OF THESE REGIONS OF INTEREST. IN THE UNTREATED CORE F4 A SURFACE CRUST IS REVEALED AT THE WEATHER-EXPOSED SURFACE (RED LAYER) [HAMEED, 2006].	60
FIGURE 5-7. TESTING THE WATER-RESISTANCE OF TREATED STONES FROM THE CATHEDRAL'S FACADE. ONLY IN F3 MOISTURE UPTAKE WAS PREVENTED EFFECTIVELY, WHILE IN F1, F2 THE WATER-UPTAKE WAS RATHER FAST [HAMEED, 2006].	61
FIGURE 5-8 ACOUSTIC MEASUREMENTS ALONG THE VERTICAL SAMPLE AXIS. HIGHER VELOCITIES MARK REGIONS OF HIGHER DENSITY.	62

List of Figures

- FIGURE 5-9 LEFT: PERMEABILITY MEASUREMENT. THE STONES ARE HERMETICALLY SEALED IN VESSELS COMPLETELY FILLED WITH WATER. THEN THE EVAPORATION THROUGH THE OUTER SURFACE WAS MEASURED OVER A TIME PERIOD OF 21 HOURS. RIGHT: MEASUREMENT OF DRYING RATES OF THE WET STONES IN SAME CONFIGURATION BUT EMPTY VESSELS. 62
- FIGURE 5-10 OPTICAL SCANS OF THIN-SECTIONS. THE SURFACE CRUST AND ZONES OF HIGHER DENSITY ARE CLEARLY VISIBLE IN F3, AND PARTLY ALSO IN F2. F1 SHOWS A RATHER HOMOGENEOUS AND DENSE PROFILE. IN F1 AND F3 WE RECOGNIZE GRAINS OF IRON HYDROXIDE (BROWN DOTS). THE SLICES HAVE BEEN CUT IN TWO PIECES (WHITE DIVIDING LINE) FOR POLISHING; THE BLUE AREAS SHOW THE COLORED RESIN CARRIER. 64
- FIGURE 5-11: SEM DETECTION OF SILICA GEL IN F3: A) FINE FILAMENTS TYPICAL FOR GEL FORMATION B) SMOOTH AMORPHOUS GEL STRUCTURES IN A PORE C) AMORPHOUS LAYERS ON GRAIN SURFACES INDICATE A THIN HYDROPHOBIC FILM OF SILICONE RESIN. 65
- FIGURE 6-1: (A) THIN SECTION OF THE HIGHLY POROUS CALCAREOUS ARENITE FROM AFLENZ (BLUE STAINED RESIN) CONSISTING OF DEBRIS FROM CALCAREOUS RED ALGAE AND FORAMINIFERS. (LENGTH OF THE PICTURE ABOUT 10MM) (B) THIN SECTION OF THE HIGHLY POROUS CALCAREOUS ARENITE FROM ST. MARGARETHEN (BLUE STAINED RESIN) CONSISTING OF DEBRIS FROM CALCAREOUS RED ALGAE, ECHINODERMS AND FORAMINIFERS. (C) THIN SECTION OF WEATHERED QUARTZ ARENITE FROM LOWER AUSTRIA (MAUERBACH) WITH A LAYER OF CRYSTALLISED GYPSUM ON THE SURFACE (TOP OF THE PICTURE); SCALE ABOUT 3X5 MM (CROSSED NICOLS). 68
- FIGURE 6-2: THE NT OF S1 WITH DIFFERENT CONSOLIDANTS. LEFT) A HOMOGENEOUS DISTRIBUTION OF OH100. IN RIGHT, THERE IS A SURFACE EFFECT. THIS NT WAS PERFORMED ONE MONTH AFTER STRENGTHENING WHEN THE CONSOLIDANTS HAD STABILIZED. THE NEUTRON ATTENUATION WAS HIGHER IN THE INITIAL NT MEASUREMENTS AND LOWER AFTERWARDS WHICH IS DUE TO THE EVAPORATION OF THE SOLVENT OVER TIME. A 400 μM ^6Li BASED SCINTILLATOR AND A CCD CAMERA WERE USED. THE EXPOSURE TIME WAS 40S PER IMAGE AND THE NUMBER OF PROJECTIONS WAS 180.. 70
- FIGURE 6-3: A) NT-BOTTOM PART OF THE STONE STRENGTHENED WITH OH100. THE NT MEASUREMENT SHOWS THAT OH100 IS HOMOGENEOUSLY DISTRIBUTED. B) NT OF THE TOP PART OF THE STONE STRENGTHENED WITH PARALOID 5%.IT IS WELL VISIBLE THAT THE DISTRIBUTION IS DIFFERENT FROM THE FIRST CASE. THE LIGHT COLOUR SHOWS LOW DENSITY OF STRENGTHENER AND THE DARK BLUE SEGMENTS REPRESENT HIGH DENSITY AREAS. THESE RESULTS ARE VERY INTERESTING FOR GEOLOGISTS AND CONSERVATORS. 71
- FIGURE 6-4: NT OF S3; A) NT BEFORE TREATMENT, THE DARK SEGMENTS REPRESENT HUMIDITY OR MICA. B) NT AFTER TREATMENT WITH PARALOID 1%. IN B) THE ARROWS INDICATE LAYERS WHERE A LOWER CONCENTRATION OF THE SOLUTION IS VISIBLE. FIGURE 4B) SHOWS NT OF THE STONE SOON AFTER STRENGTHENING. A LOW CONCENTRATION OF THE DARK SEGMENTS COULD BE A RESULT OF SEDIMENTARY LAYERING IN MORE POROUS WEATHERED REGIONS. A RATHER HOMOGENEOUS

List of Figures

DISTRIBUTION HAS BEEN OBTAINED. BY REDUCING THE CONCENTRATION, THERE IS NO NEGATIVE SURFACE EFFECT VISIBLE	72
FIGURE 6-5: A) THE LINE PROFILE TAKEN VERTICALLY ALONG THE CENTRE OF NR IMAGES OF THE TIME SERIES. B) THE DENSITY DISTRIBUTIONS OF TWO DIFFERENT STRENGTHENERS ALONG THE HEIGHT OF THE STONE. THE STONES WERE STRENGTHENED TO A HEIGHT OF APPROXIMATELY 3CM. THE HIGHER DENSITY AT THE BOTTOM OF THE STONE IS DUE TO THE LIQUID IN THE BATH.	73
FIGURE 7-1: A) A NEUTRON RADIOGRAPH OF A SMALL PUBE SOURCE USING THE SCINTILLATOR DETECTOR. THE EXPOSURE TIME WAS 360S. B) IMAGING PLATE RADIOGRAPH WITH AN EXPOSURE TIME OF 50MIN. C) NEUTRON RADIOGRAPH OF THE LARGER SOURCE OBTAINED WITH THE SCINTILLATOR HAVING AN EXPOSURE TIME OF 360S.	79
FIGURE 7-2: A) A SCINTILLATOR NR OF THE SMALLER PUBE SOURCE MADE WITH AN EXPOSURE TIME OF 360S. B) A GRAPH SHOWING THE HORIZONTAL LINE PROFILE TAKEN AS SHOWN IN A). FROM THE LINE PROFILE THE DIAMETER OF THE INNER ALLOY HAS BEEN DETERMINED. C) A LINE PROFILE TAKEN HORIZONTALLY FROM A NEUTRON IMAGING PLATE NR.	79
FIGURE 7-3: A) TO D) SHOWN NEUTRON RADIOGRAPHS MADE WITH THE IMAGING PLATE DETECTOR. THESE IMAGES HAVE BEEN MADE AT DIFFERENT DISTANCES FROM THE DETECTOR. ALSO IMAGES WERE MADE WITH AND WITHOUT SHIELDING TO GET BEST RESULTS. E) IS A SCINTILLATOR IMAGE AND HENCE IS NOT AFFECTED BY THE GAMMAS.....	81
FIGURE 7-4: THE NR IMAGE OF THE AMBE SOURCE. A) THE RECTANGULAR AREA SHOWS THE AREA OF INTEREST THAT WAS ANALYZED TO DETERMINE THE MATERIAL OF THE OUTER CONTAINER. B) THE RECTANGULAR AREA REPRESENTS THE REGION ANALYZED TO DETERMINE THE MATERIAL OF THE INNER CYLINDER. C) THE RECTANGULAR REGION WAS ANALYZED TO FIND THE DENSITY OF THE SOURCE WHICH WAS REQUIRED FOR THE INPUT FILE OF THE MCNP CALCULATION.	82
FIGURE 7-5: A) A RECONSTRUCTION WITH OCTOPUS SOFTWARE [OCTOPUS SOFTWARE]. B) A RECONSTRUCTION WITH IDL SOFTWARE WITHOUT BEAM HARDENING CORRECTION. C) A RECONSTRUCTION WITH IDL SOFTWARE WITH BEAM HARDENING CORRECTION. D) A 3-D VIEW AFTER BEAM HARDENING CORRECTION. E) A CHANGE IN THE TRANSPARENCY SHOWS THAT BEAM HARDENING HAS BEEN CORRECTED TO SOME EXTENT; THERE ARE STILL REGIONS WHICH SHOW A LOWER DENSITY.	85
FIGURE 8-1:(A) THE EXPERIMENTAL ARRANGEMENT SHOWING THE ALUMINUM BOX PLACED CLOSE TO THE SCINTILLATOR. (B) NR OF THE FIBER SAMPLES INSIDE THE ALUMINUM BOX. (C) NR OF THE FIBER SAMPLES WITHOUT THE BOX. ON THE LOWER SIDE THE DARK REGION SHOWS THE WALL OF THE HUMIDIFIER.	89
FIGURE 8-2: A) THE EXPERIMENTAL ARRANGEMENT SHOWING THE FIBER SAMPLES IN PILLOWS. B) NR SHOWING LYOCELL ON ONE SIDE AND POLYESTER ON THE OTHER SIDE. C) NR SHOWING CONDENSATION ALONG THE WIRES AFTER 80MIN. D) A HIGH RESOLUTION NR MADE WITH THE NEUTRON IMAGING DETECTOR. CLY REPRESENTS LYOCELL AND PES STANDS FOR POLYESTER.	90

List of Figures

FIGURE 8-3: TOP: EXPERIMENTAL SETUP. THE HUMIDIFIER WAS FILLED WITH WATER (TEXTILE WAS FULLY WET) AND THE LYOCELL FOIL WAS PLACED ON THE TOP OF THE WET TEXTILE. IN THIS SETUP, THE WIRES WEREN'T USED TO MAKE A DISTANCE BETWEEN THE FOIL AND TEXTILES. BOTTOM: IMAGING PLATE NR OF THE FILLING FIBERS, EXPOSURE TIME 10 MIN AT 62C. THIS IMAGE SHOWS THE CONDENSATION NEAR THE SURFACE; IT SEEMS THAT THE WATER DROPLETS ARE PLACED "ABOVE THE FIBER SAMPLE". THIS PHENOMENON HAS TO BE CLARIFIED.	92
FIGURE 8-4: NEUTRON RADIOGRAPHS WITH IMAGING PLATE DETECTOR, STARTING WITH ROOM CONDITIONS. GRAPH 1 AND GRAPH 2 SHOW THE LINE PROFILES TAKEN ALONG THE HEIGHT OF THE LYOCELL FIBER AT DIFFERENT TEMPERATURES. GRAPH 3 SHOWS THE PRELIMINARY ANALYSIS OF THE DENSITY OF WATER OR HYDROGEN RELATIVE TO TEMPERATURE.	95
FIGURE 8-5: NEUTRON RADIOGRAPHIES MADE WITH AN IMAGING PLATE WITH AN EXPOSURE TIME OF 50 MINUTES. THESE IMAGES CLEARLY SHOW THE HUMIDITY DISTRIBUTION IN THE TWO TYPES OF FIBERS.	96
FIGURE 9-1: NIP IMAGES OF A 4 MM THIN-SLICE CALCAREOUS ARENITE IN DRY AND WET CONDITION AFTER 30 MIN WETTING IN A SOAKING BATH. THE DENSITY PROFILE WAS DETERMINED ALONG THE VERTICAL AXIS IN STEPS OF 25 μM	99
FIGURE 9-2: COMPARISON OF TWO FULL DYNAMIC RANGE IMAGES OF A THIN WATER LAYER BETWEEN TWO ALUMINUM PLATES WITH 40 μM THICKNESS ON AVERAGE. LEFT: 100 μM THIN PLATE SCINTILLATOR WITH 200 X 200 μM^2 OPTICAL RESOLUTION. RIGHT: IMAGING PLATE, 25 X 25 μM^2 READOUT RESOLUTION. DRY AND WET REGIONS ARE CLEARLY RESOLVED IN BOTH DETECTORS BUT THE BETTER SPATIAL RESOLUTION OF THE IMAGING PLATE ALLOWS A MORE PRECISE DENSITY ANALYSIS (CONTRAST OF THE RAW IMAGES ENHANCED ONLY FOR PRESENTATION).	100
FIGURE 9-3: TIME SERIES SHOWING NR AFTER DIFFERENT INTERVALS OF TIME. THE RED LINES REPRESENT THE LINE PROFILE TAKE VERTICALLY.	103
FIGURE 9-4: LEFT – LINE PROFILES SHOWING THE PENETRATION OF WATER IN THE STONE AFTER DIFFERENT INTERVALS OF TIME. RIGHT: A GRAPH SHOWING THE FRONT POSITION VERSUS THE SQUARE ROOT OF TIME. THE SLOPE OF THIS CURVE IS 0.35 $\text{CM}/\text{S}^{1/2}$	104
FIGURE 9-5: LEFT: THE MASS THICKNESS OF WATER IN THE STONE CALCULATED WITHOUT CORRECTION. RIGHT: THE MASS THICKNESS OF WATER AFTER APPLYING CORRECTIONS.	105
FIGURE 9-6: LEFT: THE NR IMAGES AFTER DIFFERENT INTERVALS OF TIME SHOWING THE IMBIBITION OF WATER. RIGHT: LINE PROFILES TAKEN VERTICALLY ALONG THE HEIGHT OF THE STONE AFTER DIFFERENT TIME INTERVALS.	106
FIGURE 9-7: LEFT: A GRAPH SHOWING THE POSITION OF THE WATER FRONT RELATIVE TO THE SQUARE ROOT OF TIME. RIGHT: THE MASS THICKNESS OF WATER IN THE STONE AFTER ABOUT 9 MIN. THE SLOPE OF THE CURVE ON THE RIGHT GIVES THE PENETRATION COEFFICIENT OF WATER WHICH IN THIS CASE IS 0.2 $\text{CM}/\text{S}^{1/2}$	106
FIGURE 9-8: AN X-RAY CT OF A CALCAREOUS ARENITE STONE. BELOW, A FRONT VIEW OF A VERTICAL CUT AND A VIEW OF THE HORIZONTAL CUT OF THE STONE.	108

List of Figures

FIGURE 10-1: NEUTRON IMAGES OF 35 MM THICK FELDSPAR REVEAL DARK REGIONS OF BORON (3.3%) IN TOURMALINE, HYDROGEN IN MUSCOVITE (MICA), AND SPURIOUS RARE EARTH ELEMENTS IN GARNET. THE UNPROCESSED IMAGES DEMONSTRATE THE HIERARCHY OF DETECTOR RESOLUTION, THE BEST RESULT WITH THE NIP (RIGHT), WHICH IS ALSO FREE OF WHITE SPOTS AS SEEN IN THE SCINTILLATOR IMAGES (LEFT AND MIDDLE).	110
FIGURE 10-2: A) IMAGING OF FELDSPAR DIRECTLY IN FRONT OF THE IMAGING PLATE WITH 3 CM LEAD FOR ADDITIONAL GAMMA SHIELDING. B) SAME SAMPLE WITHOUT LEAD SHIELDING, IN BOTH CASES THE TRANSMISSION THROUGH THE FELDSPAR IS 47 % ON AVERAGE. C) DESPITE THE LONGER EXPOSURE TIME (30 MIN GD CONVERTER X-RAY FILM / 10 MIN NIP) THE IMAGE GRADATION IS MUCH SMALLER IN THE FILM DETECTOR. D) THE POOR GAMMA IMAGE EMPHASIZES THE STRENGTHS OF NEUTRONS FOR THE INVESTIGATION OF GEOLOGICAL SAMPLES.	112
FIGURE 10-3: TOMOGRAPHY OF FELDSPAR.	113
FIGURE 10-4: A) TWO ST. MARGARETHEN CALCAREOUS ARENITE SAMPLES. B) FOR MEASUREMENT, THE SAMPLES WERE PLACED ONE ON TOP OF THE OTHER. C) A NT MEASUREMENT OF THE STONES.	114
FIGURE 10-5: NEUTRON RADIOGRAPHY MEASUREMENTS OF DIFFERENT THICKNESSES OF THE BORON STEEL PLATES WERE MADE USING THE SCINTILLATOR DETECTOR. THE DISTANCE BETWEEN THE DETECTOR AND THE SAMPLE WAS ALSO VARIED.	115
FIGURE 10-6: NIP IMAGES OF THE STEEL INSPECTION. LEFT: THE INTRINSIC GRANULAR STRUCTURE OF THE NIP. MIDDLE: TRANSMISSION IMAGE OF THE BORON ALLOYED STEEL SUPERPOSED BY THE GRANULARITY OF THE NIP. RIGHT: AFTER OPEN BEAM CORRECTION, NO SIGNIFICANT INHOMOGENEITIES REMAINED. ...	116
FIGURE 12-1: A GRAPH SHOWING THE EFFECTIVE ATTENUATION COEFFICIENT OR MACROSCOPIC CROSS-SECTION OF THE DIFFERENT MATERIALS RELATIVE TO THICKNESS.	121
FIGURE 12-2: THE WINDOW USED TO CONTROL THE SHUTTER FROM THE INSTRUMENT COMPUTER.	122
FIGURE 12-3: THE CODE FOR OPENING AND CLOSING THE SHUTTER.	123
FIGURE 12-4: NEUTRON RADIOGRAPHY OF A GOLD CHAIN SHOWING THE HOLLOW DESIGN. THE THICKNESS HERE REFERS TO THE DISTANCE THE NEUTRONS HAVE TO TRAVEL THROUGH.	124
FIGURE 13-1: A) SAMPLE PHOTOGRAPH. B) NT OF THE SAMPLE WHERE THE RED SEGMENTS REPRESENT THE CONSOLIDANT. A VERTICAL CUT OF THE STONE HAS BEEN SHOWN.	125
FIGURE 13-2: A) PHOTOGRAPH OF THE SAMPLE. B) NT OF THE SAMPLE. THE STONE HAS BEEN MADE TRANSPARENT TO REVEAL THE HIGHLY ATTENUATING REGIONS.	126
FIGURE 13-3: A) PHOTOGRAPH OF THE SAMPLE. B) NT SHOWING THE CONSOLIDANT IN RED COLOR.	127
FIGURE 13-4: A) PHOTOGRAPH OF THE SAMPLE. B) A VERTICAL CUT OF THE RECONSTRUCTED SAMPLE REVEALING THE CONSOLIDANT IN RED COLOR. C) THE STONE HAS BEEN MADE TRANSPARENT TO SHOW THE STRENGTHENER.	128
FIGURE 13-5: A) PHOTOGRAPH OF THE SAMPLE. B) THE HIGHLY ATTENUATING REGION SHOWN IN RED COLOR HAS BEEN EXTRACTED FROM THE RECONSTRUCTED 3D RENDERING.	130

List of Figures

List of publications

This thesis is based on the following list of publications:

Journal articles

- M. Zawisky, F. Hameed, E. Dyrnjaja, J. Springer:
“Digitized neutron imaging with high spatial resolution at a low power research reactor. Part I: Analysis of the performance of our new detector systems”;
Nuclear Instruments and Methods in Physics Research A 587 (2008) 342–349.
- F. Hameed, B. Schillinger, A. Rohatsch, M. Zawisky, H. Rauch
“Investigations of stone consolidants by neutron imaging”
Nuclear Instruments and Methods in Physics Research A (in print)
- M. Zawisky, F. Hameed, E. Dyrnjaja, J. Springer, A. Rohatsch
“Applications and results obtained with steel and rock samples”,
Nuclear Instruments and Methods in Physics Research A (in progress)

Conference proceedings

- F. Hameed, A. Rohatsch, J. Weber, B. Zamani, M. Zawisky,
“Investigation of calcareous arenites from St. Stephan’s cathedral, Vienna”
Neutron Radiography - WCNR 8, USA, 2006, ISBN: 978-1-932078-74-9
- F. Hameed, S. Karimzadeh, M. Zawisky
“Neutron imaging of radioactive sources”
SPIE Optics + Photonics 2008, San Diego, California; USA, 10.08.2008 - 14.08.2008;
in: *“Penetrating Radiation Systems and Applications”*, (2008), ISBN: 9780819473004
DOI:10.1117/12.794776.

List of Publications

Talks and Poster Presentations

- F. Hameed, M. Bastürk, H. Rauch, B. Zamani, M. Zawisky:
"Investigation of Samples from St. Stephans Cathedral, Vienna";
Poster: Int. Workshop Neutron Imaging using Cold Neutrons – ICON 2005, PSI, Villigen (Switzerland); 13-10-2005 – 14-10-2005.
- F. Hameed, A. Rohatsch, B. Zamani, M. Zawisky:
"Investigation of building stones using Neutron Radiography and Tomography";
Poster: Workshop “Neutrons for Geoscience” TU Munich, Garching (Germany); 14-07-2006.
- F. Hameed, M. Zawisky:
"Neutron tomography Investigations of lime sandstones from the facade of St. Stephans";
Poster: 56. Jahrestagung der Österr. Physikalischen Gesellschaft (ÖPG), TU Graz, Graz; 18-09-2006 - 21-09-2006.
- M. Zawisky, F. Hameed, A. Rohatsch, J. Weber, B. Zamani:
"Investigation of calcareous arenites from St. Stephans Cathedral, Vienna";
Talk: 8th World Conf. on Neutron Radiography, NIST-Gaithersburg (USA); 16-10-2006 - 19-10-2006.
- F. Hameed, H. Rauch, A. Rohatsch, M. Zawisky
“Upgrading and applications of the neutron imaging facility at a low power research reactor”
Talk: The 57th annual convention of ÖPG (Austrian Physics Society), at The Danube University Krems, Austria on 25th September 2007
- F. Hameed, S. Karimzadeh, M. Zawisky
“Neutron imaging of radioactive sources”;
Talk: SPIE Optics + Photonics 2008, San Diego, California, USA; 10-08-2008 – 14-08-2008.
- F. Hameed, B. Schillinger, A. Rohatsch, M. Zawisky, H. Rauch
“Investigations of stone consolidants by neutron imaging”.

List of Publications

Talk: The 6th International Topical Meeting on Neutron Radiography (ITMNR-6),
Kobe, Japan, 14-18 September, 2008

- M. Zawisky, F. Hameed, E. Dyrnjaja, J. Springer
“High Resolution Neutron Imaging in Nuclear Engineering, Stone Consolidation and Geology”

Poster: The 58th annual convention of ÖPG (Austrian Physics Society), at
Montanuniversität Leoben, Austria, 25th September 2008

Scientific Reports

- M. Zawisky, F. Hameed, A. Rohatsch, J. Weber, B. Zamani:
"Messergebnisse an 4 Bohrkernen von der Fassade des Stephansdoms zum Nachweis des Steinfestigers und der Wasserdurchlässigkeit";
Report for Dombauhütte St. Stephan; 2006; 5 pages.
- F. Hameed, M. Bastuerk, M. Zawisky:
Neutron imaging of stone samples'
Report for FRM II; Technical University, Munich, Germany; 2006; 5 pages.
- F. Hameed, K. Varga, M. Zawisky, K. Schuster:
'Neutron imaging of textile fibers'.
Report for Lenzing Textile Company; Austria; 2008; 10 pages.

14 REFERENCES

- Abd, A., A. Czachor, J. J. Milczarek and J. Pogorzelski (2002). Abd, A., Czachor, A., Milczarek, J.J., Pogorzelski, J.: "Neutron radiography studies of water migration in construction porous materials" Neutron radiography (7) – Proceedings of the 7th World Conference, Rome 2002, edited by P. Chirco et al., pp. 651. Neutron radiography (7). Rome.
- Abd, A. E. G. and J. J. Milczarek (2004). "Neutron radiography study of water absorption in porous building materials: anomalous diffusion analysis." Journal of Physics D: Applied Physics **37**: 2305-2313.
- Abu-Rous, M., K. Varga, T. Bechtold and K. C. Schuster (2007). "A New Method to Visualize and Characterize the Pore Structure of TENCEL1 (Lyocell) and other Man-Made Cellulosic Fibers Using a Fluorescent Dye Molecular Probe." Journal of Applied Polymer Science **106**: 2083-2091.
- Arif, M., D. Jacobson and R. Satija (2003). Neutron Imaging Study Of the Water Transport Mechanism in a Working Fuel Cell.
- Bastürk, M. (2003). Material Inspections with Low Energy Neutrons and 3D Image Reconstruction. Atomic Institute. Vienna, Vienna University of Technology. **PhD**: 152.
- Bastuerk, M., J. Arzmann, W. Jerlich, N. Kardjilov, E. Lehmann and M. Zawisky (2005). "Analysis of neutron attenuation in boron-alloyed stainless steel with neutron radiography and JEN-3 gauge." Journal of Nuclear Materials **341**: 189-200.
- Bayülken, A., H. Böck, H. Schachner and T. Buchberger (1990). "Quantitative analysis of boron by neutron radiography." Kerntechnik - Independent Journal for Nuclear Engineering, Energy Systems and Radiation **55**(1): 53 - 55.
- Bruckner, G., A. Czermak, H. Rauch and P. Weilhammer (1999). "Position sensitive detection of thermal neutrons with solid state detectors (Gd Si planar detectors)." Nuclear Instruments and Methods in Physics Research A **424**: 183-189.
- Buchberger, T., H. Rauch and E. Seidl (1989). "Tritium and helium 3 in metals investigated by neutron radiography." Kerntechnik - Independent Journal for Nuclear Engineering, Energy Systems and Radiation **53**(3): 215-217.
- Chountas, K. and H. Rauch (1968). "Neutronenradiographie von Metallklebungen, Legierungen, aktiven Reaktorbrandelementen, Diffusion von H in Zr, und Diffusion H₂O-D₂O." Atomenergie **13**: 444.

References

- Cnudde, V., M. Dierick, J. Vlassenbroeck, B. Masschaele, E. Lehmann, P. Jacobs and L. V. Hoorebeke (2008). "High-speed neutron radiography for monitoring the water absorption by capillarity in porous materials." Nuclear Instruments and Methods in Physics research B **266**: 155-163.
- Cnudde, V. C., M. Dierick, J. Vlassenbroeck, B. Masschaele, E. Lehmann, P. Jacobs and L. V. Hoorebeke (2007). "Determination of the impregnation depth of siloxanes and ethylsilicates in porous material by neutron radiography." Journal of Cultural Heritage **8**: 331-338.
- Curtiss, L. F. (1958). Introduction to Neutron Physics. Princeton, New Jersey, Toronto, New York, London, D. Van Nostrand Company, Inc.
- DATASHEET "TECHNICAL DATA SHEET Paraloid® B72 Fixative (SY7F)."
- de Beer, F. C., M. F. Middleton and J. Hilson (2004). "Neutron radiography of porous rocks and iron ore." Applied Radiation and Isotopes **61**: 487-495.
- Domanus, J. C. (1992). Practical Neutron Radiography. Dordrecht, Boston, London, Kluwer Academic Publishers.
- Draganits, E., B. Grasemann and C. Hager (2005). "Conjugate, cataclastic deformation bands in the Lower Devonian Muth Formation (Tethyan Zone, NW India): evidence for pre-Himalayan deformation structures." Geological Magazine **142 (6)**: 765-781.
- Dubus, F., U. Bonse, T. Biermann, M. Baron, F. Beckmann and M. Zawisky (2002). Tomography using monochromatic thermal neutrons with attenuation and phase contrast. Proc. SPIE.
- Dubus, F., U. Bonse, M. Zawisky, M. Baron and R. Loidl (2005). "First Phase-Contrast Tomography With Thermal Neutrons." IEEE TRANSACTIONS ON NUCLEAR SCIENCE **52**.
- Eijk, C. W. E. V. (2001). "Inorganic-scintillator development." Nuclear Instruments and Methods in Physics Research A **460**: 1-14.
- Feigl, B. and H. Rauch (1968). "Der Gd-neutronenzähler." Nuclear Instruments and Methods **61**: 349.
- Felber, J., C. Rausch and K. Raum (GBR) "ND&M neutron handmonitor." **Volume**, DOI:

References

- Fleischer, G., J. Nimmrichter and A. Rohatsch (2005). "The relevance of scientific investigation for the preservation of monuments and historic buildings made of stone." Geophysical Research 7(04479, 2005 SRef-ID: 1607- 7962/gra/EGU05-A-04479).
- Fujifilm "Life Science." **Volume**, DOI:
- Gibbons, M. R., W. J. Richards and K. Kevin Shields (1999). "Optimization of neutron tomography for rapid hydrogen concentration inspection of metal castings." Nuclear Instruments and Methods in Physics research A.
- Gruenauer, F. (2005). "ANTARES." from <http://einrichtungen.physik.tu-muenchen.de/antares/>.
- Haga, Y. K., S. Kumazuwa and N. Nimura (1999). Journal of Applied Crystallography **32**: 878.
- Hajek, M. (2002). Applied neutron spectrometry: Applications atop high-altitude mountains and onboard aircraft. Atomic Institute. Vienna, Vienna University of Technology. **PhD**.
- Hajek, M. and W. Schöner (2001). "M. Hajek, W. Schöner, Spectral distribution of neutron fluence at the thermal column of the TRIGA Mark II research reactor, AIAU 21313, April 2001." AIAU **21313**.
- Hameed, F., S. Karimzadeh and M. Zawisky (2008). Neutron imaging of radioactive sources. SPIE Optics + Photonics, USA, ISBN: 9780819473004
- Hameed, F., A. Rohatsch, J. Weber, B. Zamani and M. Zawisky (2006). Investigation of calcareous arenites from St. Stephan's cathedral, Vienna. Neutron Radiography - WCNR8, NIST, USA, ISBN: 978-1-932078-74-9.
- Hameed, F., B. Schillinger, A. Rohatsch, M. Zawisky and A. Rauch (2008). "Investigations of stone consolidants by neutron imaging." Nuclear Instruments and Methods in Physics Research A (in print).
- Hanzic, L., Nemeč, T., Ilic, R. (2002). Determination of the capillary coefficients of distilled water and oil in concrete by Neutron radiography. Neutron radiography (7), Rome.
- Harms, A. A. and D. R. Wyman (1986). Mathematics and Physics of Neutron Radiography. Dordrecht/Boston/Lancaster/Tokyo, D. Reidel Publishing Company.

References

- Harms, A. A. and A. Zeilinger (1977). "A New Formulation of Total Unsharpness in Radiography." Phys. Med. Biol.
- Hassanein, R., H. O. Meyer, A. Carminati, M. Estermann, E. Lehmann and P. Vontobel (2006). "Investigation of water imbibition in porous stone by thermal neutron radiography." Journal of Physics D: Applied Physics **39**: 4284-4291.
- Hassanein, R. K. (2006). Correction methods for the quantitative evaluation of thermal neutron tomography. Zurich, Swiss Federal Institute of Technology. **PhD**.
- <http://www.stephansdom.at/data/restaurierung/index.php> from
<http://www.stephansdom.at/data/restaurierung/index.php>.
- Image-Pro Plus 6.0 software, M. C., USA.
- Kak, A. C. and M. Slaney (1988). Computerized tomographic imaging, IEEE Press.
- Kardjilov, N., F. de Beer, R. Hassanein, E. Lehmann and P. Vontobel (2005). "Scattering corrections in neutron radiography using point scattered functions." Nuclear Instruments and Methods A **542**: 336-341.
- Kobayashi, H. and M. Satoh (1999). "Study for a novel tomography technique using an imaging plate " Nuclear Instruments and Methods A **424**: 1.
- Koerner, S. (2000). Digital Image Processing in Neutron Radiography. Atomic Institute. Vienna, Vienna University of Technology. **PhD**.
- Koerner, S., B. Schillinger, P. Vontobel and H. Rauch (2001). "A neutron tomography facility at a low power research reactor." Nuclear Instruments and Methods in Physics Research A **471**: 69-74.
- Lamarsh, J. R. (1965). Introduction to Nuclear Reactor Theory. New York, Addison-Wesley Publishing Company, Inc. Reading Massachusetts, U.S.A.
- Lehmann, E., S. Hartmann and P. Wyer (2005). "Neutron radiography as visualization and quantification method for conservation measures of wood firmness enhancement." Nuclear Instruments and Methods **542**(1-3): 87-94.
- Lehmann, E., P. Vontobel and N. Kardjilov (2004). "Hydrogen distribution measurements by neutrons." Applied radiation and isotopes **61**: 503-509.

References

Lehmann, E. H., P. Vontobel, G. Frei and C. Broennimann (2004). "Neutron imaging—detector options and practical results." Nuclear Instruments and Methods in Physics Research A **531**: 228-237.

Lehmann, E. H., P. Vontobel and A. Hermann (2003). "Non-destructive analysis of nuclear fuel by means of thermal and cold neutrons." Nuclear Instruments and Methods in Physics Research A **515**: 745-759.

Masalovich, S., A. Ioffe, E. Küssel, M. Schlapp, H. V. Seggern and T. Brückel (2002). "Development of neutron image plate for low-flux measurements." Applied Physics A materials science and processing **74**.

Mishra, K. K. (2005). North Carolina State University.

Müller, H. W., A. Rohatsch, B. Schwaighofer, F. Ottner and A. Thinschmidt (1993). Österreichische Zeitschrift für Kunst und Denkmalpflege 3/4: 106.

Nemec, T., J. Rant, V. Apih and B. Glumac (1999). "Study of building materials impregnation processes by quasi-real-time neutron radiography." Nuclear Instruments and Methods in Physics Research A **424**: 242-247.

Octopus software, U. G., Belgium Octopus software, University Ghent, Belgium.

Patent WACKER OH 100, Wacker Chemie AG, Germany; REMMERS Funcosil 100, Remmers Baustofftechnik, Germany.

Pel, L., A. A. J. Ketelaars, O. C. G. Adan and A. A. Van Well (1993). "Determination of moisture diffusivity in porous media using scanning neutron radiography." Int. J. Heat Mass Transfer **36**(5): 1261-1267.

Pleinert, H. (1998). "Determination of Moisture Distributions in Porous Building Materials - Neutron Signal Transfer Analysis." Building Materials Reports **10**.

Pleinert, H., E. Lehmann and S. Koerner (1997). "Design of a new CCD-camera neutron radiography detector." Nuclear Instruments and Methods in Physics Research A **399**: 382-390.

Pochman, W. A., A. Zeilinger and H. Böck (1977). "Detection of cracks in TRIGA fuel rods by neutron radiography." Atomkernenergie (ATKE) Bd. 29, Lfg 3.

References

- Price, C. A. (1996). Stone Conservation - An Overview of Current Research. USA.
- Rauch, H. and A. Zeilinger (1977). "Hydrogen transport studies using neutron radiography." Atomic Energy Review.
- Rodrigues, J. D. (2001). "Consolidation of decayed stones. A delicate problem with few practical solutions." Historical Constructions.
- Schillinger, B., E. Calzada, F. Grünauer and E. Steichele (2004). "The design of the neutron radiography and tomography facility at the new research reactor FRM-II at Technical University Munich." Applied Radiation and Isotopes **61**(4): 653-657.
- Schillinger, B. and E. Lehmann (2006). "Scientific Reviews: Detectors for Neutron Imaging." Neutron News **17**: 19-21.
- Schuster, K. C., C. Rohre, D. Eichinger, J. Schmidthauer, P. Aldred and H. Firgo (2004). Environmentally friendly lyocell fibers. Book Chapter 9. W. F. T. W. N., Kowler Academic Publishers.
- Sears, V. F. (1975). Advances in Physics **24**: 1.
- Sears, V. F. (1983). Nuclear Instruments and Methods **213**: 561.
- Shipton, Z. K. and P. A. Cowie (2003). "A conceptual model for the origin of fault damage zone structures in high-porosity sandstone." Journal of Structural Geology **25**: 333-344.
- Solyman, M., E. Lehmann, P. Vontobel and A. Nordlund (2003). "Relating variations in water saturation of a sandstone sample to pore geometry by neutron tomography and image analysis of thin sections." Bull Eng Geol Env.
- Thoms, M. (1999). "Neutron detection with imaging plates Part II. Detector characteristics." Nuclear Instruments and Methods in Physics Research A **424**: 34-39.
- Tritec, R. C. AG.
- WACKER OH 100, W. C. A., Germany; REMMERS Funcosil 100, Remmers Baustofftechnik, Germany.

References

Weder, M., P. A. Bruehwiler, U. Herzig, R. Huber, G. Frei and E. Lehmann (2004). "Neutron Radiography Measurements of Moisture Distribution in Multilayer Clothing Systems." Textile Research Journal **174**(8): 695-700.

Winkler, B., K. Knorr, A. Kahle, P. Vontobel, E. Lehmann, B. Hennion and G. Bayon (2002). "Neutron imaging and neutron tomography as non-destructive tools to study bulk-rock samples." Eur. J. Mineral **14**: 349.

Zawisky, M. Lecture - Neutron optics and tomography.

Zawisky, M., M. Bastürk, R. Derntl, F. Dubus, E. Lehmann and P. Vontobel (2004). "Non-destructive 10B analysis in neutron transmission experiments." Applied Radiation and Isotopes **61**: 517-523.

Zawisky, M., M. Bastürk, J. Rehacek and Z. Hradil (2004). "Neutron tomographic investigations of boron-alloyed steels." Journal of Nuclear Materials **327**: 188-193.

Zawisky, M., F. Hameed, E. Dyrnjaja and J. Springer (2008). "Digitized neutron imaging with high spatial resolution at a low power research reactor: 1. Analysis of detector performance." Nuclear Instruments and Methods A **587**(2-3): 342-349.

Zawisky, M., F. Hameed, E. Dyrnjaja, J. Springer and A. Rohatsch "Applications and results obtained with steel and rock samples." Nuclear Instruments and Methods in Physics Research A (in progress).

Zeilinger, A. and W. A. Pochman (1976). "New method for the measurement of hydrogen diffusion in metals." Journal of Applied Physics.